Chem Soc Rev

Near Infrared light responsive nanomaterials in cancer therapeutics

Journal:	*Chemical Society Reviews*
Manuscript ID:	CS-REV-01-2014-000011.R1
Article Type:	Review Article
Date Submitted by the Author:	07-Mar-2014
Complete List of Authors:	Shanmugam, Vijayakumar; National Cheng Kung University, Department of Chemistry Selvakumar, Subramanian; National Cheng Kung University, Department of Chemistry Yeh, Chen-Sheng; National Cheng Kung University, Department of Chemistry

SCHOLARONE™
Manuscripts

Near-infrared light-responsive nanomaterials in cancer therapeutics

Vijayakumar Shanmugam[‡] S. Selvakumar[‡] and Chen-Sheng Yeh*

Noninvasive techniques, such as breath tests (urea breath test), blood pressure measurements using a sphygmomanometer, and electrocardiography, were employed by a physician to perform classical diagnosis. The use of state-of-the-art noninvasive therapies at the organ level in modern medicine has gradually become possible. However, cancer treatment demands for spatially and temporally controlled noninvasive therapy at the cell level because nonspecific toxicity often causes complicated side effects. To increase survival in cancer patients further, combination therapy and combination drugs are explored which demand for high specificity to avoid combined drug side effects. We believe that high specificity could be obtained by implementing near-infrared (NIR) light-assisted nanoparticles in photothermal therapy, chemotherapy-, and photodynamic therapy. To refine this therapy and subsequently achieve high efficiency, novel nanomaterials have been designed and modified either to enhance the uptake and drug delivery to the cancer site, or control treatment to administer therapy efficiently. These modifications and developments have been demonstrated to achieve special and temporal control when conducting an *in vivo* xenograft, because the NIR light effectively penetrated the biological tissue. The nanoplatforms discussed in this review are grouped under the following subheadings: Au nanorods (NRs), Au nanoshells, other Au-related nanomaterials, graphene oxide, upconversion nanoparticles, and other related materials (including materials such as CuS, Fe_3O_4-related systems, and carbon nanotubes (CNTs)).

A. Introduction

Cancer is a serious disease that challenges the survival of people in all age groups, especially those living in developed countries. Cancer is the uncontrolled growth of cells that can occur in any type of tissue, and at the later stage begins to migrate and relocate to noncancerous tissue. This spread of cancer is called metastasis. Therefore, treating cancer at the early stage is optimal. However, the only treatment option is to kill the cancer cells, which could result in detrimental consequences. If the cancer cells are not killed, then the cancer spreads, but if the cancer cells are killed, healthy cells are likely to be damaged as well. Consequently, selectively killing the cancer cells without damaging healthy noncancerous cells is challenging, but can be accomplished by using nanotechnology. In classical terms, nanotechnology can be used to transport drugs to a specific site using specific markers. However, these markers are not unique to the cancer cells; they are overexpressed, which also happens in pluripotent or young healthy cells as well. Hence this marker-assisted deliver has a chance to get misdirected. Therefore, using external stimulation to control the release of drugs systemically is the goal in developing next-generation treatment. This can be accomplished by using optical nanoparticles exhibiting near-infrared (NIR) absorbance. As water and blood cells absorb NIR hardly, NIR can penetrate the tissue to reach the deeply placed optically sensitive nanoparticles. The penetrating NIR radiation can be transduced into local heat by the nanoparticles; consequently, this heat can be envisaged for the photothermal therapy (PTT). Otherwise, potentially harsh traditional hyperthermia methods such as using a hot-water bath, heated blood perfusion, or an electromagnetic approach were used.[1] In addition to the direct effect of these particles on heat delivery to the site, when illuminated using an NIR laser for PTT, these heat-transducing nanoparticles can also demonstrate controlled drug release through the transduction of heat to the thermoresponsive drug reservoirs, such as polymers and supramolecules, coated on heat-transducing nanoparticles. Furthermore, these nanoparticles can transport the photodynamic agent, so that the NIR can be additively used for photodynamic therapy (PDT). PDT involves using the reactive oxygen species (ROS) to kill the cancer cells, which is produced from the photodynamic agent.[2,3] The light is nontoxic when not combined with the photodynamic agent; similarly, the photodynamic agent is nontoxic when not combined with the excitation energy of light. Thus, phototoxicity can be performed and controlled externally using these nanoplatforms to avoid collateral damage, which is a serious side effect of cancer chemotherapy. For example, the indocyanine green (ICG) photodynamic agent requires low excitation energy and, thus, can be excited using an NIR laser. Consequently, ICG can be loaded into a transducer, such as nanorod (NR), to implement the NIR laser in performing PTT using the NR and PDT from ICG. This combination therapy enhances the therapeutic effects of the treatment. However, not all photodynamic agents exhibit a similar low excitation-energy requirement because most efficient ROS producers require the presence of high-energy photons in the visible wavelength, which cannot penetrate the tissue effectively. In this context, recently developed upconversion nanoparticles (UCNPs) are a promising candidate for overcoming this limitation by providing high energy from the incident NIR energy through upconversion. Thus, these UCNPs have given clinical hope for PDT.

However, this NIR-assisted therapy may still be challenged in the clinical setting by the technique of stimulating the tumors located deep in the tissues. Numerous studies have emphasized the strategy of reaching deep-seated tumors using optical fibers. Recently, Batia *et al*. implanted an NIR source to irradiate deep-seated tumors for performing PTT using NRs as photothermal antenna.[4] Therefore, the use of this class of nanomaterials will change cancer therapy radically in the near future. In this review, we identified the potential NIR-absorbing

Department of Chemistry and Department of Materials Science and Engineering, National Cheng Kung University
Tainan 701, Taiwan
E-mail: csyeh@mail.ncku.edu.tw
‡ These authors contributed equally

nanomaterials used for PTT, drug delivery, and PDT, from the literatures and discussed the ability of these nanomaterials to treat various cancers using modified nanoplatforms according to tumor targeting specificity to improve the efficiency of the treatment. The nanoplatforms discussed are grouped under the following subheadings: Au NRs, Au nanoshells, other Au-related nanomaterials, graphene oxide, UCNPs, and other related materials (including materials such as CuS, Fe_3O_4-related systems, and carbon nanotubes (CNT)). The aim of this review is to provide a summary of nanoplatforms, their modifications, and their efficiency in producing a photo-induced therapeutic effect.

B. Au nanorod

B.1. Properties and synthesis

Au NR is an attractive nanostructure that demonstrates unique optical behaviour. This optical behaviour is caused by the anisotropic structure that comprises the plasmon cloud located on two axes, one on the transverse axis and the other on the longitudinal axis. The transverse band oscillates in resonance with high-energy visible electromagnetic waves at 500 nm and the longitudinal band oscillates in resonance toward the low-energy NIR range. This longitudinal range can be tuned by changing the aspect ratio. Generally, Au NRs synthesized with an aspect ratio of 4 show a longitudinal absorbance at approximately 800 nm. Hence, this material combined with 800-nm laser irradiation absorbs the photons and converts the energy to heat. The photothermal properties of the material at the NIR range are unique because of the biological transparency. Although isotropic gold nanospheres have been claimed to exhibit photothermal properties when irradiated with a laser with a visible wavelength, the corresponding wavelength cannot penetrate the tissues deeply or efficiently.[5]

Au NRs synthesis was successfully demonstrated in the 1990s using a hard template, porous alumina, in which gold was electrodeposited to form NRs. The Au NRs in the porous channels were extracted by dissolving the alumina with NaOH.[6] Murphy *et al*[7] and El-Sayed *et al.*[8] used seed mediated Au NRs growth with cetyl trimethyl ammonium bromide (CTAB). Subsequently, Jana successfully demonstrated large-scale synthesis in solution.[9] Although CTAB facilitates Au NR synthesis and enables NRs distribution with the flexibility to tune the aspect ratio by modifying the Ag ion concentration,[8] the presence of CTAB, a potential cytotoxic agent, presents obstacles to its application in the field of biomedicine. However, no favourable alternative for synthesizing high-quality NRs without using CTAB exists. Therefore, strategies for overcoming the toxicity of CTAB, such as layer-by-layer assembly and ligand exchange, are presented.

B.2. Photothermal therapy

The photothermal property of Au NRs enables the extensive use of these NRs in nanoparticle-assisted PTT. In this context, the following subjects are discussed: (1) to overcome the toxicity of CTAB, Au NRs have been modified to achieve the

biocompatibility and conjugation of the targeting proteins or peptides for enhancing uptake and increasing PTT efficiency; (2) the mechanism of Au NRs-assisted PTT involving membrane permeability, the influx of the cation, and actin damage; and (3) Au NRs in conjugation with other functional nanoparticles were designed to produce multifunctionalities.

Huang *et al.*[10] studied the applications of Au NRs in imaging and PTT. In this trial, Au NRs were synthesized using seed-mediated method with the assistance of CTAB. Au NRs coated with a CTAB bilayer were masked using poly(styrenesulfonate) (PSS) polymer through electrostatic attraction. To conduct *in vitro* imaging and therapy, both human oral squamous cell carcinomas (HOC 313 clone 8 and HSC 3) and the human keratinocyte nonmalignant oral epithelial cell line (HaCat) were used. Because the malignant cells overexpress the epidermal growth factor receptor (EGFR), the PSS-coated Au NRs were coated with targeting antiEGFR antibodies to form antiEGFR-Au NRs. In the light-scattering image, the antiEGFR-Au NRs showed greater uptake on the malignant cell line than on the nonmalignant cells. This is due to the difference in EGFR targeting to the malignant cells and passive uptake in the nonmalignant cells. This was also confirmed by the increase in the extinction intensity measured by comparing the malignant cells with the nonmalignant cells. In PTT, the malignant cells incubated with the antiEGFR-Au NRs induced cell death at an 800-nm continuous wave (CW) Ti: sapphire laser with a power density of 10 W/cm^2 whereas the nonmalignant HaCat cells incubated with the antiEGFR-Au NRs required the use of an NIR laser with a power density of 20 W/cm^2 to cause cell death. This proved the efficiency of using antiEGFR-Au NRs to destroy cancer cells in PTT. The imaging and PTT effects of using polymer-based nanocarriers containing Au NRs were also demonstrated in comparison with the as-prepared Au NRs by Choi *et al.*[11] In this study, Au NRs were prepared using the seed-mediated method with the help of CTAB. Chitosan-conjugated pluronic F-68-based, denoted as chi-PF68, nanocarriers were prepared using photopolymerization. For comparison, bare pluronic F-68 nanocarriers (PF68) were also used. To load the Au NRs into the polymer nanocarriers, an Au NR solution was mixed with the powders of PF68 and chi-PF68, and the incubated for 12 h at 4° C to form Au NRs@PF68s and Au NRs@chi-PF68s, respectively. The synthesis scheme is shown in Fig 1. SCC7 squamous carcinoma cells were used for the *in vitro* examination. The uptakes of Au NRs@chi-PF68 and Au NRs@PF68 in comparison with that of Au NRs by SCC7 cells were observed through scattering images. The scattering images showed the uptake in the order of Au NRs@chi-PF68s > Au NRs@PF68s > Au NRs. For conducting the *in vitro* PTT, the SCC7 cells were incubated with Au NRs@chi-PF68s, Au NRs@PF68s, or Au NRs and irradiated using a 780-nm CW Ti: sapphire laser with two laser power densities (41.5 W/cm^2 or 26.4 W/cm^2). In the fluorescence imaging of the cells stained with live and dead cells under PTT, the SCC7 cells incubated with Au NRs@chi-PF68s induced cells death at a laser power density of 26.4 W/cm^2, whereas SCC7 cells incubated with Au NRs@PF68s caused cell death at 41.5 W/cm^2, and the cells treated with Au NRs were not effective to induce cell death in the PTT. In the *in vivo* studies, after 24 h of Au NRs@chi-PF68 tail vein injection, the tumors were

illuminated using a 4 W/cm² 808-nm laser for 4 min, which resulted in no increase in tumor size for 1 weak and then a slight increase in tumor size was observed afterward. This regrowth was controlled with another shot of laser. However, Au NRs@PF68s and Au NRs were not effective in the complete control of tumor growth.
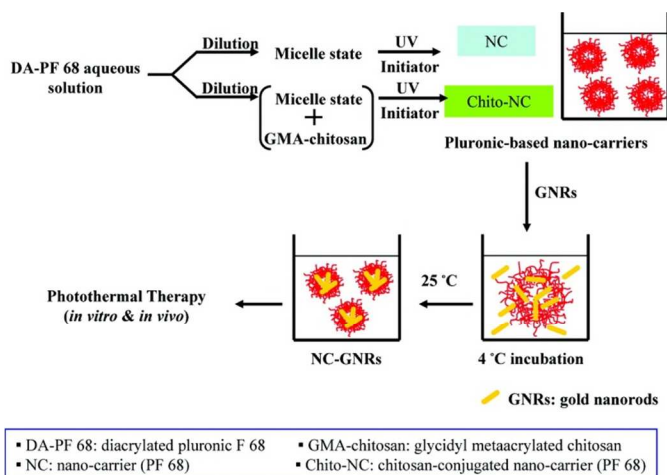

Fig. 1. The formation of Au NRs@PF68 and Au NRs@chi-PF68 occurred in the following sequence: Pluronic F-68-based nanocarriers with and without chitosan were prepared using photopolymerization → Au NRs encapsulated into nanocarriers → Au NRs@PF68 and Au NRs@chi-PF68 used in PTT (Reprinted with permission from ref. 11. Copyright *ACS Nano*, 2011).

An additional attempt was made to combine imaging with Au NR-assisted PTT using a self-immolative approach.[12] Matrix metallo protease (MMPase) overexpresses in most tumors. This protease degrades the peptide sequence of Gly-Pro-Leu-Gly-Val-Arg-Gly-Cys (MMPsubstrate).[13] To be carried by Au NRs in biomedical studies, this peptide sequence was conjugated with NIR fluorescence dye Cy5.5 to form P-Cy5 (P: peptide sequence). Au NRs were prepared using a CTAB-assisted process and the P-Cy5 was conjugated with the Au NRs by replacing CTAB to form P-Cy5-Au NRs. The normal fluorescence of Cy5.5 was quenched in P-Cy5-Au NRs, but in the tumor environment, the MMPase acted on the MMPsubstrate to release the Cy5.5 and subsequently exhibited NIR fluorescence, as shown in Fig. 2. In the *in vitro* experiment, various populations of HeLa human cervical cancer cells were grown. The mediums used to enable HeLa cell growth were separated and mixed with P-Cy5-Au NRs to measure IR fluorescence, where the population-dependent fluorescence increase was observed. In the *in vivo* imaging performance, SCC-7 tumor-bearing mice were intratumorally injected with P-Cy5-Au NRs without an MMPase inhibitor and with P-Cy5-Au NRs with an MMPase inhibitor. Bright NIR fluorescence was observed in the tumor that received the P-Cy5-Au NRs without the MMPase inhibitor, whereas fluorescence was not observed in the tumor injected with the matrix metallo protease inhibitor. To observe the *in vivo* photothermal effect, the tumors were intratumorally injected with P-Cy5-Au NRs and irradiated using the NIR laser, which resulted in the temperature of the tumor increasing to 45° C in 4 min. Moreover, on the surface

modification of Au NRs, the zwitterionic phosphorylcholine-coated Au NRs were synthesized to enhance the uptake and PTT.[14] The Au NRs were synthesized again by using CTAB. The CTAB layer on the Au NRs was replaced with 11-mercaptoundecyl phosphorylcholine using gold thiol conjugation to form Au NR@PC (PC: phosphorylcholine). To compare this zwitterionic Au NR@PC, a control was prepared by the PEGylation on the Au NRs with 11-mercaptoundecyl polyethylene glycol to form Au NR@PEG. To perform the *in vitro* uptake analysis, CNE-1 nasopharyngeal cancer cells were incubated with Au NR@PCs or Au NR@PEGs for 12 h and analyzed using inductively coupled plasma atomic emission spectroscopy. The quantitative analysis results indicated that the uptake of Au NR@PCs was 3 times greater than the uptake of the Au NR@PEGs. In addition, the Au NR@PCs were incubated with rhinal epithelial normal cells, and demonstrated only a trace amount of uptake. This observation suggests that Au NR@PCs selectively targeted the cancer cells. Furthermore, the selectivity of Au NR@PCs to CNE-1 cancer cells was confirmed using transmission electron microscopy analysis. The microtome section of the CNE-1 cancer cells treated with Au NR@PCs showed that the NRs were located in the cytoplasm, whereas no such NR structures were observed in the CNE-1 cancer cells treated with Au NR@PEGs or in the rhinal epithelial normal cells treated with Au NR@PCs. To perform i*n vitro* PTT, Au NR@PCs-treated CNE-1 cancer cells were irradiated using the NIR laser with a power density of 300 mW and were inspected using fluorescence imaging by staining the live cells with green fluorescence. The image showed the live cells exhibiting green fluorescence surrounding the black zone of dead cells due to the illumination of the NIR laser, whereas the rhinal epithelial normal cells treated with Au NR@PCs and irradiated with the NIR laser did not demonstrate cell destruction. This confirmed the selective PTT effect of Au NR@PCs on CNE-1 cancer cells.
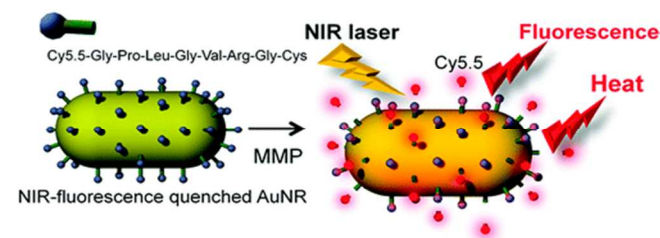

Fig. 2. P-Cy5 (P: peptide sequence; Cy 5: cyanine dye) was conjugated with Au NRs to form P-Cy5-Au NRs. The normal fluorescence of Cy5.5 was quenched in P-Cy5-Au NRs, but in a tumor environment, MMPase acted on MMP substrate to release Cy5.5, which exhibited NIR fluorescence during PTT (Reprinted with permission from ref. 12. Copyright *Bioconjugate Chem.,* 2010)

The mechanism of the photothermal effect with Au NRs was investigated to analyze the destruction of the cancer cells.[15] The CTAB layer on the Au NRs was replaced with dithiocarbamate, on which folic acid was conjugated through amide bonding to form folic acid-Au NRs (FANRs). Malignant KB oral carcinoma cells overexpress folate receptors; therefore, folic acid is used for targeting these cancer cells. For the *in vitro* examination, folic acid positive KB cells and negative NIH 3T3 mouse fibroblast cells were used for comparison in target specificity. The FANRs incubated with

the KB cells localized in the membranes in 6 h, and subsequently moved into the perinuclear region in 17 h, whereas no FANR binding was observed in the NIH 3T3 cells incubated with the FANRs. Cells with membrane-bound FANRs (at the early stage of cell incubation with FANRs) were exposed to a CW 765-nm NIR Ti: sapphire laser with a power density of 6 mW and exhibited PTT damage, whereas the cells that internalized the FANRs in the perinuclear region (at a later stage of cell incubation with FANRs) exhibited PTT damage when exposed to a CW NIR laser only with higher power density of 60 mW. Similarly for PTT conducted using a femtosecond (fs) pulse NIR Ti: sapphire laser, the cells with membrane-bound FANRs required a laser power of 0.75 mW, whereas the cells with internalized FANRs required a laser power of 4.5 mW. They observed that blebbing of the cell membranes occurred when PTT was conducted. In addition, the blebbing did not occur near the location where the FANRs were bound. Therefore, they speculated that this may have been caused by the damage in the actin that formed a dense 3-D network in the cell membrane. To test this hypothesis, KB cells with green fluorescent protein actin expression (GFPactin) were used. The GFPactin KB cells treated with FANRs and exposed to the CW NIR Ti: sapphire laser exhibited a 50% reduction in actin green fluorescence intensity with the appearance of blebbing, whereas the GFPactin KB cells exposed to the NIR laser without the FANRs demonstrated no blebbing and no significant reduction in actin fluorescence damage. In another control experiment, for the GFPactin KBs cell treated with cytochalasin D, an inhibitor of actin polymerization, the actin fluorescence did not distribute evenly when blebbing occurred. Therefore, the authors concluded that the FANR-mediated blebbing of the membrane was caused by actin degradation. Moreover, they hypothesized that the actin degradation may have been caused by the calcium ion influx in the intracellular region. To verify this, KB cells treated with FANRs were retained in calcium ion-rich or calcium ion-deficient PBS, and exposed to an fs pulse NIR laser. Ethidium bromide (EB) was used to stain the nucleus when cell permeability occurred. Both the cells in the calcium-rich and -deficient medium exhibited EB staining, but blebbing was observed only in the calcium-rich medium and not in the calcium-deficient medium. Therefore, the mechanism was revealed to be that FANRs-assisted PTT caused cavitation resulting in the influx of the calcium ion, which led to the degradation of the actin accompanied by blebbing.

In continuation of the above PTT using single component Au NRs, the following illustration using dual components of Au NRs with Fe_3O_4 for determining the multifunctional capability in magnetic resonance imaging (MRI), PTT, and optical imaging are discussed (Fig. 3).[16] The Au NRs were synthesized using the CTAB-assisted method. The CTAB layer on the Au NRs was replaced with cystamine in the first step, and stabilized using the thiolated polyethylene glycol (SH-PEG) in the second step. The iron oxide nanoparticles with carboxyl groups were synthesized to attach them to the Au NRs. In the third step, the carboxyl groups on the iron oxide surface were conjugated with the amines in the cystamine tethered to the Au NRs using amide binding (Au NR@Fe_3O_4). The remaining carboxyl groups on the iron oxide nanoparticles of Au NR@Fe_3O_4 were conjugated with the antibody herceptin to form antiHER-Au NR@Fe_3O_4 for targeting herceptin-positive SK-BR 3 human breast cancer cells. Herceptin-negative MCF7 human breast cancer cells were used as the control group. AntiHER-Au NR@Fe_3O_4 acted as the contrast agent for MRI in addition to fluorescence imaging and PTT functions. MRI was conducted by taking T2 weighted images of the SK-BR 3 cells and MCF 7 cells incubated with antiHER-Au NR@Fe_3O_4. The SK-BR 3 were darker than the MCF 7 cells in the contrast. The photon illumination confocal image of the SK-BR 3 cells incubated with antiHER-Au NR@Fe_3O_4 showed bright fluorescence, whereas fluorescence was absent in the MCF cells treated with antiHER-Au NR@Fe_3O_4, and faint fluorescence was observed in the SK-BR 3 cells treated with Au NR@Fe_3O_4 (no antibodies). The aqueous dispersion of antiHER-Au NR@Fe_3O_4 at 0.2 and 1.2 nM concentrations produced a 20° C and 25° C increase in temperature caused by the irradiation using a 785-nm CW diode laser with a power density of 4.53 W/cm^2, respectively. For *in vitro* PTT, SK-BR 3 and MCF 7 cells treated with antiHER-Au NR@Fe_3O_4 were exposed to NIR laser irradiation with a power density of 4.53 W/cm^2, and the live and dead cells were immediately stained with calcein AM and propidium iodide (PI), respectively. Consequently, the SK-BR 3 cells died, whereas the MCF 7 cells remained alive, thereby demonstrating the target specific PTT effect of antiHER-Au NR@Fe_3O_4. Further, multifunctional Au NR@Fe_3O_4 demonstrated PTT along with MR and photoacoustic (PA) images.[17] The surface of the Au NRs was coated with poly(N-isopropylacrylamide-comethacrylic) to form P-Au NRs (P: polymer coating). In addition, the iron oxide nanoparticles were activated in base solution and coated with (3-aminopropyl)triethoxysilane (APTES). Subsequently, the P-Au NRs were conjugated with the iron oxides through amide binding to yield MP-P-Au NRs (MP: magnetic particles). The MP-P-Au NRs exhibited a red shift in the longitudinal absorbance band compared with that of the as-prepared Au NRs. C6 glioma cells were incubated with MP-P-Au NRs, followed by 2 min of irradiation using a 2 W/cm^2 808-nm CW laser, which resulted in the selective destruction of cells in the irradiated region. In the *in vivo* studies, the MR and PA images were improved by using magnetic targeting compared with the images obtained without magnetic targeting. C6 tumor-bearing mice were intravenously injected with MP-P-Au NRs, and were subsequently subjected to magnetic targeting and irradiation using an 808-nm CW laser with a 2-W/cm^2 power density for 3 min. Although the tumor was not completely inhibited, only a 284% tumor volume increase occurred during treatment, whereas the group treated with NIR irradiation without MP-P-Au NRs exhibited a 1137% increase in volume.
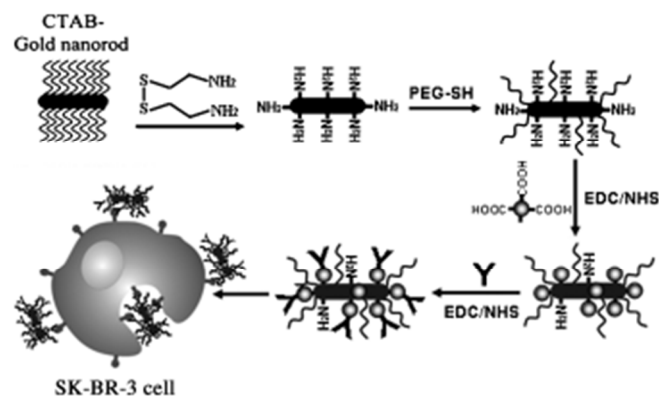
Fig. 3. The formation of antiHER-Au NR@Fe$_3$O$_4$ occurred in the following sequence: CTAB layer on Au NRs replaced with cystamine → stabilized with the SH-PEG → carboxyl groups in Fe$_3$O$_4$ conjugated with amines in cystamine → remaining carboxyl groups in Fe$_3$O$_4$ conjugated with herceptin to form antiHER-Au NR@Fe$_3$O$_4$ → antiHER-Au NR@Fe$_3$O$_4$ targeted to cancer cells (Reprinted with permission from ref. 16. Copyright *Angew. Chem. Int. Ed.*, 2009).

B.3. Drug delivery

Previous studies on the chemotherapy revealed that tissue heating prior to administering the chemotherapy enhances the cytotoxicity by chemotherapy.[18–22] For example, L1210/0 mouse cells were incubated in a water bath maintained at 41.5° C in which cisplatin was administered, which resulted in enhanced cell death compared with that of the cells treated using chemotherapy only.[19] The inhibitory concentration 50 (IC50: the concentration of the drug responsible for the inhibition of 50% of the cancer cell population) value reduced by 4 times compared with that produced when administering chemotherapy without heating. These results were verified by the enhanced uptake and binding of the drug with the DNA. In this context, studies have been conducted to deliver the drugs using photothermal transducers such as Au NRs to achieve simultaneous heating and drug delivery.

Based on these results, Hauck *et al.*[1] administered photothermal heating using Au NRs combined with chemotherapy by using the anticancer drug, cisplatin (the cisplatin was not conjugated with the Au NRs). The Au NRs were synthesized using the seed-mediated process with the aid of CTAB. The Au NRs were coated with poly(4-styrenesulfonic acid) using electrostatic attraction. Polydiallyldimethylammonium chloride (PDADMAC) was deposited over the negatively charged PSS using electrostatic interaction to form PDADMAC-Au NRs. For the *in vitro* analysis, OCI AML3 human myeloid leukemia cells were incubated with PDADMAC-Au NRs for 12 h. Cisplatin was then added to the medium incubated with OCI AML3 cells before undergoing 810-nm laser irradiation. The cytotoxicity analysis revealed that the OCI AML3 viability of chemotherapy combined with PTT was 78% less than that exhibited by using chemotherapy alone, 84% less than the treatment using PTT alone, and 73% less than the calculated cell viability of the combined chemotherapy and PTT conducted using

the Hans method.[23] The efficiency of this type of therapy proved the synergistic effect of the combination therapy involving PTT and chemotherapy. Similar to aforementioned study, the enhanced cytotoxicity effect of chemotherapy combined with photothermal heating was demonstrated using Au NRs and anticancer drug doxorubicin (DOX)-loaded liposomes.[24] The CTAB coating on the Au NR was removed by replacing it with PEG to form Au NR@PEG. The DOX was loaded in the temperature-sensitive liposome (TSL) and temperature-insensitive liposome (TIL) to form TSL$_{DOX}$ and TIL$_{DOX}$, respectively. TSL$_{DOX}$ exhibited a 60% drug release in response to the heat, whereas TIL$_{DOX}$ did not demonstrate such behavior. The Au NR@PEGs and the DOX-loaded liposomes were added separately and were not conjugated together in the therapeutic analysis. MDA-MB-435 human melanoma tumor cells were treated using free DOX, TSL$_{DOX}$, and TIL$_{DOX}$ at 80 µg/mL DOX concentrations followed by the addition of Au NR@PEGs to maintain the final gold ion concentration at 7 ppm. The groups to be treated with NIR irradiation were exposed to an 810-nm diode laser using a power density of 0.75 W/cm^2. The cytotoxicity analysis confirmed that the Au NRs-mediated PTT increased the cytotoxicity of free DOX significantly. Similarly, the Au NR-mediated PTT also enhanced the TSL$_{DOX}$-mediated chemotherapy. These results indicated that the Au NR-mediated photothermal therapy aided in the release of the drug from the TSL, whereas, such enhanced Au NR-mediated chemotherapy was not observed for TIL$_{DOX}$ because the DOX may not have been released for the TIL$_{DOX}$ liposomes. For the *in vivo* trial, the mice bearing MDA-MB-435 tumors were injected with Au NR@PEGs, which were allowed to circulate and accumulate in the tumor for 72 h. After 72 h, the mice were individually injected with free DOX, TSL$_{DOX}$, and TIL$_{DOX}$, followed by 810-nm laser irradiation with a power density of 0.75 W/cm^2. DOX uptake efficiency was monitored using fluorescence intensity. The results indicated that TSL$_{DOX}$ delivered using Au NR-assisted photothermal hyperthermia resulted in 12 times more drug accumulation in the tumor than the free DOX delivered using the Au NR-assisted photothermal effect did. This may have been caused by the short half life of the free drug (5 min) in comparison to the long circulation time of 3 h for the liposomes. In addition, TIL$_{DOX}$ delivered using Au NR-assisted photothermal hyperthermia also resulted in the enhanced uptake. Although TIL$_{DOX}$ exhibited an enhanced uptake, TSL$_{DOX}$ exhibited statistically greater uptake.

Despite the therapeutic advantages of combining PTT with chemotherapy demonstrated in the aforementioned examples, this type of therapy has the drawback of the drug not being tethered to the nanoparticles. Understanding that tethering the drug to the nanocarrier provides more control over the time and dose used, and the area targeted in the combination therapy. Zhong *et al.* loaded the hydrophobic drugs into the photothermal transducer Au NRs using temperature-sensitive caprolactone conjugated polymerblock polymer, poly(ethylene glycol)-b-poly(ε- caprolactone) (denoted as amP : amphiphilic polymer).[25] The Au NRs were mixed with amP to form micelle around the Au NR, denoted as Au NR@amP in Fig. 4. DOX was loaded into the hydrophobic component of the Au NR@amP to yield DOX-Au NR@amP. This thermosensitive micelle exhibited only a 2.5% drug release in 1 h without laser

irradiation. In contrast with 5 min of 808-nm diode laser irradiation using a power density of 0.25 W/cm^2, approximately 40% of the drug was released. The drug release further increased up to approximately 70% in the subsequent cycle of laser irradiation. The cell viability of MCF 7 human breast cancer cells incubated with DOX-Au NR@amPs, followed by 808-nm laser irradiation with a power density of 0.2 W/cm^2, dropped to 45%, whereas DOX-Au NR@amPs that were not exposed to the laser remained nontoxic. To develop a thermosensitive fastener to hold the drugs, DNAs were used as the reservoir to hold the anticancer drug DOX, and drug release behavior was observed when applying Au NR-assisted laser heating.[26] DNA with $(CGA)_8/(TCG)_8$ was designed; $(CGA)_8$ was the capture strand with a 5' thiol end used to bind with Au NRs through thiol-gold binding. Complementary to the capture strand was TCG_8, the 5' end of which was conjugated with NH_2-terminated PEG-folic acid (PEG-FA) through amide bonding to form FA-Au NR@DNA. FA-Au NR@DNAs were loaded with the DOX by intercalating DOX with the DNA sequence to form FA-Au NR@DNA-DOX, as shown in Fig. 5. KB human nasopharyngeal epidermoid carcinoma cells were incubated with FA-Au NRs@DNAs and FA-Au NRs@DNA-DOX, followed by irradiation applied using an 808-nm diode laser with a power density of 600 mW. The effect of PTT demonstrated by the FA-Au NR@DNAs resulted in 34% cell viability, whereas the effect of the combined chemotherapy and PTT indicated by the FA-Au NR@DNA-DOX was an 11% cell viability. BALB/c mice with the KB xenograft tumor were intratumorally injected with FA-Au NR@DNAs and FA-Au NR@DNA-DOX and exposed to 808-nm laser irradiation with a power density of 600 mW. The FA-Au NR@DNA and FA-Au NR@DNA-DOX groups compared with the PBS injection group exhibited a 51% and 65% reduction in tumor volume, respectively, which was caused by the PTT and combination (PTT and chemotherapy) therapy.
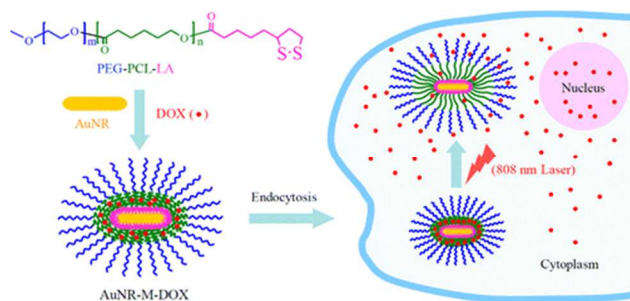

Fig. 4. Au NRs were mixed with amphiphilic block polymer poly(ethylene glycol)-b-poly(ε-caprolactone) to form amP (amP: amphiphilic polymer) micelle around the Au NRs, and hydrophobic doxorubicin drugs were loaded to administer combined chemotherapy and PTT (Reprinted with permission from ref. 25. Copyright *Biomacromolecules*, 2013).

Recently, mesoporous silica grown on Au NRs (Au NR@MS) was developed to serve as a drug reservoir for drug delivery.[27] The pores in the Au NR@MS were loaded with anticancer drug DOX and closed using DNA, but could be opened photothermally for drug delivery. Au NRs were prepared using the seedless growth method. The mesoporous silica was grown on the

Au NRs with CTAB as the soft template to form Au NR@MSs. After the pores of the Au NR@MSs were loaded with DOX, the pores were closed with the thiolated duplex DNAs by Au-thiol conjugation, denoted as dsDNA-Au NR@MS-DOXs. A549 human lung cancer cells incubated with dsDNA-Au NR@MS-DOXs were irradiated using an 808-nm laser with a power density of 1.5 W/cm^2 to achieve 50% cell destruction. The Au NRs in dsDOX-Au NR@MS-DOXs were heated to dehybridize the DNAs photothermally and subsequently induce NIR-controlled drug delivery. Contrarily, A549 cells incubated with Au NR@MSs and irradiated with an 808-nm laser with a power density of 1.5 W/cm^2 exhibited more than 90% cell viability. Similarly, the A549 cells incubated with dsDNA-Au NR@MS-DOX and not subjected to laser irradiation exhibited greater than 90% cell viability. Thus, these Au NR@MSs accompanied by DNAs serving as gatekeepers with the assistance of NIR laser irradiation provided a platform for remotely controlled chemotherapy.
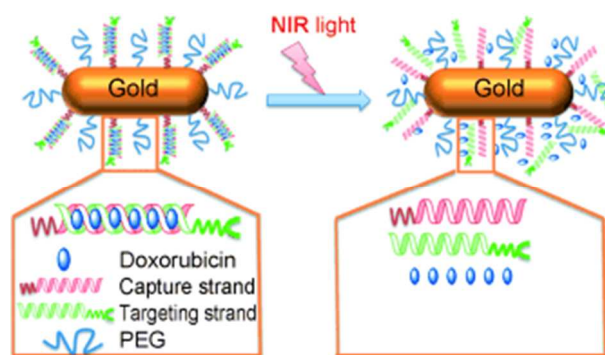

Fig. 5. DNA-assembled Au NRs served as the drug reservoirs, which released the drugs using the external NIR stimuli (Reprinted with permission from ref. 26. Copyright *Angew. Chem. Int. Ed.*, 2012).

B.4. Photodynamic therapy

Several photodynamic agents possess excitation energy in the NIR region. Thus, when photosensitizing dye is coated on Au NRs, the Au NRs can transport the photosensitizing dye to facilitate PDT, and the NIR excitation source can be used to generate heat photothermally for conducting PTT. Kuo *et al.* demonstrated this concept by loading ICG, a photosensitizing dye, on Au NRs to administer both PTT and PDT using NIR excitation.[28] Au NRs were synthesized using the seedless growth method. The CTAB-capped Au NRs were coated with poly(styrene-*alt*-maleic acid) (PSMA) through electrostatic interaction to form Au NR@PSMA. Au NR@PSMA was loaded with ICG using π-π staking to form Au NR@PSMA-ICG. To achieve cancer-cell targeting, antiEGFR antibodies were conjugated on Au NR@PSMA-ICG using electrostatic interaction, which yielded antiEGFR-Au NR@PSMA-ICG. To determine the *in vitro* therapeutic efficiency, antiEGFR-Au NR@PSMA-ICGs, Au NR@PSMAs, and ICG were individually incubated with EGFR overexpressing A549 cancer cells and irradiated using an 808-nm diode laser with a power density of 22.5 W/cm^2 for 2 min. A549 cancer cells incubated with antiEGFR-Au NR@PSMA-ICGs, Au NR@PSMAs, and ICG exhibited approximately 55%, 93%, and 69% cell viability, which

corresponded to the effect of applying the combination (PTT + PDT) therapy, PTT, and PDT, respectively. Metal-enhanced fluorescence imaging of ICG was also verified for antiEGFR-Au NR@PSMA-ICGs, which contributed for the function of the IR fluorescence imaging in addition to the combination therapy, as shown in Fig. 6.
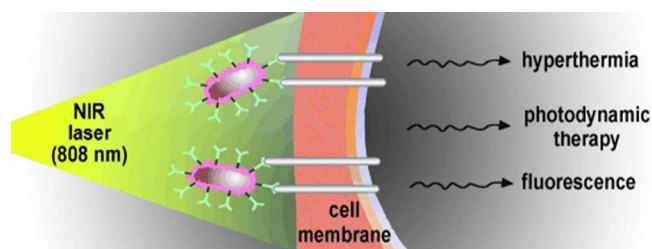

Fig. 6 Triple function (PTT, PDT, and IR fluorescence imaging) delivered by Au NRs loaded with photodynamic dye ICG (Reprinted with permission from ref. 27. Copyright *Angew. Chem. Int. Ed.*, 2010).

C. Au nanoshell

An Au nanoshell is a thin layer of Au containing dielectric space at the core and exhibits the optical absorbance maxima in the NIR region. Therefore, this nanomaterial can serve as a photothermal transducer. The optical absorption cross-section of a Au nanoshell is 6 times more than the NIR-absorbing ICG,[29] which makes the Au nanoshell a strong NIR absorber. Furthermore, the appreciable photostability of Au nanoshells encourages their applications in the field of biology. This Au nanoshell can be grown using various dielectric materials: (1) Au nanoshells grown in the presence of dielectric silica nanoparticles; (2) Au nanoshells grown in the presence of dielectric polymer nanoparticles; and (3) Au nanoshells grown using the galvanic exchange reaction involving electron donors such as Ag nanospheres, which creates a hollow dielectric core space within the Au nanoshell. The applications of these materials in photothermal therapy and drug delivery are discussed in the following section.

C.1. Photothermal therapy

The ability of the Au nanoshell to absorb NIR is used to administer PTT in biomedical applications. In addition to the NIR-absorption capability, Au nanoshells also exhibit the scattering property which can be used in imaging. Loo *et al.* applied the abilities of Au nanoshells to scatter and absorb NIR to conduct imaging and therapeutic studies, respectively.[30] Au nanoshells were synthesized using a 2-step process: (1) Au seeds were placed on the silica nanosphere using electrostatic attraction; and (2) isolated Au particles were grown on the silica into a continuous Au shell to form a Au nanoshell corresponding to SiO_2@Au. This Au nanoshell was functionalized using the targeting antibody antiHER2. To perform this functionalization, the antiHER2 was conjugated to the PEG containing the distal thiol end, forming PEG-conjugated antiHER2 to attach the Au nanoshell through Au-S binding, denoted as antiHER2-Au nanoshell. In the *in vitro* tests, SKBr 3 human breast

adenocarcinoma cells were treated with antiHER2-Au nanoshells, and exposed for 7 min to an 820-nm NIR laser with a power density of 0.008 W/cm². This led to the destruction of the cells exposed to the antiHER2-Au nanoshells with the laser. Fluorescence microscopy revealed a round patch of live cells, stained with green calcein, localized outside the NIR zone, as shown in Fig. 7. In addition, the cells exposed to nontargeting Au nanoshells and had undergone laser irradiation did not die because of the low uptake of Au nanoshells. This difference in uptake was reflected in the imaging results, in which SKBr 3 cells incubated with antiHER2-Au nanoshells showed substantially increased scattering than the cells treated with
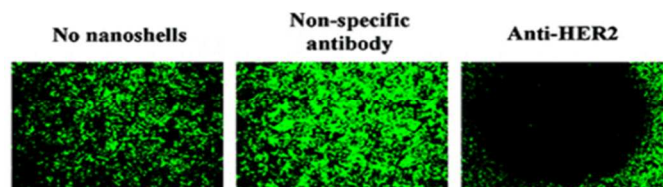

Fig. 7. Site-specific SKBr 3 breast cancer cell death occurred on antiHER2-coated Au nanoshells when 0.008 W/cm² laser irradiation was used, whereas the SKBr 3 breast cancer cells treated with no Au nanoshells or Au nanoshells without an antibody target exposed to laser irradiation did not die (Reprinted with permission from ref. 30. Copyright *Nano Lett.*, 2005).

nontargeting Au nanoshells did. Similarly, targeted PTT was performed by coating the Au nanoshell (SiO_2@Au) with A54 targeting peptides.[31] To conjugate the Au nanoshell with the targeting peptides, the A54 (short peptide comprising the AGKGTPSLETTP sequence) peptides were modified with cysteine, an amino acid containing a thiol group. This cysteine containing A54 peptides conjugates to the Au nanoshell through Au-S binding, denoted as A54-Au nanoshell. The ability of A54-Au nanoshells to target liver cancer cells was demonstrated using HL-7702 normal liver cells (no affinity to A54 peptide), and BEL-7404 and BEL-7402 human heptacellular cancer cells (affinity to A54 peptide). These cells incubated with A54-Au nanoshells were exposed to an NIR laser for 7 min of irradiation and monitored using a fluorescent microscope. The fluorescent images of the live cells stained with green fluorescence showed no fluorescence in the BEL-7404 and BEL-7402 cancer cells, but green fluorescence was exhibited by the normal HL-7702 cells. This indicates that A54-Au nanoshells had more uptake by the BEL-7404 and BEL-7402 cells with an affinity for A54 peptides, which caused a significant amount of cancer cells to be killed by NIR irradiation, whereas the A54-Au nanoshells were barely uptook by the normal HL-7702 cells with no affinity for A54 peptides, and no cell destruction was caused by NIR laser irradiation. Finally, the uptake and the effect of the A54-Au nanoshells and laser irradiation on the BEL-7404 cells were studied using TEM. The BEL-7404 cells treated with the A54-Au nanoshells exhibited a micro villi-like structure in the cell membranes and nuclei. The NIR laser irradiation on the cells caused shrinking and blebs began to appear. Based on the ability of the Au nanoshell (SiO_2@Au) to process imaging and therapy in the *in vitro* conditions, the Au nanoshell capacity was further demonstrated using *in vivo* imaging and therapy.[32] To prevent the immune response from occurring and

enhance Au nanoshell circulation for *in vivo* applications, the Au nanoshell was coated with PEG by using thiolated PEG, denoted as PEG-Au nanoshell. The mice bearing CT-26 murine colon tumors were intravenously injected with the PEG-Au nanoshells. Before imaging, the PEG-Au nanoshells were allowed to circulate for 20 h, after which the tumor and normal tissue images were captured using optical coherence tomography (OCT) imaging. As expected, the PEG-Au nanoshell signal appeared in the tumor tissues, which was absent in the normal tissues. After OCT imaging, the tumors were exposed to an NIR laser with a power density of 4 W/cm^2, which led to a significant reduction in tumor size and an increase in the survival percentage, as shown in Fig. 8.
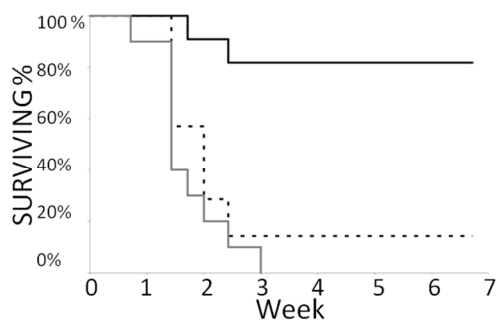

Fig. 8. PEG-coated Au nanoshells showing an increased survival percentage (y-axis: survival percentage from 0% to 100%; x-axis: weeks after laser irradiation was performed) (Reprinted with permission from ref. 32. Copyright *Nano Lett*., 2007)

In a dynamic approach for the Au nanoshell to reach the tumor site, monocytes with a natural instinct to reach the tumor hypoxia region were introduced to enable targeted delivery.[33] The Au nanoshell (SiO$_2$@Au) phagocytosed by the monocytes (Monocyte$_{Au\ nanoshell}$) remained inactive when not subjected to irradiation, but demonstrated ablation when a fs pulse laser with a wavelength of 754 nm and 1.54 W of power was used. To demonstrate the ability of Monocyte$_{Au\ nanoshell}$ to reach the tumor hypoxia region, which is inaccessible during chemotherapy, an *in vitro* model of a tumor spheroid with the hypoxia tumor environment was created by culturing T47D breast cancer cells on agarose. This spheroid contains core necrotic cells surrounded by hypoxia cells, which is the middle layer of the spheroid, and the peripheral normoxia cells are also present surrounding the hypoxia cells. The spheroids were incubated with the monocytes and Au nanoshells in a cell culture plate, which caused *in situ* Monocyte$_{Au\ nanoshell}$ formation. Thus, the as-formed Monocyte$_{Au\ nanoshell}$ perpetuated the tumor spheroids to reach the interior hypoxia cells that were margined around the necrotic cells, as shown in Fig. 9 (the margin of hypoxia and the necrotic cells is marked with a white line). When the fs laser was employed, Monocyte$_{Au\ nanoshell}$ caused PTT ablation, resulting in the death of T47D cells.
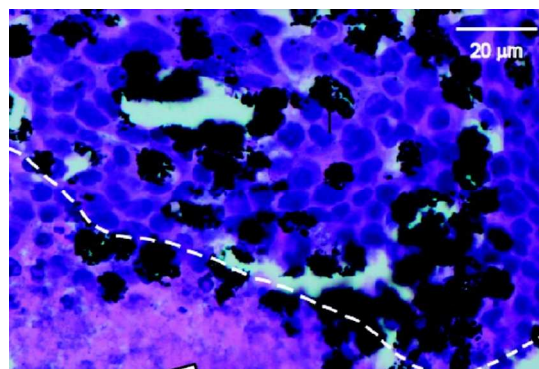

Fig. 9. Infiltration of the Au nanoshell -laden macrophages (stained black) into the tumor spheroids (the white dotted line divides the necrotic cells (stained pink) from viable cells (stained purple)) (Reprinted with permission from ref. 33. Copyright *Nano Lett*., 2007).

At the next step in the development of Au nanoshells, the nonfunctional silica core motivates researchers to replace it with a functional dielectric core to conserve NIR absorbance while maintaining the functionality of the substitute. Ke *et al*. developed a polymer sphere to substitute the silica core and serve as the ultrasound contrast agent.[34] Poly(lactic acid) (PLA), which is biodegradable and possesses an ultrasound signaling capability, was investigated in this study. Microcapsules of the PLA were made using polyvinyl alcohol through double emulsion method. The zeta potential of the microcapsule was determined to be negative (-25 mV), hence the microcapsule was coated with poly(allyl amine hydrochloride) to produce a positive charge (+2 mV). This positive surface charge helps the negatively charged citrate-capped Au seeds be electrostatically adsorbed on the microcapsule surface. The isolated Au seeds were then grown to cover the microcapsule surface to form microcapsule-coated Au nanoshell, denoted as MC-Au nanoshell. The ability of MC-Au nanoshells to serve as the ultrasound imaging contrast agent was demonstrated in *in vivo* studies. In the *in vivo* ultrasound imaging process, MC-Au nanoshells were intravenously injected into rabbits, and the enhancement was observed in the kidney image. These MC-Au nanoshells show the broad absorption band from 650 nm to 900 nm. The aqueous dispersion of 500 ppm of MC-Au nanoshells, irradiated by using an 808--nm diode laser with a power of 2 W, produced a 25° C increase in temperature in 10 min. In PTT, HeLa cells treated with MC-Au nanoshells were irradiated using an 808-nm laser with a power density of 8 W/cm^2 for 10 min. The destruction of the cells was observed using fluorescence imaging in combination with live-cell staining. The distinct zone containing the live cells was observed outside the irradiation zone. The quantification of cell viability revealed that the HeLa cells treated with MC-Au nanoshells exhibited less than 20% cell viability under laser irradiation, and more than 80% cell viability without laser irradiation.

NIR absorbance by using the dielectric core containing metal shell was achieved by the direct growth of metal on a silica or polymer core, as demonstrated in the aforementioned studies. In addition, a hollow dielectric space at the center was developed by

Xia *et al.* using the galvanic exchange method to create a Au nanocage (Au NC).[35] Au NCs were synthesized by performing reduction using sacrificial Ag nanocubes as the templates. The Au NCs with a 45-nm edge length and 3.5-nm wall thicknesses exhibits absorbance at the 810-nm wavelength. The photothermal effect of the Au NCs was demonstrated on SK-BR-3 human breast cancer cells, which overexpress the EGFR. In this study, Au NCs were functionalized using the NHS-activated PEG combined with sulphide bonding. The activated PEG was then conjugated with the antiEGFR through amide bonding, denoted as antiEGFR-Au NCs. SK-BR-3 was treated with the antiEGFR-Au NCs, followed by irradiation using a Ti: sapphire 810-nm pulse laser at a power density of 1.5 W/cm^2 for 5 min, and the SK-BR-3 cells were photothermally destroyed. This was observed using a fluorescence microscope after performing calcein staining, in which the live cells stained to produce green fluorescence around the black dead cell zone caused by laser irradiation. The increase in the irradiation laser power density caused the zone area of SK-BR-3 cell destruction to increase proportionally, as shown in Fig. 10.[36]
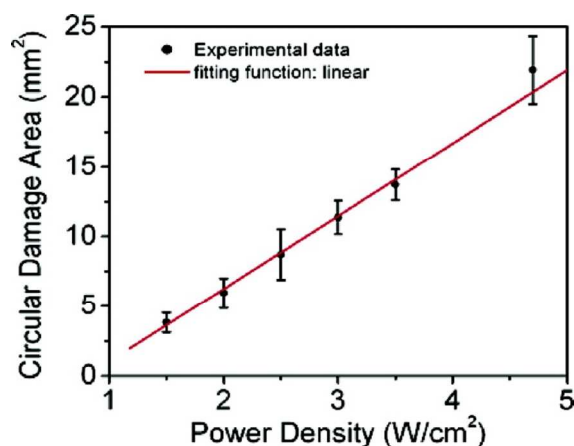

Fig. 10. Power dependent increase in the zone area exhibiting tumor cell death derived from Au NCs exposed to an NIR laser (Reprinted with permission from ref. 36. Copyright *Nano Lett.*, 2007).

In vivo studies on PTT performance have been conducted using Au NCs.[37] Herein, Au NCs were PEGylated with hetero bifunctional poly(ethylene glycol), with one end containing sulfhydryl and the other end containing a methoxy group. The sulfhydryl end facilitates the conjugation of the PEG with Au NCs through gold thiol binding to form PEG-Au NCs. The PEG in the PEG-Au NCs enabled them to circulate in blood for an extended period. Before *in vivo* studies were conducted, the photothermal properties of PEG-Au NCs were examined by subjecting PEG-Au NCs with a particle concentration of 10^9 particles/mL to an 808-nm diode laser with a power density of 0.5 W/cm^2. This caused an increase of 10° C within 5 min, whereas without the PEG-Au NCs, only a 2–3° C increase occurred. Subsequently, PEG-Au NCs were injected intravenously into the mice bearing U87wtEGFR human glioblastoma cells. The PEG-Au NCs were allowed to accumulate in the tumor for 72 h post-injection. The PEG-Au NCs accumulated in the tumor passively through the enhanced permeability and retention

effect. At the end of 72 h, the tumor was irradiated with an NIR laser with a power density of 0.7 W/cm^2 for 10 min. This was monitored with an IR camera, which showed that the temperature of the tumor increased to 50° C within 1 min and then leveled off at 54° C after 2 min for the remainder of the 10 min duration. The metabolic change caused by PTT was studied using F-fluorodeoxyglucose positron emission tomography (F-FDG-PET) imaging. The uptake of F-fluorodeoxyglucose (F-FDG), a contrast agent for PET imaging, depends on cell metabolic activity. When the tumor cells die after PTT is administered, a reduction in F-FDG uptake by the dead tumor cells (no metabolic activity) is expected. Accordingly, the image produced when irradiation was applied showed a 70% reduction in metabolic activity when compared with the image produced when no irradiation was used, as shown in Fig. 11. This change did not occur when the treatment involving saline injection followed by NIR laser irradiation was administered. The histopathalogical analysis of the tumor section of an animal injected with PEG-Au NCs indicated that necrosis, karyorhectic, karyolysis, pyknosis, karyorrhexis, karyolysis, and interstitial edema had occurred. Such symptoms were absent in the tumor sections obtained from the animals that were not treated with PEG-Au NCs. Recently, by adopting the aforementioned strategy to create a hollow interior using the replacement reaction, the silver tetrahedron was replaced with Au to form a Au tetra-nanocage (AuTNC).[38] The photothermal properties of AuTNCs were tested using a range of AuTNC concentrations and exposing the AuTNCs to an 808-nm laser with a power density of 2 W/cm^2; when the optimal concentration of 500 pmol was used, the temperature increased from 28° C to 47.3° C in 15 min. In *in vitro* PTT, A549 and SK-BR-3 cancer cells were incubated with AuTNCs for 3 h, followed by 808-nm laser irradiation with a power density of 2 W/cm^2. After laser irradiation, the cells were stained to identify the live and dead cells. The cells treated with the AuTNCs followed by NIR irradiation exhibited apparent cell death, whereas the cells treated with either AuTNCs or NIR irradiation alone were not destroyed, which confirmed the photothermal efficiency of AuTNCs.
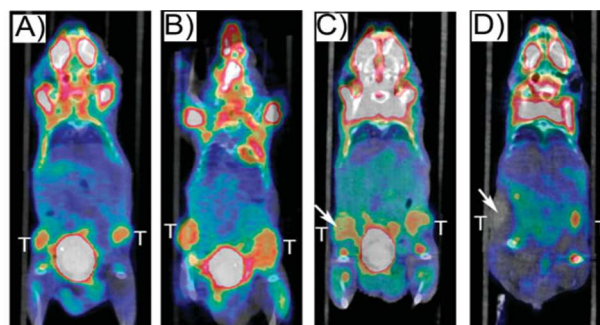

Fig. 11. *In vivo* PTT effect on mice bearing tumors monitored using F-FDG PET/CT imaging; from left to right, (i) Saline was injected and no irradiation was used, (ii) Au NCs were injected and no irradiation was used, (iii) Saline was injected and irradiation was administered. The arrow shows the metabolic activity did not decrease compared with that of the group not subjected to irradiation, and (iv) Au NCs were injected and irradiation was administered. The arrow shows the metabolic activity decreased compared with that of the group not subjected to irradiation (Reprinted with permission from ref. 37. Copyright *Small*, 2010.)

To design multifunctional Au nanoshells with MRI function, a sandwich structure was designed using a silica core coated with iron oxide nanoparticles and then decorated with a Au shell.[39] Silica nanoparticles were prepared using the Stöber method,[40] followed by 3-aminopropyltrimethoxysilane (APTES) coating. Oleic acid-capped iron oxide nanoparticles were prepared in octyl ether solvent, and were ligand exchanged with 2-bromo-2-methylpropionic acid to disperse the nanoparticles in water. The iron oxides were deposited on the APTES-coated silica by employing amide binding ($SiO_2@Fe_3O_4$). An electrostatic force was applied to make the remaining silica surface of $SiO_2@Fe_3O_4$ interact with the gold seeds, and then the isolated gold seeds were grown into a complete 15-nm-thick shell to form $SiO_2@Fe_3O_4@Au$. The gold shell of $SiO_2@Fe_3O_4@Au$ exhibits broad absorbance from 700 nm to the NIR range, and the T_2-weighted images of $SiO_2@Fe_3O_4@Au$ shows concentration-dependent darkness. In the *in vitro* experiments, the targeting antibody antiHER2/neu was tethered to $SiO_2@Fe_3O_4@Au$, denoted as antiHER2-$SiO_2@Fe_3O_4@Au$. AntiHER2-$SiO_2@Fe_3O_4@Au$ was tested against antiHER2/neu-positive SKBR3 human breast cancer cells and antiHER2/neu-negative A520 lung cancer cells. In the *in vitro* MR images, antiHER2-$SiO_2@Fe_3O_4@Au$ treated with SKBR3 was darker than antiHER2-$SiO_2@Fe_3O_4@Au$ treated with A520 cells was. The T_2 relaxation times of antiHER2-$SiO_2@Fe_3O_4@Au$ treated SKBR3 and A520 cells were 54.8 and 76.9 ms, respectively. In the *in vitro* PTT involving an NIR pulse laser, SKBR3cells treated with antiHER2-$SiO_2@Fe_3O_4@Au$ died when 20 mW was applied, whereas A530 cells treated with antiHER2-$SiO_2@Fe_3O_4@Au$ were destructed when 60 mW was applied. In a similar approach to fabricating multifunctional nanoshells, iron oxide nanoparticles served as cores, over which silica with a thickness of a few nanometers was coated and then with Au to form a Au shell.[41] The iron oxide core was coated with amorphous silica using the sol gel method to form $Fe_3O_4@SiO_2$, and then $Fe_3O_4@SiO_2$ was modified using APTES to produce a positively charged amine. This positively charged amine facilitates the firm attachment of the negatively charged citrate-capped Au seeds. The Au seeds then nucleated and grew into a continuous shell to form $Fe_3O_4@SiO_2@Au$. $Fe_3O_4@SiO_2@Au$ was conjugated with MeO-PEG-SH through gold thiol bonding (PEG-$Fe_3O_4@SiO_2@Au$). The absorbance spectrum of PEG-$Fe_3O_4@SiO_2@Au$ showed the peak stretching from 825 nm to 910 nm in the NIR range. The PEG-$Fe_3O_4@SiO_2@Au$ concentration-dependent images showed a dark T_2-weighted phantom with the increase in the concentration. PEG-$Fe_3O_4@SiO_2@Au$ with a 7.5 x 10^{10} particles/mL concentration that underwent irradiation administered using an 808-nm diode laser with 1 W of power produced a 16.3° C increase in temperature in 5 min. Moreover, a multifunctional Au nanoshell ($Au@SiO_2$) exhibiting trimodal function with PTT, MRI and IR imaging was further developed by Bardhan *et al.*[42] The Au nanoshell surface was coated using the iron oxide nanoparticles, and was then coated with silica. During silica coating, ICG was loaded *in situ*. The absorbance peak of Au nanoshell@$Fe_3O_4@SiO_2$-ICG was observed at 820 nm and exhibited concentration-dependent darkness in the T_2-weighted image. In the *in vitro* experiments, Au nanoshell@$Fe_3O_4@SiO_2$-ICG was conjugated with the antiHER2 that can target the HER2-positive SK

BR3 cancer cell line. To achieve this conjugation, Au nanoshell@$Fe_3O_4@SiO_2$-ICG was coated with 3-(mercaptopropyl)-triethoxysilane to cause thiol termination. Au nanoshell@$Fe_3O_4@SiO_2$-ICG was then modified with streptavidin maleimide through thioester bonding. Biotinated antiHER2 was conjugated to this streptavidin through streptavidin biotin bonding (antiHER2-Au nanoshell@$Fe_3O_4@SiO_2$-ICG). In the *in vitro* magnetic resonance imaging process, antiHER2-Au nanoshell@$Fe_3O_4@SiO_2$-ICG was treated with HER2-positive SKBR3 and HER2-negative MDA-MD-231 human breast adenocarcinoma cells. The MR images were then taken by embedding the cells in 0.5% agarose gel. The SKBR3 cells produced intense MR signals compared with those of the MDA-MD-231 cells. In the *in vitro* IR images, antiHER2-Au nanoshell@$Fe_3O_4@SiO_2$-ICG treated with SKBR3 cells exhibited IR fluorescence, whereas IR fluorescence was absent in antiHER2-negative MDA-MD-231 cells treated with antiHER2-Au nanoshell@$Fe_3O_4@SiO_2$-ICG. This confirmed the targeting and IR fluorescence of antiHER2-Au nanoshell@$Fe_3O_4@SiO_2$-ICG. In *in vitro* PTT, the SKBR3 cells treated with antiHER2-Au nanoshell@$Fe_3O_4@SiO_2$-ICG and exposed to an 808-nm diode laser with a power density of 3.72 W/cm^2 were completely destroyed, whereas fewer HER2-negative MDA-MD-231 cells treated with nanoparticles exposed to the laser were destroyed.

For the comparison of Au NR, Au nanoshell, and hollow Au nanoshell (HAu nanoshell), PTT performance was investigated by Cheng *et al.*[43] In their studies, the as-prepared Au nanoshells and HAu nanoshells were used without any modification. In case of Au NRs, Au NRs was coated with PSS and polyethyleneimine (PEI) by layer-by-layer (LBL) assembly. Au nanoshell, HAu nanoshell and Au NRs at 8.36 x 10^8 particles /100 μL concentration were used under irradiation with 808 nm CW diode laser of 30 W/cm^2 power density for 7 min and the temperatures rose to 50.2° C, 42.6° C and 32.8° C, respectively. The minimum number of particles required for the photothemal effect on A549 lung, HeLa cervical and TCC baldder cancer cells showed the order of Au nanoshells < HAu nanoshells < Au NRs. This infers that the photothermal effect was more effective in Au nanoshells than HAu nanoshells and Au NRs.

C.2. Drug delivery

Nanoparticle-based drug delivery is becoming crucial in cancer therapy because of the enhancement in therapeutic effect, compared with that produced by the free drug. In this context, controlled drug delivery enhances treatment quality by preventing a nontarget effect from occurring through spatiotemporal activation. This spatiotemporal control is established using a photothermal transducer. In addition, the photothermal transducer provides the advantage of combining chemotherapy and PTT to achieve therapeutic efficiency. In this subsection, various designs for controlled drug delivery using Au nanoshell are discussed.

You *et al.* demonstrated NIR-triggered drug delivery using a HAu nanoshell. [44] The HAu nanoshells was synthesized using the galvanic exchange process with cobalt nanoparticles serving as the electron donor; the cobalt nanoparticles were synthesized by

reducing cobalt chloride using borohydrate as the reducing agent. To these cobalt nanoparticles, the Au ions in $HAuCl_4$ were reduced to form HAu nanoshells. The synthesized HAu nanoshells were stabilized by conjugating methoxy-PEG-SH using gold thiol bonding to form PEG-HAu nanoshells. The PEG-HAu nanoshells were then loaded with DOX to form DOX-PEG-HAu nanoshells. At this drug loading step, the PEG to Au ratio was varied to achieve the highest possible DOX loading. DOX-PEG-HAu nanoshells with a concentration of 7 x 10^{10} particles/mL exposed to an 808-nm laser with a power density of 5 W/cm^2 for 10 min exhibited a 30° increase in temperature. NIR-stimulated drug release from DOX-PEG-HAu nanoshells was studied using the laser on/off sequence of an 808-nm laser with a power density of 4 W/cm^2. The *in vitro* examination of DOX-PEG-HAu nanoshells was conducted using MDA-MB-231 human breast carcinoma cells. The florescence image of MDA-MB-231 cells treated with DOX-PEG-HAu nanoshells without laser exposure exhibited DOX fluorescence in the cytoplasms but not in the nuclei. This red fluorescence in the cytoplasm area colocalized with the scattering signal of the DOX-PEG-HAu nanoshells, which was observed using a fluorescence microscope equipped with a dark field condenser. The DOX did not reach the nuclei and was not released from the DOX-PEG-HAu nanoshells. However, the fluorescence image of the MDA-MB-231 cells treated with DOX-PEG-HAu nanoshells that underwent 808-nm laser irradiation with a 1-W/cm^2 power density (using the laser on/off sequence, with 3 min for each sequence) showed DOX fluorescence in the nuclei, indicating that the drug was released after NIR stimulation. The cytotoxicity of DOX-PEG-HAu nanoshells on MDA-MB-231 cells that underwent NIR irradiation caused 86% of the cells to be destroyed when combined PTT and chemotherapy was used, whereas the cytotoxicity of HAu nanoshells alone on the cells that underwent the same amount of NIR irradiation caused only 41% of the cells to be destroyed (PTT only).

NIR-controlled hydrophobic anticancer drug delivery from poly(lactide-co-glycolide) (PLGA) microspheres was conducted using HAu nanoshells.[45] In this demonstration, paclitaxel (PTX)-loaded PLGA microspheres suspended with the HAu nanoshells were prepared using the double emulsion method (PTX/HAu nanoshells MSs, MSs: microspheres). The schematic of the formulation is shown in Fig. 12. The photothermal property of the PTX/HAu nanoshells MSs was studied by performing irradiation using an 808-nm laser with a power density of 4.5 W/cm^2 on the particles concentration of 4.2 x 10^{10} particles/mL, which caused a 23° C increase in temperature. This indicated that the photothermal property of PTX/HAu nanoshell MSs was not compromised by the encapsulation of PLGA over bare HAu nanoshells. The controlled release behavior of the drugs from the PTX/HAu nanoshell MSs was studied using the consecutive on and off sequence of the laser, which was turned on for 5 min and turned off for 1.5 h. The PTX release from the PTX/HAu nanoshell MSs during the first, second, third, and fourth irradiations were 12.6%, 8%, 7.4%, and 6.2%, respectively, whereas the release was ≤ 1 % during the 1.5-h off period. The *in vitro* efficiency of PTX/HAu nanoshell MSs was demonstrated in MDA-MB-231 breast cancer and U87 glioma cells. Among the MDA-MB-231 cells treated using the PTX/HAu nanoshell MSs,

followed by NIR irradiation using an NIR laser with a 2-W/cm^2 power density, 53% of the cells were killed by the combined PTT and chemotherapy effect. Whereas, using HAu nanoshell MSs alone with irradiation killed 11% of the cells when administering PTT effect, and using PTX/HAu nanoshell MSs pre-irradiated with an NIR laser followed by addition of pre-irradiated PTX/HAu nanoshell MSs to the cells caused 21% of the cells to be destroyed when chemotherapy was applied. A similar trend was also observed in the U87 cells. In the *in vivo* studies, mice bearing MDA-MB-231 breast cancer cells were injected with PTX/HAu nanoshell MSs intratumorally and irradiated using a laser power of 1.5 W for 5 min. This tumor progress was controlled for 25 days, whereas tumor progress was controlled for only 19 and 15 days in the group treated using HAu nanoshell MSs with laser irradiation and the group treated using PTX/HAu nanoshell MSs without laser irradiation, respectively. Similar results were reflected in the mice bearing U87 tumor cells. The concept of NIR-stimulated drug delivery from liposomes was also demonstrated using HAu nanoshells. 6-carboxyfluorescein (C6), a fluorescent dye, was used in substitution to the drug.[46] C6 was encapsulated in the liposome made of dipalmitoylphosphatidylcholine. The fluorescence was quenched inside the liposomes. The C6-loaded liposomes also co-encapsulated with PEG-coated HAu nanoshells. The liposome composites irradiated with an fs NIR Ti: sapphire pulse laser with a power density of 2.2 W/cm^2 at an 800-nm wavelength released C6. Immediately after the C6 molecules were released from the liposomes, fluorescence was observed. The liposomes without encapsulated HAu nanoshells did not exhibit a fluorescence signal after laser irradiation. In addition, using an 820-nm CW laser with a power density as high as 89 W/cm^2 did not cause C6 dyes to be released from the liposomes encapsulating the HAu nanoshells. This indicated that the controlled release of the drugs from the liposomes was possible only in the presence of both HAu nanoshells and the fs pulse laser. This study also revealed that the release of drugs from the liposomes occurred through transient cavitation, which was caused by microbubble formation during NIR stimulation. Because the CW laser was not able to create a temperature gradient on the HAu nanoshells encapsulated in the liposomes, microbubbles were not formed and C6 was consequently not released. This concept suggests that a similar controlled-drug-release platform using Au nanoshells and an fs laser can be constructed. Moreover, NIR-stimulated controlled drug release from a smart polymer was achieved using Au NCs.[47] Au NCs were synthesized using the galvanic exchange reaction with a gold ion solution in the presence of Ag nanocubes, which served as the templates for the NCs construction, and poly(vinyl pyrrolidone) (PVP), which served as the capping agent to stabilize the resulting NCs colloids. The PVP on the Au NCs was then replaced with the polymer poly(N-isopropylacrylamide) (pNIPAAm) to form P-Au NCs (P: pNIPAAm). pNIPAAm can stretch or collapse in response to temperatures below or above the low critical solution temperature (LCST), respectively. The controlled release feature of P-Au NCs was demonstrated by loading alizarin dye to form al-P-Au NCs (al: alizarin). The release of alizarin in response to the use of a laser was monitored using the spectroscopic absorbance at 354 nm exhibited by the alizarin. The irradiation of the al-P-Au NCs using an NIR

pulse laser with power densities of 10, 25, and 40 W/cm^2 caused a 5, 14, and 20 µM alizarin release, respectively. In the *in vitro* studies, P-Au NCs were loaded with DOX to form DOX-P-Au NCs. The cancer cells treated with DOX-P-Au NCs, followed by NIR laser irradiation using a power density of 20 mW/cm^2 for 2 and 5 min, exhibited approximately 65% and 55% cell viability, respectively, whereas the cells treated with the laser only or with P-Au NCs exposed to the laser exhibited cell viability greater than 90%.
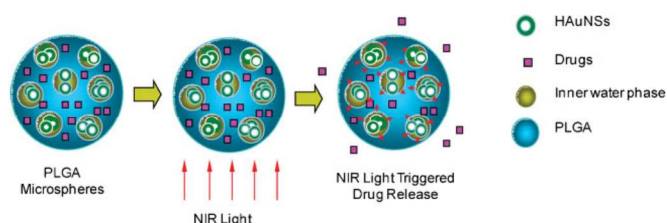

Fig. 12. PLGA encapsulating both HAu nanoshells (HAuNSs) and PTX drugs to form PTX/HAu nanoshell MSs. (Reprinted with permission from ref. 45. Copyright *Small*, 2010.)

In addition to the HAu nanoshell platform, a silica nanorattle structure was also used to study the combination of PTT and chemotherapy.[48] In this study, the gold seeds were placed on silica nanorattles using electrostatic force. The gold seeds nucleated and grew around the nanorattle as a thin shell to form Au nanoshells. The Au nanoshells were PEGylated with methoxy-poly(ethylene glycol)-thiol through gold thiol bonding to form PEG-Au nanoshells. The PEG-Au nanoshells were then conjugated with transferrin, a targeting glycoprotein used for rapidly dividing cancer cells, through amide bonding to form tf-PEG-Au nanoshells. The tf-PEG-Au nanoshells exposed to an 808-nm laser using a power density of 2 W/cm^2 exhibited a 25° C increase in temperature in 10 min. Mice bearing MCF7 human breast adenocarcinoma cells were intravenously injected with tf-PEG-Au nanoshells, which were allowed to accumulate in the tumor for 6 h. Subsequently, the tumors were irradiated using an 808-nm NIR laser with a power density of 2 W/cm^2 for 3 min, which caused the temperature of the tumor to increase from 30.5° C to 45.7° C. The uptake efficiency of tf-PEG-Au nanoshells (with targeting transferrin) by the MCF7 cells compared to the PEG-Au nanoshells (without targeting transferrin) was measured using inductively coupled plasma emission spectrometry. The Au content of the MCF7 cells treated with tf-PEG-Au nanoshells was approximately 15 times more than that of the MCF7 cells treated with PEG-Au nanoshells. The tf-PEG-Au nanoshells were further loaded with docetaxel through a noncovalent interaction, physical adsorption, to form DTX-tf-PEG-Au nanoshells. In the therapeutic cytotoxicity, MCF7 cells treated with DTX-tf-PEG-Au nanoshells were exposed to an 808-nm laser with a power density of 2 W/cm^2 for 3 min. The IC50 value of the DTX-tf-PEG-Au nanoshells that underwent laser illumination was 2.4 nM, which was lower than that of the DTX-PEG-Au nanoshell exposed to the laser (5.5 nM), and that of the free drug DTX (without laser exposure) (7.6 nM). In the *in vivo* tests, the BALB/c mice bearing MCF7 cell tumors were intravenously injected with DTX-tf-PEG-Au nanoshells, followed by irradiation for 3 min in 6 h post-injection

using an 808-nm laser with a power density of 2 W/cm^2. The tumor volume was monitored for up to 17 days. DTX-tf-PEG-Au nanoshells that were exposed to NIR completely controlled the tumor volume, whereas the group treated with the free drug DTX alone or with the DTX-PEG-Au nanoshells (with NIR irradiation) exhibited initial tumor volume control, but the tumors began to grow from the 14th day.

D. Other Au related nanomaterials and their composites

Although the aforementioned Au NRs and Au nanoshells dominate the field of NIR-controlled cancer therapy, other Au-related nanomaterials that can absorb NIR radiation are designed with different shape or structure into shell-like structure. This section describes several of these materials.

D.1. Photothermal therapy

Recently, Tsai *et al*. presented 50-nm rod-in-shell structures that can absorb NIR radiation in the second biological window (1000–1300 nm).[49] Plasmon hybridization was used to observe the absorbance by introducing a dielectric hollow gap between the core rod and a shell made of noble metal. Au NRs were synthesized using the seedless method. The Au NRs were then coated with a Ag shell by reducing AgNO$_3$ with ascorbic acid (AA) in the presence of CTAB and PVP to form Au NR@Ags. This Ag shell was galvanically replaced to yield a Au/Ag alloy shell with the addition of HAuCl$_4$ in the presence of CTAB and AA. The galvanic reaction facilitated the synthesis of the Au/Ag alloy shell by sacrificing the Ag shell, which resulted in the dielectric hollow gap between the Au NR core and Au/Ag alloy shell. This structure containing a dielectric hollow space caused the shell to produce inner and outer plasmons. Two possible interactions could have occurred: (1) interaction between the inner shell plasmon and the outer shell plasmon (shell plasmon); and (2) interaction between the core rod plasmon and the inner shell plasmon (cavity plasmon). The symmetric and asymmetric interactions in the shell caused bonding and antibonding modes to occur, respectively. Bonding results in low-energy absorption and antibonding results in high-energy absorption. In the cavity, the symmetric interaction caused antibonding to occur, which resulted in high-energy absorption, and the asymmetric interaction caused bonding to occur, which resulted in low-energy absorption. Therefore, four modes of hybridization were expected to have: bonding-bonding, bonding-antibonding, antibonding–bonding and antibonding–antibonding. The hybridization modes were most pronounced in the rod-in-shell with narrow gap (e.g., 2 nm), compared with those exhibited in the rod-in-shell with wider gap (e.g., 6.5 nm). The pronounced hybridization resulted in the absorbance peak maxima occurred at 1100 and 1280 nm in the second biological window; therefore, the use of this rod-in-shell structure in PTT was tested using a 1064-nm diode laser and the performance was compared using different gaps of 2 and 6.5 nm. To evaluate the photothermal properties, the rod-in-shells were irradiated using a 1064-nm laser with a power density of 3 W/cm^2. The temperature of the rod-in-shells with a 2-nm gap increased to

50° C in 6 min, whereas the temperature of the rod-in-shells with a 6.5-nm gap increased to only 29° C. To reflect this phototransduction efficiency in PTT, the zone area of cell death was extended beyond the laser illumination region in LLC/LL2 lung cancer cells treated with 2-nm gap structures by administering irradiation using a 1064-nm laser with a 3-W/cm^2 power density. Comparatively, the PTT zone area of cell destruction was not apparent when rod-in-shell with 6.5-nm gap was used to treat LLC/LL2 tumor cells. LLC/LL2 tumor-bearing mice were intratumorally injected with the rod-in-shells and irradiated using a 1064-nm laser with a 3-W/cm^2 power density. The tumor change was monitored for 9 days. The mice group injected with 2-nm-gap rod-in-shells demonstrated complete control over tumor growth, whereas the group injected with the 6.5-nm-gap rod-in-shells displayed no control over tumor growth.

A hybrid with Au NPs assembled on silicon nanowires (SiNWs) was developed for evaluating NIR photothermal properties.[50] The SiNWs were prepared by etching a silicon wafer. Subsequently, the SiNW@AuNPs were synthesized by performing the *in situ* reduction of Au$^+$ on the SiNW. The absorbance spectra of the SiNW@AuNPs showed NIR absorbance from 700 to 1000 nm. The SiNW@AuNPs displayed approximately 40° C increase in temperature, whereas the SiNWs or the AuNPs alone demonstrated only a 3° C or 7° C increase in temperature, respectively when irradiated with an 808-nm diode laser for 3 min at a power density of 2 W/cm^2. For the *in vitro* applications, SiNW@AuNPs was PEGylated with PEG-SH through gold thiol bonding, denoted as SiNW@AuNPs-PEG. KB cells were incubated with SiNW@AuNPs-PEGs, followed by NIR irradiation using an 808-nm laser with a 2-W/cm^2 power density. Among the various SiNW@AuNPs-PEGs concentrations and durations of laser irradiation, administering 150 ppm of SiNW@AuNPs-PEGs combined with 3 min of laser irradiation completely destroyed the cells. In addition to the KB cells, the effects of PTT on A549 and HeLa cells were studied, the results of which exhibited a similar trend.

D.2. Drug delivery

For the combination of chemotherapy with PTT, DOX-encapsulated polymer nanoparticles (DOX-PNPs) were formed with Au nanoparticles decorated on the surface.[51] The DOX-PNPs were formed by performing oil-in-water emulsification on DOX and dithiolated dimethylaminoethyl methacrylate polymers (DDMP). The as-prepared Au nanoparticles were bound to the surface of the DOX-PNPs through gold thiol binding to yield DOX-PNP@Au. DOX-PNP@Au mimicked the Au shell containing a dielectric core and exhibited NIR absorbance. The DOX-PNP@Au was then PEGylated with SH-PEG-COOH through gold thiol bonding to form DOX-PNP@Au-PEG. The remaining –COOH groups in the PEG of the DOX-PNP@Au-PEG were tethered with antiherceptin antibodies using amide binding for targeting Herceptin-positive SK BR3 human breast cancer cells. The resulting antiHER-DOX-PNP@Au-PEGs with an unorganized Au shell-like structure showed an absorbance maximum at 795 nm. The antiHER-DOX-PNP@Au-PEGs exhibited a 15.3° C temperature increase when subjected to irradiation using

an 810-nm laser with a 5 W/cm^2 power density for 5 min. In addition to thermal sensitivity, the antiHER-DOX-PNP@Au-PEGs were also pH sensitive because the amines in the polymer DDMP were protonated at a low pH, which caused them to expand in size and release the drug. The antiHER-DOX-PNP@Au-PEGs induced a 30% DOX release at pH 5.5 in 6 h that increased to 50% when NIR irradiation was performed. Comparing the combined therapeutic effect (PTT and chemotherapy) of the antiHER-DOX-PNP@Au-PEGs with the PTT effect of antiHER-PNP@Au-PEGs in SK BR 3 cells, revealed that 14.5% and 31% cell viability was exhibited, respectively. Herceptin-negative MCF 7 human breast cancer cells were used to demonstrate the targeting effect of antiHER-DOX-PNP@Au-PEGs. By comparison, the SK BR 3 cells demonstrated a 5.4-fold increase in the antiHER-DOX-PNP@Au-PEG uptake compared with the MCF 7 cell uptake. The MCF 7 cells treated with antiHER-DOX-PNP@Au-PEGs and antiHER-PNP@Au-PEGs, with or without irradiation, did not exhibit a significant difference, which was attributed to the lack of targeting. In another study, the aforementioned unorganized shell formed using Au nanoparticles tethered to thiolated polymer nanoparticles was modified to create a Au semishell grown on DOX-loaded PLGA nanoparticles, which was demonstrated to exhibit NIR absorbance.[52] DOX-loaded PLGA nanoparticles were prepared using poly (vinyl alcohol) as the stabilizer to form DOX@PLGA. DOX@PLGA was spin casted onto the silicon surface, and then a 15-nm-thick layer of gold was deposited on the remaining exposed surface to form DOX@PLGA@sGS (sGS: semigold shell). The DOX@PLGA@sGSs exhibited absorbance at approximately 800 nm. The DOX@PLGA@sGSs induced a slow DOX release, in which 68% of the DOX was released, but the speed was increased by applying 808-nm diode laser irradiation with a power density of 1.5 W/cm^2. In the *in vitro* combined PTT and chemotherapy studies, the cell viability of HeLa cells treated with DOX@PLGA@sGSs followed by irradiation using an 808-nm laser with a 0.7 W/cm^2 power density had reduced to approximately less than 20%. However, in the independent PTT (PLGA@sGS) and chemotherapy (DOX@PLGA@sGS) studies, the HeLa cells treated with materials exhibited 65% and 70 % cell viability, respectively.

D.3. Photodynamic therapy

A pseudonanoshell was prepared by Lin *et al.*[53] by assembling the Au nanoparticles using the amphiphilic block polymer to form gold vesicles (GVs), which were used as carriers of photodynamic sensitizing dye. In their study, the citrate reduction of gold ions was used to prepare the Au NPs. The Au NPs were then functionalized using the thiol-terminated amphiphilic block polymer, polyethylene oxide-b-polystyrene (Au NPs-PEG-PS). The Au NPs-PEG-PS was dried and rehydrated to form hollow vesicles called gold vesicles. The absorbance spectra of the GVs showed a broad absorbance range from 650 to 800 nm, which was attributed to the enhanced plasmonic coupling caused by the adjacent Au NPs. This NIR absorbance was used in studies on PTT alone or PTT combined with PDT, in which the GVs were loaded with Ce6 photodynamic photosensitizer. The excitation wavelength of Ce6 was 671 nm, which coincided with the wide absorbance range of the GVs, to use a

single laser for conducting both PTT and PDT. GV-Ce6 irradiated with the 671-nm laser with a 2 W/cm^2 power density increased the temperature to 42° C in 5 min. The GV-Ce6 was endocytosized, which caused a greater uptake of Ce6 through the GV-Ce6 than the uptake of free Ce6 through passive diffusion. This enhanced uptake efficiency of Ce6 through the GV-Ce6 increased the cytotoxicity when 2 W/cm^2 of laser-powered irradiation was applied compared with that produced by the free Ce6 treatment with laser irradiation. In the *in vitro* combination (PTT + PDT) therapy, MDA-MB-435 human breast cancer cells incubated with GV-Ce6 were irradiated with a 671 nm laser with a 2 W/cm^2 power density. The combination therapy caused an approximately 90% reduction in cell viability, whereas in the control cells incubated with GV-Ce6, without laser irradiation, an approximately 90% cell viability was observed. In the *in vivo* combination (PTT + PDT) therapy, the mice bearing MDA-MB-435 tumors were injected with the GV-Ce6, followed by irradiation using a 671 nm laser, and the tumor volume was monitored for 2 weeks. The tumor size was observed to be completely controlled. Regarding the independent PTT (mice injected with GVs) and PDT (mice injected with Ce6) performance, the mice bearing MDA-MB-435 tumors were injected with GVs and Ce6 separately, followed by 671 nm laser irradiation with a 2 W/cm^2 power density. A reduction in tumor volume was subsequently observed, compared with that of the control, which did not undergo NIR irradiation. In addition to PTT and PDT, the applications of the fluorescence produced by GV-Ce6 were demonstrated in the uptake analysis both *in vitro* and *in vivo*, as shown in Fig. 13.
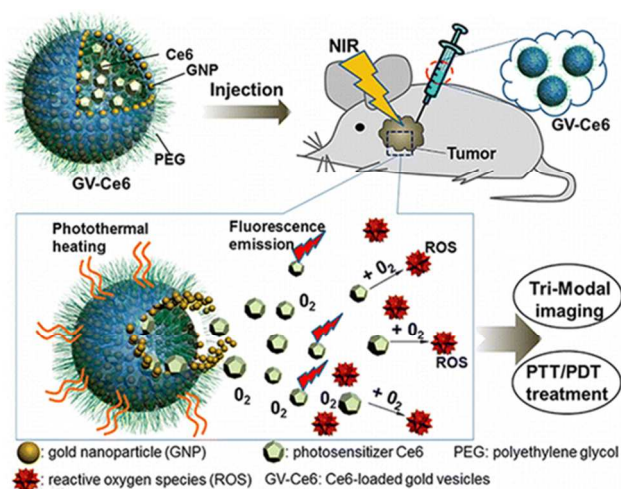

Fig. 13. The schematic illustration of GV-Ce6 injected into the mice bearing xenograft tumors, showing the trimodal function comprising PTT, PDT, and imaging. (Reprinted with permission from ref. 53. Copyright *ACS Nano*, 2013.)

E. Graphene oxide

Graphene oxide (GO) is a two-dimensional material obtained from the oxidative exfoliation of graphite. It has been synthesized using the widely accepted Hummer method,[54] which involves the use of a strong oxidizing agent such as KMnO$_4$ with the acid H$_2$SO$_4$. The oxidation of the graphite to GO is conducted by the active species dimanganese heptoxide, formed by combining

KMnO$_4$ with H$_2$SO$_4$. This method is used to produce functional groups on the surface of GO that facilitate functionalization. By contrast, pristine graphene synthesized using chemical vapor deposition (CVD) does not comprise functional groups that can facilitate adequate dispersion. Graphene, ideally of single-atom thickness, has a radically large specific surface area of up to 2600 m^2/gm.[55] Graphene and GO have become attractive materials because they have a large surface area; are light weight; exhibit high strength and electrical conductivity; and are capable of optical property-expressing plasmon, fluorescence, and nonlinear emission. In the pursuit of nanomaterials expressing optical properties, studies have typically involved the confinement of metals and metal oxides such as gold, silver, and copper oxide. However, the optical property expressed by carbon nanomaterials broadens the range of possible nanomaterials that can be used beyond the category of metal nanoparticles. The optical properties of graphene, for example, became a topic of interest when the existence of plasmon in this allotrope of carbon was determined.[56]

E.1. Photothermal therapy

The absorbance of GO extends from the UV wavelength to the NIR region. Thus, the absorbance at 808 nm was used for expressing the photothermal property. This photothermal property of GO was applied in the *in vivo* photothermal ablation of tumors.[57] However, this readily induced GO dispersion was not easily achieved in bio-applications because of the high degree of binding that occurs between GO and proteins and with other salts in serum, which leads to aggregation. Therefore, the carboxyl groups in the as-prepared GO were functionalized covalently using amine-terminated PEG (PEG-GO) to increase the level of dispersion. By performing irradiation using an 808 nm diode laser with a 2 W/cm^2 power density, PEG-GO increased the temperature to approximately 60° C within 3 min. To monitor the *in vivo* uptake of PEG-GO, cyanine IR fluorescent dye (Cy7) was covalently conjugated to the amine in the PEG-GO to form Cy7-PEG-GO. The Cy7-PEG-GOs were injected into the mice bearing three xenografts: 4T1 (murine breast cancer cells), KB, and U87MG. All of the tumor xenografts in the mice injected with Cy7-PEG-GOs passively accumulated in the tumors over 24 h. Based on this uptake result for the three cell lines, only 4T1 cells were used in PTT. In PTT, the mice bearing 4T1 cells were intravenously injected with PEG-GOs at a dosage of 20 gm/kg and allowed to accumulate in the tumor for 24 h. After 24 h of PEG-GOs accumulation in the tumors, the tumors were irradiated using an 808-nm laser with a power density of 2 W/cm^2, which caused the tumor temperature to increase to approximately 50° C. By contrast, the mice that were not injected with PEG-GOs exhibited only an approximately 2° C increase in tumor temperature. Regarding the therapeutic efficiency demonstrated in the mice injected with PEG-GOs and subjected to irradiation, the tumors disappeared in 1 day and the group of mice survived for 40 days. However, the mice that were injected with PEG-GOs and were not subjected to laser irradiation showed an increase in tumor volume and they did not survive for more than 16 days. Furthermore, the chemical reduction of graphene oxide (rGO) was determined to improve photothermal efficiency compared to GO.[58] In the aforementioned study, GO was

PEGylated through amide binding using amine-terminated 6-arm branched PEG (PEG-GO). The PEG-GO was reduced chemically using hydrazine to yield PEG-rGO, which still caused a certain degree of aggregation despite PEG conjugation. To restore the dispersion, the PEG-rGO was PEGylated again using sonication with a polymer (two methoxy-terminated PEG and one C17 chain attached to the poly maleic anhydride) to form 2PEG-rGO. The hydrophobic component interacted with the graphene plane and the hydrophilic component facilitated the restoration of dispersion. Compared to the unreduced PEG-GO, the NIR absorption of 2PEG-rGO was 6 times greater because the hexagonal pristine structure was partially restored. The 2PEG-rGO also exhibited a substantial increase in temperature when compared with that of the PEG-GO when irradiation was performed using an 808 nm laser with a 0.6 W/cm^2 power density. The 2PEG-rGOs were conjugated with the RGD peptides (Arg-Gly-Asp) through the amine end of the PEG, denoted as RGDrGOs. The RGD peptides on the RGDrGOs facilitate the targeting of the $\alpha_v\beta_3$ integrin receptors overexpressing in U87MG glioblastoma cells. Thus, after incubation with the RGDrGOs, the U87MG cells were irradiated using an NIR diode laser with a power density of 15 W/cm^2 for 8 min. The temperature of the cells increased to 52° C in 1 min, which led to the complete destruction of the cells. To enhance the photothermal effect further, the plasmon-rich Au NPs were combined with GO.[59] In this context, Au nanoshells and Au NRs were coated with GOs electrostatically followed by chemical reduction to yield rGONSs and rGONRs (together referred to as rGOAu NPs), respectively. The hydrazine-reduced GO was coated on the plasmonic nanoparticles and fastened them, as shown in Fig. 14. The rGOAu NPs with an optical density of 5 units were coated onto a thin-layer chromatography (TLC) plate for the dry-state photothermal property measurements. Upon exposure to an 808-nm diode laser with a power density of 3 W/cm^2 for 30 s, the temperature increased by 27° C and 57° C in the GONSs and rGONSs, respectively; similarly, the temperature increased by 32° C and 67° C in the GONRs and rGONRs, respectively. This indicated that the chemical reduction of GO played an effective role in enhancing photothermal conversion efficiency. The therapeutic effect of the photothermal rGOAu NPs was further demonstrated on human umbilical vein endothelial cells. The cells treated with rGONSs and rGONRs for 24 h, followed by 1 min of irradiation performed using an 808 nm laser with a 3 W/cm^2 power density, reduced the cell viabilities to 23% and 33%, respectively, whereas in the unreduced GO-coated NSs and NRs, the cell viabilities were 43% and 57%, respectively.
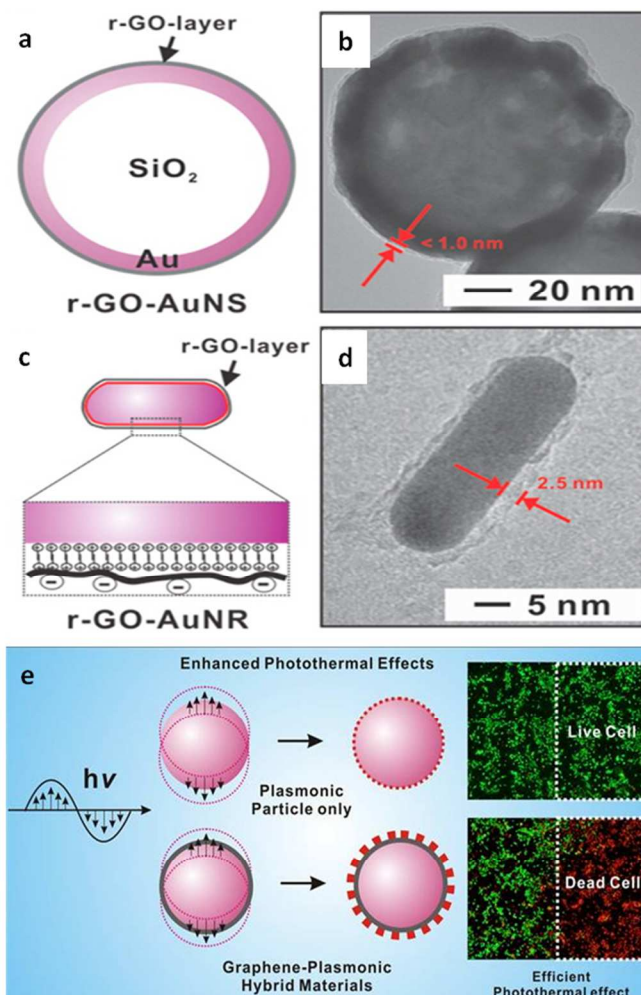

Fig. 14. (a) and (c) show the schematic illustrations of the rGO coated on an NS and NR, respectively; (b) and (d) show the corresponding TEM of (a) and (c), respectively. The red arrows indicate the thickness of the rGO coating on the nanoparticles, accompanied by the corresponding values. The right panel of (e) shows the efficiency of the rGO-coated plasmonic particles in photothermal therapy compared with that of the conventional plasmonic nanoparticles. (Reprinted with permission from ref. 59. Copyright *Nano Lett.*, 2013)

Following the aforementioned photothermal study and the enhancement achieved using the combination of Au NPs, subsequent attempts were made to conjugate other functional nanoparticles to demonstrate multiple functions. Hu *et al.*,[60] attempted to combine quantum dots (QDs) with rGO. However, placing more QDs onto a single rGO sheet may cause fluorescence quenching. Therefore, to avoid fluorescence quenching, an isolation distance between the QDs was maintained by applying an organic coating over the QDs. The organic coating was formed using tri-n-octylphosphine oxide (TOPO), followed by mercaptoundacanoic acid coating for the partial replacement of TOPO. This organic coating produced a 1.7-nm gap between the nanoparticles that prevented the quenching of fluorescence. In addition, the rGO was coated with poly (L-lysine)

using hydrophobic adsorption. The loading of the organic molecule-coated QDs onto the poly (L-lysine)-coated rGO was achieved using electrostatic adsorption. The resulting composites were prepared by using two sizes of rGO: approximately 38 nm and 260 nm. The composite containing the 38-mm GO sheet was designated as the ultra small composite, denoted as QDUSrGO, and the other containing the 260-nm rGO sheet was designated as the small composite, denoted as QDSrGO. Although the composites exhibited unquenched fluorescence, a shielding effect of the GO accounted to 15% in the QDUSrGO and 50% in the QDSrGO. The composites were further conjugated with the folic acid using the amine end of the lysine for the imaging and photothermal studies. The folate receptor overexpressing MCF 7 human breast cancer cells incubated with the QDUSrGOs demonstrated a significant uptake both in the flow cytometry and imaging analysis. In the demonstration of photothermal therapeutic properties, MCF cells incubated with QDUSrGOs and QDSrGOs were irradiated using an 808 nm diode laser with a 2 W/cm^2 power density for 9 min. The QDUSrGOs and QDSrGOs showed the cell viabilities decreased to approximately 5% and 30%, respectively. However, it was found that irradiation time-dependent fluorescence was compromised in the composites. This was considered to be a result of thermal damage to the organic coating on the QDs, which caused the QDs to become susceptible to oxidation. Similarly, to achieve multifunctionality using the GO platform, GO combined with fluorine (FGO) was investigated for used in MRI and photothermal applications.[61] The fluorinated graphite was exfoliated in the same manner used in GO synthesis to obtain FGO. The MRI studies have reported that T_2 contrast was observed in FGOs, whereas no such contrast was observed in GOs. FGOs were biocompatible even at a concentration greater than 500 ppm. FGOs also could increase the tissue temperature to as high as 60° C within 1 min under 800 nm laser irradiation at a power density of 1.3 W/cm^2, demonstrating that the photothermal property was not compromised during fluorination. The glioma cancer cells (GI 1) containing FGOs, when irradiated with the NIR laser for 1 min and stained for determining necrosis and apoptosis, exhibited increased staining intensity compared with that of the cells untreated with FGOs. Another example to achieve multifunctionality, the triple function (MRI and X-ray imaging combined with enhanced PTT) was demonstrated by loading iron oxide nanoparticles (IONPs) and Au NPs onto GO.[62] The GOs synthesized using the Hummer method were loaded with the IONPs by using the hydrothermal process. Subsequently, polyethyleneimine coating that allowed the negatively charged Au seeds to adsorb electrostatically on the GO sheet was applied. The Au seeds were grown using a growth solution to form GO-IONP-Au composites. The GO-IONP-Au composites were then functionalized using the lipoic acid modified PEG to achieve dispersion, denoted as GO-IONP-Au-PEG. By varying the Au concentration, different ratios of GO:IONP:Au were obtained. The composite with a ratio of 1:2.11:1.57 exhibited enhanced NIR absorbance compared with that of the composites with a lower Au ratio. Au also helped to enhance the contrast in X-ray imaging, which was demonstrated using a digital X-ray imaging accessory. The IONP in the GO-IONP-Au-PEG composites contributed to the T_2-weighted image, which was confirmed by the concentration-dependent darkness shown in the 3T MR scanner. For evaluating

PTT performance, 4T1 cells treated with GO-IONP-Au-PEGs were exposed to an 808 nm NIR diode laser with a power density of 2 W/cm^2 for 5 min, which resulted in complete cell death. In the *in vivo* studies, BALB/c mice with the 4T1 tumor were injected with 40 μL of 50 ppm GO-IONP-Au-PEGs intratumorally and irradiated using an 808 nm NIR laser with a 0.75 W/cm^2 power density for 5 min, which caused a reduction in tumor size, whereas in other treatments that did not involve a laser, a continual increase in tumor size occurred. By using an IR camera, the temperature in the tumor exposed to laser irradiation was observed to increase to 55° C.

E.2. Drug delivery

In initial studies on GO-assisted chemotherapy, GO was limited to serving as the drug delivery vehicle, in which the drug was slowly released at the cell site spontaneously. In the subsequent development of GO-assisted chemotherapy, the photothermal properties of GO were considered for several applications: (1) combined chemo- and photothermal therapy; (2) drug release caused by endosome disruption; and (3) drug release caused by the collapse of the thermosensitive drug reservoir. In this subsection, the details in design and associated therapy are discussed.

The hexagonal arrangement of carbon in GO favors the noncovalent loading of anticancer drug cargo using π-π staking. The GO exhibits a radical increase in drug loading of approximately 200% by weight, and this is the first drug carrier to achieve over 100% loading consistently. In addition, the GO was able to unload the cargo under highly acidic and basic conditions because of the compromise in the hydrogen bonds between the –COOH and –OH groups of GO and the –OH and –NH$_2$ groups of DOX.[63,64] The unloading of DOX from the GO in an acidic environment is caused by the formation of NH$_3^+$ from the NH$_2$ groups of DOX. NH$_3^+$ does not contribute hydrogen bonds; consequently, the loaded DOX is delivered under acidic conditions from the GO. This phenomenon is desirable because the endosome mimics the acidic condition. Thus, initial studies used this native acidic tumor environment to deliver the drug spontaneously as desired to kill cancer cells. In this context of spontaneous release, Dai *et al.* loaded the hydrophobic drug SN38 (an analogue of anticancer drug camptothecin) on the PEGylated GO using π-π staking.[65] This complex (GO-SN38) was noncovalently stable, releasing only 30% of the drug during 3 days of incubation. Clinically, the treatment with SN38 is administered as a CPT-11 (CPT-11: camptothecin) prodrug, which is hydrophilic and must metabolize to SN38 to achieve cytotoxic activity. However, this metabolism process often fails and, consequently, CPT-11 exhibits low therapeutic efficiency. In HCT-116 human colon cancer cells, the IC50 value of CPT-11 was 10 μM, whereas the IC50 value of GO-SN38 was 6 nM. The GO-SN38 was more efficient by approximately 1000 fold compared with that of the CPT-11.

Following the studies on the aforementioned spontaneous release, the photothermal characteristic of GO was subsequently introduced for determining the combination of PTT and chemotherapy with imaging.[66] In this demonstration, FeCo alloy nanoparticles with a graphitic carbon shell (FeCo/GC) were prepared using the CVD method. The FeCo/GC was coated with

phospholipid-branched polyethylene glycon (PL-PEG-FeCo/GC). The PL-PEG-FeCo/GC was able to carry up to 2000 DOX molecules using π-π staking and hydrophobic force. Under acidic conditions, the protonation of the amine in DOX led to drug release. The amount of intracellular drug delivery was further increased by the photothermal property of GO. To demonstrate this phenomenon, MCF 7 cells were treated with the DOX-loaded PL-PEG-FeCo/GCs, which exhibited 35% and 75% cell viability with and without NIR laser irradiation, respectively. The low cell viability exhibited during the irradiated treatment was caused by the enhancement of drug toxicity under hyperthermic conditions and increased uptake. The increase in uptake when laser irradiation was applied was confirmed using MRI imaging, which showed increased brightness. The synergistic effect of PTT combined with chemotherapy was also observed by loading DOX onto the PEGylated GO (GO-DOX) using π-π stacking.[67] The GO-DOX demonstrated 143% drug loading efficiency. EMT6 murine mammary tumor cells were incubated with the GO-DOXs, followed by the irradiation of the cells using an 808 nm CW laser with a power density of 2 W/cm^2 for 2 min. The inhibition rate of the cells treated with GO-DOXs was 82.1%, whereas for the free DOX (without laser irradiation) and GO (with laser irradiation), the inhibition rates were 57% and 45.4%, respectively. The tail vein injection of GO-DOXs followed by 5 min of exposure to an 808 nm laser with 2 W/cm^2 enabled complete control over tumor growth, whereas in the other groups that received chemotherapy or PTT alone, an initial reduction was observed, but the tumor began to grow gradually. Wang *et al*. used mesoporous silica-coated GO (GO@MS) to administer chemotherapy and PTT.[68] In this study, the GO was coated with mesoporous silica to form a sandwich structure. The GO@MS was then coated with PEG to achieve solubility and IL31 peptides (sequence: VDKLL LHLKK LFREG QFNRN FESII ICRDR TC)[69] for glioma cell targeting. This mesoporous coating structure, GO@MS, had a 1252 m^2/g specific surface area and exhibited 125% DOX drug loading, and was denoted as DOX-GO@MS. When irradiation was performed using an 808 nm laser at a power density of 6 W/cm^2 on 50 ppm of GO@MSs, the temperature increased to greater than 50° C in 2 min. The DOX-GO@MSs spontaneously released the drug in the acidic solution. In addition, laser irradiation affected the amount of the drug released, which increased by 3 times. The increase in uptake caused by the targeting peptide-coated DOX-GO@MSs was revealed using a fluorescence microscope. Regarding cytotoxicity, the combination index of the therapeutic combination involving chemotherapy and PTT of the DOX-GO@MSs confirmed the synergistic effect.

Recently, the process of photothermally disrupting endosomes to release drugs was demonstrated by applying GO-assisted photothermal therapy.[70] GO was conjugated with PEI through amide binding, followed by reduction to form PEI-rGO. This PEI-rGO was PEGylated using a coupling reaction to yield PEG-PEI-rGO. The composite PEG-PEI-rGO was loaded with DOX to form DOX-PEG-PEI-rGO and the loading efficiency was approximately 100% (w/w), which was 10 times more than the loading efficiency of PEG-PEI-GO (unreduced form). Subsequently, photothermal efficiency was monitored using an 808 nm diode laser with a power density of 6 W/cm^2, which showed that the temperature

increased to 80° C in 350 s. The endosomal disruption and drug release were demonstrated using a fluorescence microscope. The image showed that the PEG-PEI-rGOs localized in the endosomes, and only after NIR irradiation was performed, giving the fluorescence dyes loaded in the PEG-PEI-rGOs to distribute throughout the cytoplasm. However in the *in vitro* cytotoxicity studies, the DOX-PEG-PEI-rGOs subjected to NIR irradiation exhibited less cell death in PC3 human prostate cancer cells compared with that caused by using the free drug. The low therapeutic efficiency of DOX-PEG-PEI-rGOs compared with that of free DOX was accepted because of the delay in the release of DOX and the endocytosis-mediated cytosolic release of DOX. The release of the drug from the nanocarrier in the endosomes to the cytoplasm was partially controlled by the photothermal disruption of the endosomes. In addition, the free drug reaches the cytoplasm directly through passive diffusion.[71] Despite the low efficiency of DOX-PEG-PEI-rGOs compared with that of free DOX, it was considered crucial because the drug could be released from endosomal disruption.

A GO-based nanogel was developed to expand the scope of GO in controlled drug release.[72] To prepare the nanogel, chitosan was conjugated with chemically reduced GO through amide binding. In addition, acrylic acid was attached to the chitosan-GO through additional amide binding. This acrylated chitosan-GO monomer was then polymerized using the cross linker diacrylate PEG to form nanogels. The nanogels exposed to an 808 nm laser with a power density of 900 mW/cm^2 increased the temperature by 24.5° C in 5.5 min. This heating dehydrated the gel and the size of the hydrophilic chain subsequently decreased to 220 nm from 500 nm. Thus, this property enabled drug delivery. DOX was loaded through noncovalent binding in the gel. The incubation solution of 300 μg/mL DOX exhibited approximately 50% (w/w) DOX loading in nanogel (DOXNG). The DOXNG demonstrated an 18% DOX release when subjected to NIR irradiation, whereas the DOX release without NIR exposure was only 5%. The *in vitro* cytotoxicity against the cancer cells was demonstrated using TRAMP-C1 mouse prostate cancer cells. The IC50 value for the free drug was 2 μM, whereas using 900 mW/cm^2 of power to perform irradiation with an 808 nm NIR laser led to an IC50 value of 1 μM for the DOXNGs. This enhancement in toxicity was caused by the increased uptake of the DOXNGs.

E.3. Photodynamic therapy

GO could serve as an effective carrier of photodynamic sensitizer dye through noncovalent interaction. In addition to being the carrier in PDT, the property of the GO as a transducer was used for administering PTT with PDT. The potential of the GO to load efficiently was also considered for loading chemotherapeutic drugs in addition to photodynamic sensitizer dye in the combined photodynamic and chemotherapy studies. All these combinations are discussed in this subsection.

GO was used as the carrier of a hydrophobic photodynamic sensitizer, hypocrellin A, through hydrophobic adsorption and denoted as GOHA.[73] The amount of singlet oxygen

produced from the GOHA was less than the free hypocrellin A produced when quantified immediately after dispersing in the solvent. After a long incubation time, unstable free hypocrellin A dispersion was severely reduced in the singlet oxygen formation, whereas GOHA retained the same efficiency during singlet oxygen production because it achieved stable dispersion. Therefore, delivering hypocrellin A using the GO carrier is crucial. Furthermore, the ability of the hypocrellin A to target mitochondria helped the GOHA localize in the mitochondrial region. The HeLa human cervical cancer cells treated with GOHAs followed by light irradiation (570 nm) exhibited nuclear shrinking, chromatin condensation, and fragmentation, whereas such complexation was not noticed in the cells treated with the GOHAs without laser exposure, or those treated with NIR irradiation alone. Similarly, Huang *et al*. demonstrated that GO conjugates with folic acid (FA) to serve as the targeted carrier of the photodynamic photosensitizer.[74] The GO was conjugated to FA through the EDC/NHS reaction. After FA conjugation, photodynamic photosensitizer dye chlorin e6 (Ce6) was loaded to form FA-GO-Ce6. The FA-GO-Ce6s incubated with MGC803 human stomach cancer cells demonstrated targeting uptake, which was confirmed using the fluorescence microscope image. The cells treated with FA-GO-Ce6s, and then with 632.8 nm He-Ne laser irradiation using a 30 mW/cm^2 power density for 10 min exhibited a 90% reduction in cell viability, whereas the cells that were not treated with laser irradiation displayed more than 80% cell viability.

In contrast to the aforementioned studies, in which the GO served as the carrier only, few attempts were made to enhance the photothermal properties of GO by combining it with PDT. The GO was functionalized with the pluronic block polymer to achieve biological stability.[75] The functionalization with the pluronic block polymer is simple because the poly (propylene oxide) block polymer readily causes hydrophobic interaction with GO to occur. Subsequently, methylene blue (MB) loading performed using electrostatic attraction was characterized by a maximum of 22% loading on the GO, denoted as GOMB. The MB displays singlet oxygen production upon irradiation with a 655 nm diode laser. Applying irradiation using an 808 nm CW laser with a power density of 2 W/cm^2 on 10 ppm GOMBs caused a 17° C increase in temperature within 3 min. The HeLa cells treated with GOMBs followed by laser irradiation, for the groups that underwent PTT, an 808 nm laser was used for irradiation for 3 min; for the group that underwent PDT, a 655 nm laser was used for 3 min; and for the combined therapy, a 655 nm laser was used, followed by an 808 nm laser. The PTT effect resulted in 40% cell viability, the PDT group exhibited 50% cell viability, and the combined therapy group showed 25% cell viability. GOMBs were also tested for the *in vivo* therapy using mice bearing HeLa tumors. The GOMBs were injected through the tail vein. At 24 h postinjection, the laser treatment was administered by using the 655 nm laser and 808 nm laser for 3 min each at the tumor site. The 15 days observation of tumor volume revealed no tumor increase in the group that received both treatments (PDT and PTT), whereas the mice that received PDT or PTT alone demonstrated initial inhibition, but then the tumor size increased steadily. Recently, by using combined PTT and PDT, Tian *et al*.

produced a mild photothermal effect to enhance the uptake followed by PDT.[76] GO synthesized using the Hummer method was functionalized with the amine-terminated 6-arm PEG using covalent conjugation. Subsequently, photosensitizer Ce6 was loaded using electrostatic adsorption to form GOCe6, which exhibited 15% Ce6 loading. The KB carcinoma cells treated with GOCe6 were irradiated for 10 min using a 660 nm diode laser with 0.1 W/cm^2. The cell viability reduced more than that of the free Ce6. They speculated that this may have been caused by the enhancement in the uptake of Ce6 in the GOCe6 compared with that of free Ce6. A fluorescence image was taken, which showed that a higher fluorescence was produced by GOCe6 compared with that of the cells treated with free Ce6. In addition, they predicted that preheating may further enhance uptake. In this context, a separate uptake analysis was performed using an 808 nm laser with a power density of 0.3 W/cm^2 to conduct preirradiation for 20 min. Because the photosensitizer excitation occurred at 660 nm, preheating did not generate singlet oxygen. When preheating was conducted, the uptake increased further. Thus, the GO functioned as the carrier and preheat supplier in enhancing uptake. KB cells that were not preirradiated but treated with GOCe6 followed by 660 nm laser irradiation exhibited approximately 25% cell viability. Conversely, the KB cells incubated with GOCe6 and subjected to 808 nm laser exposure followed by 660 nm laser irradiation had a cell viability of approximately 5%. This verifies the effect of preheating on the uptake of GOCe6.

In contrast to the aforementioned combination of PTT and PDT, combined PDT and chemotherapy was investigated in another study using GO.[77] In this study, GO conjugated with PEG through covalent binding with the amine end of the PEG. The PEG-GO was loaded with Ce6 (PEG-GO-Ce6) or DOX (PEG-GO-DOX) using electrostatic attraction and demonstrated 52% and 67% loading, respectively. SCC7 cells treated with PEG-GO-Ce6 using 690 nm laser irradiation exhibited approximately 60% cell viability in PDT; the cells treated with PEG-GO-DOX using 660 nm LED light irradiation showed approximately 90% cell viability during chemotherapy. By contrast, the synergistic effect of PEG-GO-Ce6/DOX (PEG-GO loaded with both Ce6 and DOX) combined with 660 nm laser exposure caused cell viability to reduce to approximately 20%. PEG-GO-Ce6/DOX used in the *in vivo* experiments and monitored for 28 days caused a 73% reduction in tumor volume.

As compared to the Au NRs, the mass extinction coefficient of rGO at 808 nm is 2 times more.[58] Further, the dramatic increase in the specific surface area[55] in this ultra low density material aids in the 200% drug loading efficiency which is significantly higher than the any of the nanocarriers.[63] The native hexagonal ring in the graphene aids in the spontaneous loading of the drug through π-π staking without the requirement for the modification or crosslinkers by non-covalent interaction. As mentioned in section E2, the GO is able to unload the cargo under highly acidic and basic conditions. This behaviour matches well with the acidic cancer tissue environment for the site specific delivery. Hence, the increased mass extinction coefficient, exceptionally

increased drug loading and the ability to unload in the acidic condition make GO a promising material for PTT and chemotherapy. However, one should keep in mind that its polydispesity challenges the uniformity and quantification at single particle level.

F. Upconversion nanoparticles

UCNPs are lanthanide-doped nanomaterials that can emit upconverted energy using the excitation of low-energy NIR, which is typically at 980 nm. The upconverted wavelength of UCNPs matches favorably with the absorption region of various photosensitizer (PS) molecules; therefore, UCNP-mediated NIR cancer therapeutics are mainly focused on PDT. However, the relationship between drug delivery and PTT with UCNPs has been reported in a few studies. Therefore, in this section, for the convenience of the readers we have categorized the studies of PDT using subheadings based on PS loading interaction. Because reviews on the synthesis of UCNPs already exist,[78,79] we directly focused on the applications of UCNPs in cancer therapy.

F1. Adsorption/encapsulation

The porphyrin and phthalocyanine types of PS molecules are widely employed as PDT agents, which comprise a large aromatic cyclic skeleton and exhibit intense visible absorption. The simple physical adsorption of PS and UCNPs is derived from the hydrophobic nature of PS and UCNPs that are typically coated with oleic acid. This type of physical adsorption causes extremely close contact between PS and UCNPs, which improves the fluorescence resonance energy transfer (FRET) between the UCNPs and PS. In this category, hydrophobic UCNPs are converted into hydrophilic UCNPs by coating them with appropriate molecules. This leads to the combination of inner hydrophobic and outer hydrophilic layers.

The physical adsorption caused by hydrophobic interaction between PS and UCNPs was demonstrated using PEGylated UCNPs [$NaYF_4$:Yb/Er (Y:Yb:Er = 78%:20%:2%)], followed by the treatment of lipophilic Ce6 (PS) in PBS buffer.[80] Because of the presence of oleic acid (OA) on the surface of UCNPs, a hydrophobic-hydrophobic interaction occurred between the PS and UCNPs. In addition, because the OA was directly linked on the surface of the UCNPs, the incoming PS molecules were in close contact with them as PS-UCNP composites, which facilitated the transfer of energy using the FRET mechanism upon excitation. By using this strategy of simple physical adsorption, the results indicated that in-depth *in vivo* PDT was more favorable than the traditional visible-light-excited PDT. For this demonstration, 4T1 cells treated with PS-UCNPs were blocked with pork tissue of varying thicknesses when irradiated with a 980 nm diode laser using a 0.5 W/cm² power density. The 3- and 8-mm-thick pork blocked the irradiation, resulting in a 5% and 50% PDT reduction, respectively, whereas in the free Ce6-treated cells irradiated with a 660 nm laser (Ce6 absorbs 660 nm wavelengths), the 3-mm-thick tissue block reduced PDT by 80% and PDT was indeterminate when an 8-mm-thick tissue block occurred. For *in vivo* PDT, the mice bearing 4T1 tumor cells were intratumorally injected with PS-UCNPs, covered with 8-mm-thick pork tissue, subjected to irradiation using a 980 nm

laser with a 0.5 W/cm² power density. The results indicated a substantial reduction in tumor growth. In addition, when free Ce6 was administered to the tumor, followed by 660 nm irradiation using a similar tissue block, no reduction in tumor growth was observed. A similar strategy of physical adsorption of PS for PDT was proposed in combination with chemotherapy using DOX.[81] In this study, Mn was doped in UCNPs (Mn-doped $NaYF_4$: Yb/Er). The strong single-band emission of Mn-modified UCNPs appears in the 650–670 nm region, which is being widely used to excite various PS molecules, such as Ce6, zinc phthalocyanine (ZnPc), and MB molecules, for PDT. Hydrophilic α-cyclodextrin (α-CD) was used to convert hydrophobic UCNPs to water-soluble UCNPs using a self-assembly approach, in which an interaction occurred between the hydrophobic cavity of the host molecule, α-CD, and the guest OA, as shown in Fig. 15A. The Ce6 was loaded onto α-CD-coated UCNPs using simple stirring *via* hydrophobic interaction. In addition, by combining hydrophobic DOX with Ce6, they are able to show the improved efficiency of the combinational therapeutic system (DOX-Ce6-UCNPs). The release of a chemotherapy agent was based on the change in pH inside the microenvironment of the cancer cells. The acidic pH protonates DOX and renders DOX hydrophilic, which subsequently cannot remain in the hydrophobic reservoir. This was proved by incubating DOX-Ce6-UCNPs in pH 7.4 and 4.7 for 48 h, which caused approximately 20% and 60% of the drugs to be released. A549 cells incubated with DOX-Ce6-UCNPs, followed by 980 nm laser irradiation with a 1 W/cm² power density, exhibited a reduction in cell viability. For example, A549 cells incubated with DOX-Ce6-UCNPs followed by irradiation (chemotherapy + PDT) displayed 30% cell viability, whereas in the absence of laser irradiation, the use of DOX-Ce6-UCNPs (chemotherapy) led to 60% cell viability. The A549 cells incubated with Ce6-UCNPs, followed by laser exposure (PDT), exhibited a 40% survival rate and 90% cell viability when no laser was used.
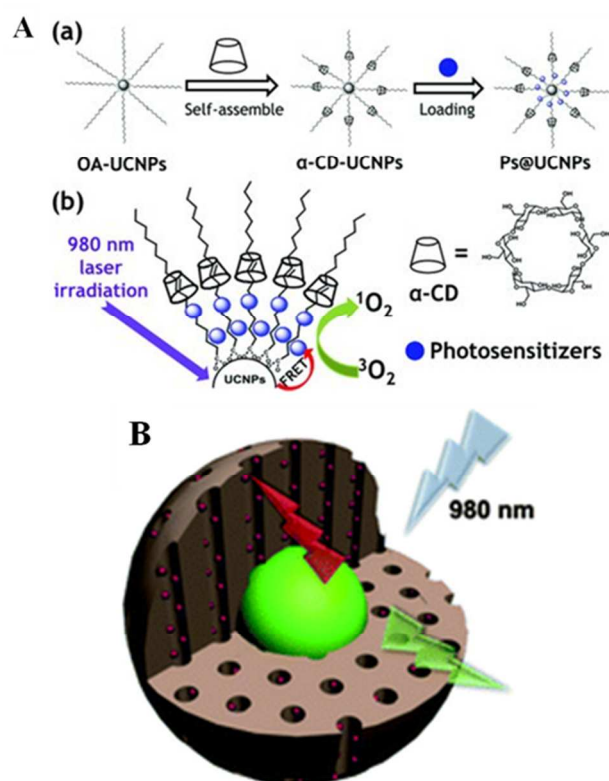
Fig. 15 [A] Schematic illustration of (a) α-CD surface functionalization and Ps@UCNPs (UCNP: Mn^{2+}-doped NaYF$_4$: Yb/Er; Ps: Photosensitizer) that were prepared using the following steps in sequence: UCNPs were coated with α-CD to form α-CD-UCNPs → α-CD-UCNPs were loaded with Ps using hydrophobic interaction to create Ps@UCNPs, and (b) 980 nm NIR-induced PDT using the Ps@UCNPs. [Reprinted with permission from ref. 77. Copyright *Small*, 2013]; [B] Core–shell structured (NaGdF$_4$: Yb, Er@CaF$_2$@SiO$_2$-PS) nanomaterial consisting of NaGdF$_4$: Yb,Er@CaF$_2$ nanoparticles (green sphere) as the core and mesoporous silica (brown sphere) covalently grafted with PSs (small red sphere) as the shell. Under excitation at 980 nm, the nanomaterials emitted luminescence at 550 and 660 nm, in which the former emitted wavelength was used for fluorescence imaging (green arrowhead) and the later was used to achieve the energy absorption of PSs to generate singlet oxygen (red arrowhead). (Reprinted with permission from ref. 86. Copyright *Nanoscale*, 2012.)

Another case of physical adsorption of PSs and UCNPs was developed by Shan *et al.*,[82] who loaded meso-tetraphenyl porphine (m-TPP) over PEG-b-PLA block copolymer-coated hexagonal β-NaYF$_4$:Yb/Er nanoparticles. They used the flash nanoprecipitation (FNP) self-assembly method by which the PSs (m-TPP) and block copolymer were treated together with the UCNPs. By properly adjusting the m-TPP to PEG ratio, they uniformly coated m-TPP and PEG over the UCNPs (PEG-TPP-UCNPs) and demonstrated PDT using an NIR laser. PEG-TPP-UCNPs treated with HeLa cells, followed by the irradiation of the cells using a 978 nm laser with 134 W of power, exhibited cell destruction, whereas the cells treated with PEG-TPP-UCNPs (no laser) exhibited no cell destruction. The use of amphiphilic chitosan as a UCNP modifier has been explained in recent studies based on its excellent biocompatibility and biodegradability.[83] N-succinyl-N'-octyl

chitosan (SOC) was coated on UCNPs (NaYF$_4$:Yb/Er) to improve biocompatibility and hold the ZnPc to administer effective *in vivo* PDT using hydrophobic interaction with the inner OA layer of SOC-coated UCNPs. For the *in vitro* PDT, MCF 7 cells were treated with ZnPc-UCNPs and exposed to a 980 nm NIR laser with 600 mW, which caused cell viability to decrease to 20%; in the treatment without the laser, the cell viability was 90%. S180 murine cancer cell tumor-bearing mice were injected with ZnPc-UCNPs intratumorally and irradiated with a 980 nm laser using a power density of 0.4 W/cm^2 and monitored for 14 days, which caused a 76% reduction in tumor volume compared with that of the untreated control group (no laser). In a similar study, folate-modified chitosan combined with ZnPc-coated UCNPs was explored for *in vivo* targeted deep-seated tumors with an inhibition ratio of up to 50% more than conventional visible light-activated PDT.[84] NaYF$_4$:Yb/Er UCNPs were prepared by performing thermal decomposition using OA capping. In addition, FA was conjugated with amphiphilic N-succinyl-N-octyl chitosan. The FA-conjugated chitosan (FASOC) was coated on the UCNP to form FASOC-UCNP. The FASOC-UCNPs were then loaded with ZnPc using hydrophobic interaction to yield FASOC-PS-UCNPs. The ability of FASOC-PS-UCNPs to generate ROS with pork tissue blocking was analyzed, and a 53% and 17% reduction of the ROS generation signal relative to the unmasked ROS generation ability occurred when a 660- and 974-nm laser was used, respectively. In the *in vivo* experiment, mice bearing S180 tumor cells were intravenously administered with FASOC-PS-UCNPs that inhibited 50%, and 18% of the tumors when a 980- and 660-nm laser was used, respectively, even in the tissue covered with 1-cm-thick pork tissue.

When encapsulating PS, SiO$_2$ comprising a high surface area and mesoporous structure attracted a more favorable host for PS molecules. The porous nature of the silica network prevents the aggregation of PS molecules, which leads to the prevention of self-quenching. Moreover, the porous structure can be tailored to selectively incorporate multiple drugs. In the study by Zhang *et al.*,[85] NaYF$_4$:Yb^{3+}/Er^{3+} was coated with silica using the sol gel method. In the course of sol gel preparation, merocyanine PS molecule was added to dope in the silica coating, in which the absorption energy of 540 nm of merocyanine overlapped the emission of UCNP@SiO$_2$. MCF-7/AZ cancer cells overexpressing MUC1/episialin were used for evaluating PDT performance. UCNP@SiO$_2$-M (M: merocyanine) was coated with antiMUC1/episialin to form antiUCNP@SiO$_2$-M. MCF-7/AZ cells incubated with antiUCNP@SiO$_2$-M, followed by irradiation using a 974 nm diode laser with 60 mW power showed the results of the cells shrinking. Qiao *et al.*[86] individually loaded two types of PSs, silicon phthalocyanine dihydroxide and hematoporphyrin (SPCD and HP, respectively), by covalently grafting them onto mesoporous silica-coated NaGdF$_4$:Yb/Er@CaF$_2$ nanomaterials to achieve effective PDT, as shown in Fig. 15B. The presence of mesopores facilitated the favorable contact of water molecules with Gd ions for performing MRI effectively. Using SPCD-grafted NaGdF$_4$:Yb/Er@CaF$_2$ produced an r_2 value of 2.13 mM/s and using HP-grafted NaGdF$_4$:Yb/Er@CaF$_2$ produced an r_2 value of 1.52 mM/s with an equal Gd concentration. In addition, the presence of

CaF$_2$ coating on the UCNPs decreased the surface-related defects and facilitated the increase in luminescence intensity and biocompatibility. HeLa cells treated with NaGdF$_4$:Yb/Er@CaF$_2$ followed by irradiation using a 980 nm laser caused increase in PDT performance as the laser power density, concentration, and time of laser irradiation increased. Furthermore, cell viability greater than 90% was observed in the group that was not subjected to laser irradiation, which validated PDT. To amplify the therapeutic efficacy of PDT, a method of encapsulating two PS molecules, merocyanine 540 (MC540) and ZnPc, together inside mesoporous silica-coated UCNPs was also developed.[87] The emitted green (approximately 540 nm) and red (approximately 660 nm) wavelengths from the 980-nm excited UCNPs (NaYF$_4$:Yb/Er) were used to activate PS molecules to achieve cytotoxic $^1O_2$ generation. The 540-nm emission of UCNPs overlapped with MC540 excitation and the 660-nm emission of UCNPs matched with ZnPc excitation. For comparison in *in vitro* PDT, B16-F0 melanoma cells were treated with UCNPs co-doped with MC540 and ZnPc (coUCNPs), UCNPs doped with MC540 (MC-UCNPs), and UCNPs doped with ZnPc (Zn-UCNPs), followed by irradiation using a 980-nm laser with a power density of 2.5 W/cm^2. The cells treated with MC-UCNPs or Zn-UCNPs exhibited > 60% cell viability, whereas the cell viability of the cells treated with coUCNPs decreased to approximately 42%, thereby demonstrating the efficiency of the combined PDT.

F.2 Covalent interaction

Covalent interaction between PSs and UCNPs is developed to prevent the premature release of PS molecules before reaching the targeted cancer cells. Covalent bonding among PS, pyropheophorbide-a, and RGD peptides on the chitosan-modified UCNPs (NaYF$_4$:Yb/Er) was prepared by Zhou *et al.*[88] In their study, polyethylenimine-coated UCNP was wrapped with chitosan (chi), the amino groups of which were protected by boc anhydride (di-tert-butyl dicarbonate), to conjugate the carboxyl groups with the amines of polyethylenimine through amide bonding. The residual carboxyl groups in chi-UCNP were then conjugated with the amines of the targeting RGD to generate RGD-chi-UCNP. The carboxyl groups of the PS were subsequently attached to the protected amine groups on the RGD-chi-UCNP through deprotection, which produced the complex PS-RGD-chi-UCNP. In *in vitro* experiments involving the use of PS-RGD-chi-UCNPs, these covalently bonded nanoconstructs exhibited low dark toxicity, and high phototoxicity and selectivity against cancer cells when subjected to 980 nm laser irradiation. U87-MG (overexpression of the integrin) cells were labeled with ROS sensor DCFH-DA (dichloro-dihydro-fluorescein diacetate) and displayed fluorescence in the confocal images when incubated with PS-RGD-chi-UCNPs, followed by laser exposure, whereas the fluorescence was weak when the treatment without laser irradiation was used. To demonstrate the selectivity of the PS-RGD-chi-UCNPs to U87-MG cells, PDT was quantified using MCF 7 (less expression of the integrin) cells as the negative control. U87-MG and MCF 7 cells incubated with PS-RGD-chi-UCNP followed by 980 nm laser exposure with a power density of 0.5 W/cm^2 exhibited 40% and 90% cell viability, respectively. Similarly, additional amounts of PS were

accommodated by obtaining approximately 100 PSs per UCNP using hexanoic acid-modified rose bengal (RB-HA) and amino functional UCNPs (NaYF$_4$:Yb/Er), as shown in Fig. 16.[89] The oleylamine on the as-prepared UCNP was replaced using 2-aminoethyl dihydrogen phosphate (AEP) to include the presence of amine functional groups. The amine groups on the UCNPs were covalently conjugated with the carboxyl groups of hexanoic ester comprising the rose bengal PS (RB) using a carbodiimide link to form RB-UCNP. Because of the presence of covalently bonded RB molecules, it was demonstrated that the emission energy of UCNPs produced favorable absorption levels for achieving improved PDT. More than 80% of upconversion luminescence was transferred to PSs by using this strategy of covalent conjugation for singlet oxygen production. RB-UCNP was further conjugated using FA through heterobifunctional PEG (NH$_2$-PEG-COOH) to form FA-PEG-RB-UCNP. For the *in vitro* uptake analysis, JAR human placenta cancer cells were treated with FA-PEG-RB-UCNPs and observed using a confocal microscope. The image showed that the UCNPs were distributed in the cytoplasm, whereas the NIH3T3 normal fibroblast (folate negative) cells incubated with FA-PEG-RB-UCNPs showed no fluorescence. In addition, JAR cancer cells saturated with free FA followed by incubation with FA-PEG-RB-UCNPs displayed no UCNP fluorescence in the cytoplasm. This confirmed that the incorporation of FA led to the targeting of FA-PEG-RB-UCNPs. JAR cells treated with FA-PEG-RB-UCNPs followed by 980 nm laser irradiation with a power density of 1.5 W/cm^2 exhibited complete cell death, whereas the cell viability was approximately 90% when the treatments without irradiation or those involving NIH 3T3 cells treated with FA-PEG-RB-UCNPs with or without a laser were used.
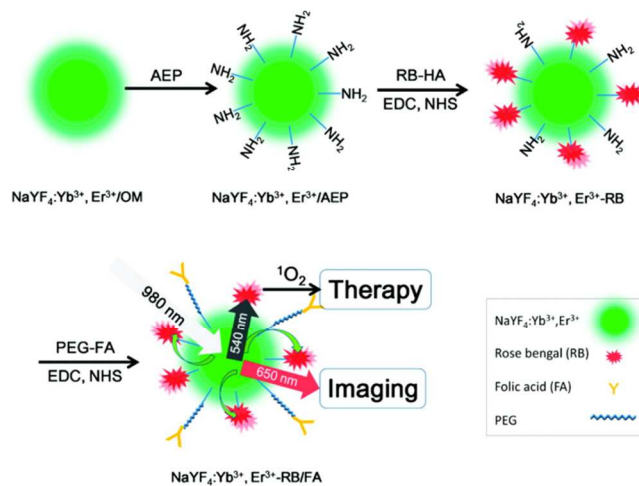

Fig. 16. Covalent conjugation of NaYF$_4$:Yb^{3+}/Er^{3+}, hexanoic acid-modified rose bengal (RB-HA), and targeting molecule folic acid (FA) for PDT and imaging functionalization. UCNP was coated using 2-aminoethyl dihydrogen phosphate (AEP) → amines of AEP on UCNP conjugated covalently with carboxyl groups of hexanoic ester of RB-HA forming RB-UCNP → FA conjugated to RB-UCNP through PEG (NH$_2$-PEG-COOH) yielding FA-PEG-RB-UCNP. FA-PEG-RB-UCNP was excited with a 980-nm laser and emission was observed at 540 nm and

650 nm for PDT and imaging, respectively. (Reprinted with permission from ref. 89. Copyright *ACS Nano,* 2012.)

An electrostatic interaction between covalently bonded Ce6 over succinic anhydride (SA) blocked poly(allylamine hydrochloride) (PAH) and UCNPs (Mn^{2+} ion-doped NaY(Mn)F$_4$: Yb/Er nanocrystals (Y:Mn:Yb:Er = 50:30:18:2)) coated with polyacrylic acid (PAA) and PAH using LBL assembly was explained by Wang *et al.*[90] In this work, PS molecules were coated with multiple layers (up to 3 coats) and the upconversion emission was tuned by doping with manganese to obtain high-intensity red emission at 660 nm for PS activation. Briefly, the PAH was conjugated with the NHS-activated Ce6 and then the remaining amines were blocked in PAH with SA, thereby causing PAH-Ce6-SA to have a negative charge. In addition, the Mn-doped UCNP coated with PAA was charge inverted by using PAH coating, which caused the UCNP/PAA/PAH to have a net positive charge. PAH-Ce6-SA was loaded on the UCNP/PAA/PAH using LBL assembly with alternative PAH to form UCNP@PAH/PAH-Ce6-SA. Simultaneously, pH-sensitive dimethylmaleic acid (DMMA) and PEG were grafted in PAH to form DMMA-PAH-PEG (negative charge). DMMA enabled charge conversion from a negative to positive charge at the acidic tumor site to enhance uptake. UCNP@PAH/PAH-Ce6-SA was subsequently coated with DMMA-PAH-PEG to form UCNP@DMMA. As a control group, the pH-insensitive polymer PAH was grafted with PEG and SA, and then coated on UCNP@PAH/PAH-Ce6-SA to form UCNP/SA. Consequently, the HeLa cells treated with UCNP@DMMA exhibited enhanced upconversion luminescence compared with that of the cells treated with UCNP@SA, as shown in Fig. 17. HeLa cells treated with UCNP@DMMA and exposed to a 980 nm laser with a power density of 0.4 W/cm^2 were destroyed more compared with the cells treated with UCNP@SA using a laser. In *in vivo* experiments, UCNP@DMMA or UCNP@SA was intratumorally injected in mice bearing 3T3 cell tumors followed by irradiation with a 980 nm laser with a power density of 0.5 W/cm^2, and the tumor volume was monitored for 12 days. Both UCNP@DMMA and UCNP@SA were subject to a laser and demonstrated tumor volume control compared with those that underwent the treatment without a laser. However, UCNP@DMMA displayed substantially more volume control than UCNP@SA did. In parallel to the observations of the therapeutic effects, the T$_1$-weighted MR image showed a slow decline in the UCNP@DMMA signal compared with that of the UCNP@SA, which declined rapidly, indicating the high uptake ability of UCNP@DMMA. This slow decline was because the pH-sensitive charge conversion property of DMMA (to positive charge) enabled enhanced uptake before the loss caused by circulation from the intratumoral injection site occurred.
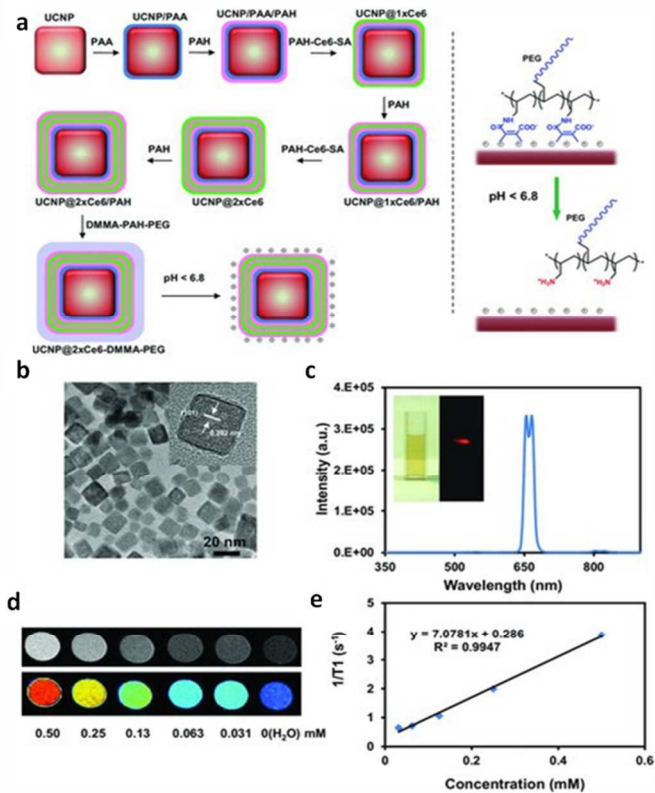

Fig. 17 Schematic illustration and characterization of pH-responsive smart theranostic UCNPs (Mn^{2+} ion-doped NaY(Mn)F$_4$: Yb/Er nanocrystals (Y:Mn:Yb:Er = 50:30:18:2)). (a) A schematic showing the fabrication process of pH-sensitive charge-reversible UCNPs with multilayers of Ce6 loading; right panel: the detachment of DMMA-PAH-PEG from the positively charged nanoparticle surface under < pH 6.8. (b) TEM micrograph of Mn^{2+}-doped UCNPs; inset: high-resolution TEM image of a UCNP. (c) An upconversion luminescence spectrum of Mn^{2+}-doped UCNPs under 980 nm laser excitation; inset: photograph of a UCNP solution under ambient light and under 980 nm laser excitation. (d) T$_1$-weighted MR images of UCNP solutions at various Mn^{2+} concentrations. (e) T$_1$ relaxation rate (r_1) of UCNP solutions at various Mn^{2+} concentrations. (Reprinted with permission from ref. 90. Copyright *Adv. Funct. Mater.*, 2013.)

F.3. Upconversion nanoparticles with Drug delivery

UCNP-mediated drug delivery can be categorized into two methods. In the first method, the chemotherapy drug is accommodated inside the mesoporous silica cavity or carrier through the hydrophobic interaction with OA-coated UCNP, in which the drug can release by the change in pH, which facilitates the change in the nature of drug molecules from one form to another (especially at low pH, the hydrophobic drug is protonated for conversion into a hydrophilic drug, and is consequently released inside the cancer cell microenvironment). In this type, the UCNPs were used for image-guided monitoring of the drug delivery.[91-98] For example, Tian *et al.*[91] fabricated red emission enhanced upconversion luminescence

material comprising $NaYF_4$:Yb/Er doped with Mn^{2+} ions. By properly adjusting the synthesis condition, they achieved a red to green intensity ratio (I_R/I_G) from 0.83 to 163.78 for treatment without Mn^{2+}- and with 30 mol% Mn^{2+}-doped UCNPs, respectively. To demonstrate the tissue luminescence imaging ability of UCNPs, the mice were injected with DOX-UCNPs that exhibited particle concentration-dependent luminescence. The lipophilic DOX drugs were loaded into Mn-doped UCNPs through hydrophobic interaction with OA-coated UCNPs. DOX loading was estimated as 8.8% (w/w) in neutral phosphate buffer. To measure the drug release, *in vitro* experiments were conducted under two pH conditions (pH 7.4 and 5.0) to simulate the intracellular cancer cells environment. A slow DOX release of approximately 19.1% after 48 h was observed when pH 7.4 was used, whereas a cumulative release of 50.5% was seen within 48 h when pH 5 was used. This pH-dependent drug release was exploited in controlled drug delivery applications. A549 cells treated with DOX-UCNPs exhibited 10% cell viability, and the survival rate was 30% for the free DOX. In another study, porous $NaYF_4$:Yb/Er@SiO_2 nanocomposite was synthesized using the electrospinning process.[94,98] OA-coated UCNPs were synthesized using the decomposition method and were transferred into the water phase using CTAB coating and treated with P123 (block copolymer composed of poly(ethylene oxide), poly(propylene oxide)) and tetraethyl orthosilicate to form a composite P123-UCNP. The P123-UCNP was then mixed with TEOS and PVP (to increase the viscosity for electrospinning) to form a gel. This gel was electrospinned to prepare a fiber precursor, which was calcined at 550° C to create porous UCNP@silica fiber nanocomposites. The drug loading and releasing property was monitored by using either ibuprofen[94] or DOX.[98] The ibuprofen was adsorbed in the silica pore through the impregnation process and was released by the diffusion-controlled mechanism in which solvent molecules replaced the drugs inside the porous silica. The upconversion emission was quenched by the loaded drugs; thus, the upconversion fluorescence was recovered once the drugs were released. By considering this property, the release of the drugs was monitored using the appearance of the upconversion fluorescence. Regarding the DOX-loaded UCNP silica nanocomposites, the release of DOX was based on a change in pH in which the DOX became protonated at a lower pH; thus, the release occurred because of the reduction in electrostatic force. Regarding the *in vitro* chemotherapeutic effect, DOX-UCNP@silica displayed enhanced toxicity when the DOX loading amount increased.

In the second method, the cancer drug is bonded with the photolabile group, which was cleaved by emitted ultraviolet radiation produced by the UCNPs. This strategy eliminates direct exposure to UV radiation, which is harmful to normal tissue and has a limited penetration depth. The intense emission at 360 nm from "Tm"-doped $NaYF_4$: Yb UCNPs was employed for the purpose of analyzing photoinduced cleavage reactions. In the study subject, the release of payload by the photocleavage of the o-nitrobenzyl group from poly (ethylene oxide)-block-poly (4,5-dimethoxy-2-nitrobenzyl methacrylate) induced by the emitted UV photons from UCNPs was explored.[99] The photo-cleavage reaction caused the dissociation of block copolymer (BCP) micelle and the release of coloaded

hydrophobic species. To demonstrate this effect, Nile Red (NR) dye was used as a model hydrophobic compound and coloaded with BCP and UCNPs for the formation of micelles in an experiment that was conducted using the setup shown in Fig. 18. By comparing the absorption maximum of nitrosobenzaldehyde in the 350–450 nm region with or without NIR laser radiation, it was proved that the release of hydrophobic NR was based on the cleavage of the o-nitro benzyl groups in the micelle core when subjected to 980 nm NIR laser excitation. Similarly the release of a model compound, the carboxylic acid group cleaved from the 3', 5'-di (carboxymethoxy) benzoin cage by applying UV emission from UCNPs, was demonstrated by Carling *et al.*[100] In this study, they synthesized β-$NaYF_4$, 0.5% Tm^{3+}, 30% Yb^{3+}/β-$NaYF_4$ core/shell nanocrystals, and then decorated the shell with 3', 5'-di (carboxymethoxy) benzoin acetate molecules by simple stirring in tetrahydrofuran solution overnight. The loaded 3', 5'-di (carboxymethoxy) benzoin acetate exhibited an absorption maxima of 282 nm, which partially overlaps with the emission spectrum of UCNPs (290 nm). The release of acetic acid was demonstrated by a high yield caused by irradiation that was applied by using either 313 nm UV radiation or 980 nm NIR radiation. In addition to the release of either payload or organic moieties, several other reports related to the efficient expression of nucleic acids[101] and d-luciferin[102] caused by the emitted UV radiation from UCNPs have been addressed. Among these reports, we discuss those that reported the green fluorescence protein (GFP) in DNA expression for as-prepared NaYF4: Yb/Tm UCNPs that were coated with silica and mesoporous silica in sequence (UCNPs@SiO_2@mesoSiO_2). The 4,5-dimethoxy-2-nitroacetophenone photocage molecule, which can bind to DNA phosphate backbone and inhibit DNA expression, was used to cage the GFP-expressing plasmid, which was designated as the cage-plasmid complex. Cage-plasmid was loaded into the mesopores in the UCNPs@SiO_2@mesoSiO_2 using adsorption forming UCNPs/silica/cage-plasmid. In the *in vitro* examination, the cells incubated with UCNPs/silica/cage-plasmid expressed green fluorescence only when subjected to 980 nm laser irradiation, and the green fluorescence intensity increased as the power density increased.
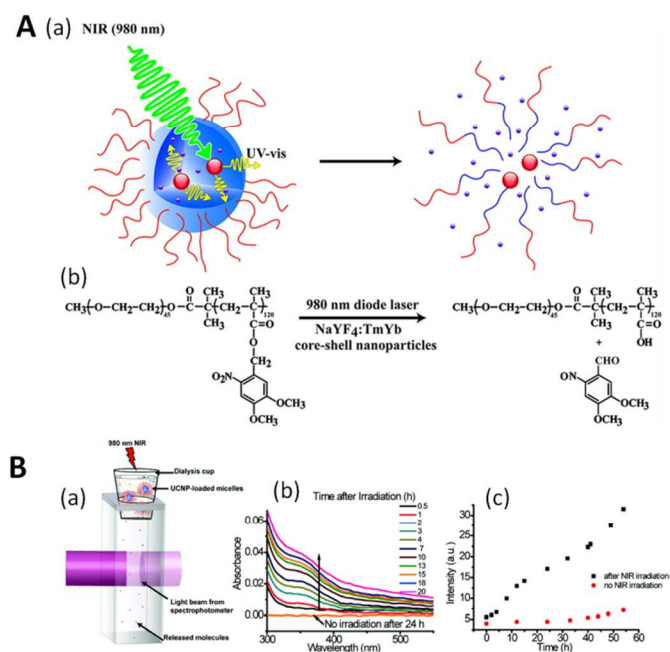
Fig. 18 [A] (a) Schematic illustration of using NIR light excitation on UCNPs to trigger the dissociation of BCP micelles. (b) NIR light-triggered photoreaction using the PEO-b-PNBMA (BCP) and NaYF4: Tm/Yb UCNPs. [B] (a) Setup used to detect species diffusing from a BCP micellar solution through a dialysis membrane into aqueous solution underneath. The diffusing molecules were either photocleaved nitrosobenzaldehyde or Nile Red (NR) released from disrupted BCP micelles as a result of 980 nm NIR laser excitation. (b) Absorption spectral change over time for nitrosobenzaldehyde molecules cleaved by the NIR light exposure of UCNP-loaded micelles. (c) Increase in the normalized fluorescence intensity of NR dye measured at 640 nm (λ_{ex} = 550 nm) over time for two aqueous micelle solutions loaded with both UCNPs and NR dye, one of which was subjected to NIR light exposure, whereas the other was not. (Reprinted with permission from ref. 99. Copyright *J. Am. Chem. Soc.*, 2011.)

Accordingly, the photolabile molecule can be used to mask the cancer drugs and is unlocked by NIR-induced UV light once the nanoparticle enters the cancer cells. This helps prevent the unwanted release of cancer drugs and side effects. Moreover, the photolabile group can be used to mask the targeting molecule, FA, to prevent the unwanted targeting of normal cells, which also possess folate receptors as in kidneys.[103] The photolabile groups were removed once they reached the cancer cells. Chien *et al.*[104] recently explored this strategy of masking FA by using the photolabile 2-nitrobenzylamine group, and unmasking FA using UV emission from NaYF4: Yb/Tm, as shown in Fig. 19. This approach prevented the unwanted targeting of FA. The as-prepared UCNP was coated with SiO2 and APTES to achieve hydrophilicity using exposed amine functional groups. The amines in UCNPs@SiO2 were partially conjugated with homobifunctional PEG (HOOC-PEG-COOH) and the residual amines were bound with thiolated DOX using N-succinimidyl 3-(2-pyridyldithio)-propionate (SPDP), a cross-linking group, to form DOX-PEGylatedUCNP@SiO2 composite. In parallel,

the carboxyl groups in the targeting FA were masked using the photosensitive cage 2-nitrobenzylamine to form caged folates. The amines in the caged folates were then conjugated with DOX-PEGylatedUCNPs@SiO2 composite to form caged folate-DOX-PEGylated UCNPs@SiO2. *In vitro* and *in vivo* studies have verified that caged UCNPs can serve as a platform for improving selective targeting. Thus, the uptake of caged folate-DOX-PEGylated UCNPs@SiO2 for photoactivation using a 980 nm diode laser with a power density of 11 W/cm^2 was determined to be 2.5 times greater in HeLa cells (folate receptor-positive) than in A549 (folate receptor-negative) cells. In the *in vitro* chemotherapy, HeLa cells treated with caged folate-DOX-PEGylated UCNPs@SiO2 accompanied by laser irradiation showed the cell death comparable with that of the uncaged FA-conjugated UCNPs. In addition, the cell viability was maintained above 90% during the treatment of caged folate-DOX-PEGylated UCNPs@SiO2 without the laser irradiation. Based on these results, the phototargeting effect of caged folate-DOX-PEGylated UCNPs@SiO2 was further examined *in vivo* using tail vein injection on mice bearing HeLa cell tumors. The mice group treated with caged folate-DOX-PEGylated UCNPs@SiO2 and laser exposure demonstrated a significant decrease in tumor size compared with the group that received treatment without the use of a laser.
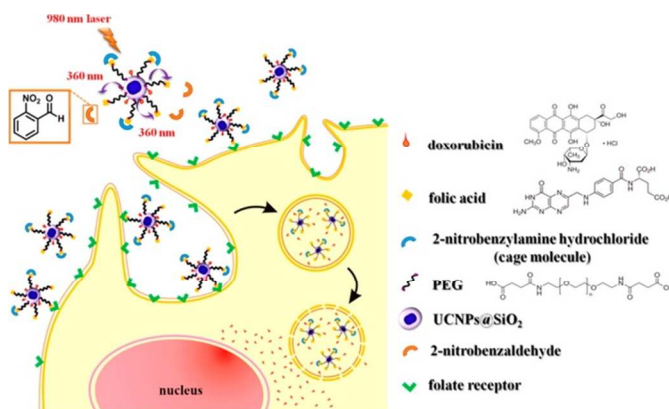

Fig. 19 The targeting folic acid groups on the drug-loaded UCNPs were masked by **a** photolabile 2-nitrobenzylamine cage to enable the cargo to enter the cells only after NIR laser irradiation, in which the photolabile cages were cleaved by the upconversion UV emission. (Reprinted with permission from ref. 104. Copyright *ACS Nano*, 2013.)

F4. Photothermal therapy using UCNPs

UCNPs are typically excited by 980 nm laser radiation. Because the absorbance of water falls at this wavelength region, precautions are made to avoid heating interference from occurring by reducing the laser power density or duration. Consequently, no report on upconversion-mediated PTT is available. Nevertheless, several studies have used UCNPs as an imaging-guided source combined with NIR-absorbing materials for conducting image-guided PTT. The magnetically targeted dual modal imaging multifunctional nanoparticles (MFNPs) was synthesized for PTT.[105, 106] For example, the LBL assembly method was introduced to synthesize MFNPs.[106] Polyacrylic acid-modified UCNPs (NaYF4:

Yb/Er) were used as the core and dopamine-modified IONPs were coated on UCNPs using electrostatic interaction adsorption (UCNP@IONP). A thin layer of gold was then grown over UCNP@IONP using the seed-mediated reduction method, which led to the creation of UCNP@IONP@Au (MFNPs). The MFNPs were PEGylated with lipoic acid-conjugated PEG to achieve dispersion and biocompatibility (MFNP-PEG). The strong surface plasmon resonance (SPR) of the Au shell at 800 nm was used for PTT and IONP coating were utilized for MRI and magnetic targeting, as shown in Fig. 20. The magnetic targeting was verified in mice bearing 4T1 murine breast cancer tumors. For PTT, mice injected with MFNP-PEG irradiated with an 808 nm laser using a 1 W/cm^2 power density exhibited a drastic temperature increase to 50° C, whereas in the untreated control the temperature was 38° C. Using MFNP-PEG with magnetic targeting and laser irradiation caused the tumors to disappear in the mice, whereas the tumor volume continued to increase when the treatment involving MFNP-PEG and a magnet (no laser) or laser only (no MFNP-PEG) was used. Using MFNP-PEG with magnetic targeting and laser irradiation enabled survival for the complete 40 daya of the monitoring period, whereas when other treatments were used, the maximal survival was only up to 18 days.
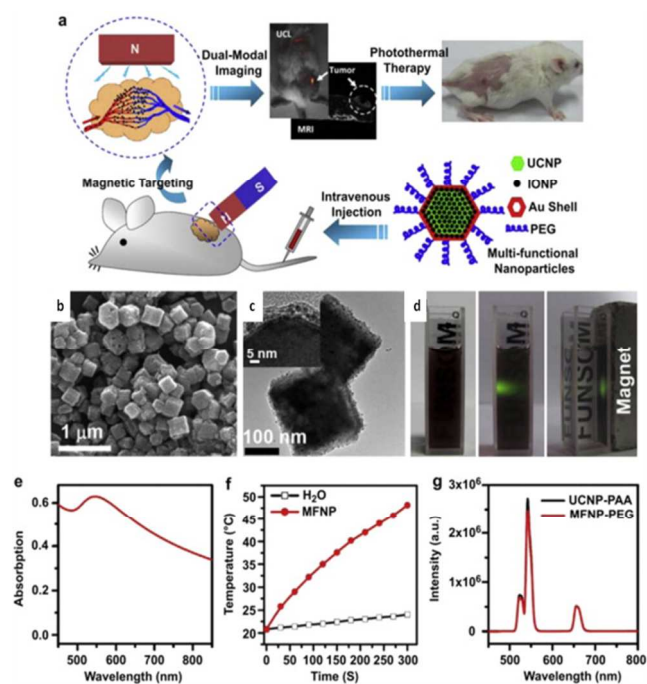

Fig. 20 Multifunctional composite nanoparticles used for imaging-guided cancer therapy. (a) A schematic illustration showing the composition of an MFNP-PEG and the concept of *in vivo* imaging-guided magnetically targeted PTT. The magnetic field around the tumor region induced local tumor accumulation of MFNP-PEG. (b) A SEM image of MFNP-PEG. (c) A TEM image of MFNP-PEG. The inset is a high-resolution TEM image. (d) Photographs of the MFNP-PEG sample in aqueous solution under ambient light (left), exposed to a 980 nm laser (middle), and with a magnet (right). (e) UV/Vis absorption spectrum of the MFNP-PEG solution. (f) Temperature curves of water and the MFNP-PEG solution exposed to an 808 nm laser at a power density of 1 W/cm^2. (g) Upconversion luminescence spectra of UCNP-PAA and MFNP-PEG at the same

Y^{3+}-concentration. [Reprinted with permission from ref. 106. Copyright *Biomaterials,* 2012]

Another theranostic platform of upconversion luminescence-guided PTT and PDT was demonstrated by Wang *et al.*[107] using UCNPs-GO/ZnPc. The as-prepared UCNPs (NaYF$_4$: Yb^{3+}/Er^{3+}/Tm^{3+}) were coated with poly(allylamine) (PAAm) by replacing OA. In addition, GO was functionalized using the heterobifunctional PEG (NH$_2$-PEG-COOH) through amide bonding between the amine ends of the PEG and carboxyl groups in GO. The remaining carboxyl ends of the PEG were tethered with the amines of the UCNP to form UCNPs-GO. The π-π stacking strategy was used to load ZnPc onto the GO of UCNPs-GO to form UCNPs-GO/ZnPc. The strong absorption of PS molecules at 630 nm, ZnPc, and 808 nm, GO, was used for PDT and PTT by applying the respective laser irradiation. The uptake of UCNPs-GO by HeLa and KB cells in cytoplasm was confirmed by the fluorescence observed upon 980 nm laser excitation. Regarding therapeutics, HeLa cells treated with UCNPs-GO/ZnPc, followed by either 808 nm laser (2 W/cm^2), 660 nm laser (50 mW/cm^2), or combination irradiation (808 nm laser followed by 630 nm laser) exhibited 75%, 50%, and 15% cell viability, respectively.

G. Other related materials

The necessity of NIR-absorbing materials in biomedical applications motivates researchers to develop new nanomaterials with excellent NIR absorbance. Materials with high optical SPR absorption in the NIR region are currently under intensive investigation for use in PTT. In this field, gold and carbon-related materials dominate over other materials because they exhibit high absorption in the visible and NIR regions. The lack of photothermal stability exhibited by Au-related materials[47] during the continual excitation of NIR radiation can be remedied by choosing other NIR-absorbing metal nanoparticles or composite materials, which have the potential to convert the NIR radiation to thermal energy that are either similar or superior to Au-related nanomaterials.[108] Therefore, in this section, we emphasize the importance of these related materials.

G. 1. CuS/Se related materials

Copper-based semiconductors have gained recognition as biocompatible, low-cost, low-cytotoxic semiconductors in recent years. Compared to Cd-containing contrast agents, which are toxic, Cu semiconductor nanomaterials have become increasingly crucial in *in vivo* cancer imaging and other applications. Unlike the SPR of Au-related materials, which can be affected by the dielectic constant of the surrounding medium,[109] the p-type semiconductor CuS has a d-d transition band with an absorption in the NIR region, which is independent of the dielectic constant of the medium. To apply this NIR-absorbance property of CuS nanoparticles to PTT, CuS nanoparticles were synthesized by using the reaction of CuCl$_2$ with Na$_2$S.[110] The synthesized CuS nanoparticles were PEGylated by incubating them with SH-PEG overnight to form PEG-CuSs. The PEG-CuSs underwent irradiation applied using an 808 nm diode laser with a power density of 16 W/cm^2 for 5 min, and the temperature subsequently increased to 80° C. In *in vitro* PTT, U87

glioma cells treated with PEG-CuSs exhibited a substantial reduction in the amount of live cells when irradiated with an 808 nm diode laser using 16 and 40 W/cm^2 power densities. U87 tumor-bearing mice were injected with PEG-CuSs intravenously, which were allowed to accumulate for 24 h. Subsequently, the tumor was irradiated using a laser with a 12 W/cm^2 power density for 5 min, which caused tumor tissue to burn. This tumor tissue was analyzed histologically and enhanced necrotic symptoms were observed in the group that had received PEG-CuSs (with laser irradiation). However, the necrotic symptoms were negligible in the mice treated with PEG-CuSs (without laser irradiation), saline (with laser irradiation), or untreated control group (no PEG-CuSs and no irradiation). Moreover, this CuS nanoparticle was considered to be able to overcome the inherent limitation associated with a radiometal-chelator complex conjugated on any nonradiative carrier nanoparticles. The main disadvantage of nonradiative carrier nanoparticles is the detachment or displacement of the radiometal-chelator complex from its coating, which creates ambiguity in diagnosis. Therefore, using chelator-free radioactive nanopatricles was desired for *in vivo* and pharmacological studies. Thus, [^{64}Cu]CuS, a chelator-free radioactive nanoparticle was formed by substituting CuCl$_2$ partially with ^{64}CuCl$_2$ in the synthesis of the CuS nanoparticles.[110] The integration of ^{64}Cu into the core structure comprising [^{64}Cu]CuS was ideally suited for diagnostic applications. The potential of PEG-[^{64}Cu]CuS to serve as a PET image contrast agent was demonstrated by the particles accumulating in the liver and spleen over time; this observation was in accordance with biodistribution data.

The photothermal transduction efficiency of CuS was further improved by harvesting the reflected radiation. To achieve this photothermal enhancement, a CuS superstructure (super-CuS) was designed as a flower-like structure that could produce almost 2 times the absorption intensity of simple hexagonal CuS nanoplates in the NIR region.[111] The large, adequately aligned nanoarray with flower-like superstructures was demonstrated to act as a laser-cavity mirror to improve the reflection and absorption ability of a 980 nm laser, as shown in Fig. 21. Thus, when using a 980 nm laser with a 0.5 W/cm^2 power density, the super-CuSs exhibited a 17° C temperature increase in 5 min, whereas in contrast, the CuS nanoplates exhibited only a 11.5° C increase in temperature. HeLa cells treated with super-CuSs were irradiated using a 980 nm laser with a 0.5 W/cm^2 power density in PTT. To employ the ability of the super-CuS to absorb a 980 nm laser that can penetrate deep into tumor tissue during PTT, the HeLa cells were covered by chicken skin during irradiation. Although the chicken skin covered the HeLa cells during PTT, damage was observed based on the results of tryphan blue staining. During *in vivo* PTT, mice bearing PC 3 tumor xenografts were intratumorally injected with super-CuSs and irradiated using a 980 nm laser with a power density of 0.5 W/cm^2. The tumor sections obtained by the microtome after hematoxylin/eosin staining revealed necrotic symptoms were present, whereas the tumor sections obtained from the mice treated with water (with laser irradiation) did not exhibit such symptoms. More detail on the various applications of CuS, including biomedical

applications, and the associated synthesis procedure can be obtained from a recent review published by Goel *et al.*[112]

Similar to CuS nanomaterials, the amphiphilic polymer-coated Cu$_{2-x}$Se nanocrystal was demonstrated to be an effective photothermal transduction agent.[113] Cu$_{2-x}$Se nanoparticles were prepared by using the thermal precipitation of CuCl$_2$ and selenourea in oleylamine. Cu$_{2-x}$Se nanoparticles in oleylamine were coated with amphiphilic oleylamine coupled poly(isobutylene-alt-maleic anhydride) to form hydrophilic Poly-Cu$_{2-x}$Se (polymer coated Cu$_{2-x}$Se). The photothermal conversion efficiency of Poly-Cu$_{2-x}$Se was comparable to those of the Au NRs and Au nanoshells when exposed to an 808 nm laser with a 2 W/cm^2 power density. These Cu$_{2-x}$Se nanoparticles were small in size, approximately 16 nm in diameter, which rendered them suitable for prolonged blood circulation and improving targeting efficiency. HCT-116 human colorectal carcinoma cells treated with Cu$_{2-x}$Se followed by irradiation using an 800 nm diode laser with a power density of 30 W/cm^2 were destroyed, whereas photothermal cell destruction was not observed in either the cells treated with Cu$_{2-x}$Se (without laser) or the cells treated with laser irradiation alone (without Cu$_{2-x}$Se).
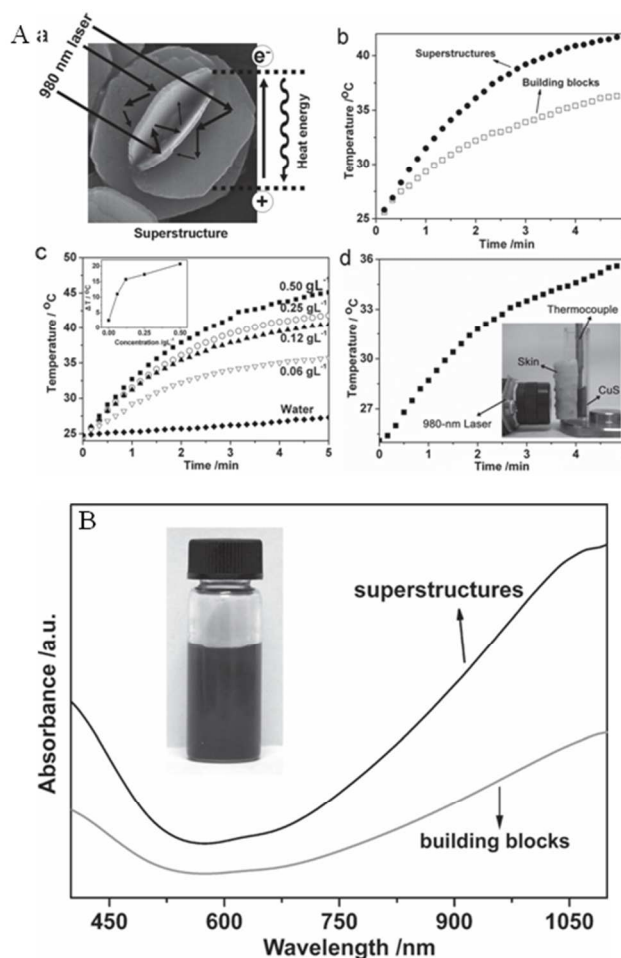

Fig. 21 [A] (a) Schematic representation of a CuS superstructure serving as a laser-cavity mirror for a 980 nm laser and photothermal conversion process. (b) The temperature elevation of the aqueous dispersion containing the CuS superstructures and the CuS hexagonal nanoplates (building blocks), with the concentration of

0.25 g L^{-1} as a function of irradiation time when the 980 nm laser was used with a power density of 0.51 W cm^{-2}. (c) The temperature elevation of the aqueous dispersion containing CuS superstructures with various concentrations as a function of irradiation time, and water was used as a control. Inset: Plot of temperature change (ΔT) over a period of 5 min versus CuS superstructure concentrations. (d) The temperature elevation of the aqueous dispersion of CuS superstructures (0.25 g L^{-1}) coated with chicken skin as a function of irradiation time when the 980 nm laser was used. The inset shows a photograph of the measuring facility in which the temperature was recorded. (B) Absorption spectra of the aqueous dispersion (0.02 g L^{-1}) of as-synthesized CuS superstructures and comparable CuS hexagonal nanoplates (building blocks). Inset: The photograph shows the CuS superstructures dispersed in water after 1 week. (Reprinted with permission from ref. 111. Copyright *Adv. Mater.*, 2011.)

G. 2. Fe$_3$O$_4$ related systems

Biocompatible and nontoxic superparamagnetic IONPs have been used for theranostic applications in the field of biomedical research. The surface-modified magnetic nanoparticles with absorption in the NIR region have prompted the development of a new field of research on the photothermal ablation of cancer cells.[114,115] For example, benzene-1,3,5- tricarboxylic acid (trimesic acid (TMA)) ligand-assisted IONPs exhibited NIR absorbance.[114] This behavior in IONPs was caused by the ligand-induced surface effect that encouraged d-d transition. The resulting IONPs were further coated with mesoporous silica and APTES to achieve sufficient dispersion (IONP@mSiO$_2$). This silica coating did not affect the optical property of IONP@mSiO$_2$ with respect to the IONP. Furthermore, subjecting the IONP@mSiO$_2$ to irradiation using an 808 nm laser with a power density of 2 W/cm^2 increased the temperature to 44° C in 4 min, in contrast with that of commercial iron oxides, Resovist, which did not exhibit a photothermal effect. In addition, IONP@mSiO$_2$ also showed concentration-dependent darkness during T$_2$-weighted imaging. IONP@mSiO$_2$ treated with KB cells and irradiated with a power density of 2 W/cm^2 caused the cell viability to reduce to 15%. In the *in vivo* study, the intratumoral injection of IONP@mSiO$_2$ followed by NIR laser irradiation caused the temperature of the tumor to increase to 47° C from 34° C, which was observed using a thermographic camera.

Li *et al.* used a magnetic field to enhance PDT in their study.[116] Fe$_3$O$_4$ nanocrystals (IONCs) were synthesized by using thermal decomposition of FeCl$_3$ in ethylene glycol and diethylene glycol. The IONCs were then functionalized with PEG using a grafted polymer, dopamine-polyacrylic acid-PEG, to form IONC-PEG. The IONC-PEG was loaded with Ce6 PS to obtain IONC-PEG-Ce6. The IONC-PEG-Ce6 exhibited a red shift in the absorbance peak of Ce6 (from approximately 650 nm to 700 nm). Thus, the resulting IONCs were excited by a 704 nm NIR laser used in PDT. In the presence of an external magnetic field, 4T1 murine breast cancer cells incubated with IONC-PEG-Ce6 (equivalent to 0.65 µM/mL Ce6) followed by 704 nm laser irradiation with a power density of 5 mW/cm^2 exhibited 90% photothermal cell destruction. In addition, the cells incubated with the same concentration of Ce6 (0.65 µM/mL Ce6), followed by 660 nm laser irradiation with a 5

mW/cm^2 power density, only 30% of the cells were destroyed. For the *in vivo* experiment, the mice bearing 4T1 cell tumors intravenously injected with IONC-PEG-Ce6 under the external magnetic field and irradiated with a 704 nm laser using a power density of 5 mW/cm^2 exhibited control over tumor volume for 16 days, as shown in Fig. 22. In the control mice group that was injected with IONC-PEG-Ce6 and subsequently subjected to either the laser (no magnetic field) or magnetic field (no laser irradiation), the tumor size increased. A similar type of magnetic targeting used for combined PDT and chemotherapy was reported: DOX delivery in the presence of magnetically promoted cellular uptake with NIR-absorbing polypyrrole-coated magnetic INOP.[117]
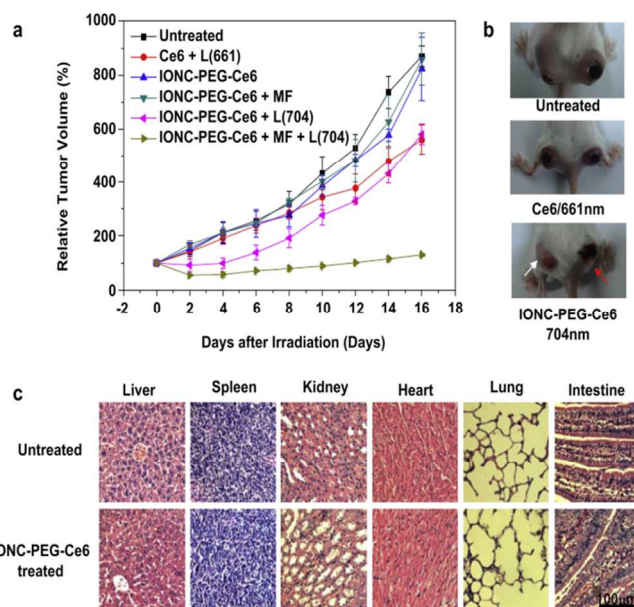

Fig. 22. *In vivo* MF-enhanced PDT: (a) Tumor growth behavior of tumor groups after undergoing various treatments as indicated. Error bars were based on the standard deviation of six tumors per group. MF: magnetic field; L: light. (b) Representative photographs of mice after undergoing various treatments. Red and white arrows point to tumors with and without magnetic targeting, respectively. (c) H&E stained images of major organs collected from healthy mice that were untreated and injected with IONC-PEG-Ce6 20 days later. (Reprinted with permission from ref. 116. Copyright *Biomaterials,* 2013.)

G.3. Carbon nanotubes

The strong optical absorption and high photon-to-thermal energy conversion efficiency of CNTs in the NIR region combined with a high-absorption cross-section make CNTs a suitable candidate for photothermal therapy.[118–123] For example, multiwall carbon nanotubes (MWCNTs) enhanced tumor volume control and the survival rate.[118] Here, the MWCNTs were dispersed in the physiological saline containing biocompatible surfactant pluronic F127 (1% w/w). The pluronic surfactant has hydrophobic poly propylene and hydrophilic polyethylene oxide. Thus, the pluronic surfactant polymer wraps around the MCNT through hydrophobic

interaction, and the hydrophilic domain helps in the suspension. These MWCNTs combined with the irradiation of Nd: YAG using a 1064 nm laser at 3 W/cm^2 led to a 28° C increase in temperature. By contrast, single-walled carbon nanotubes (SWNTs) caused only a 4° C increase in temperature. The SWNTs were prepared similar to MWNT in saline by wraping pluronic polymer through adsorption. RENCA kidney cancer cells treated with MWCNTs and irradiated for 30 s using an NIR laser with a power density of 3 W/cm^2 resulted in a 62-fold reduction in cell viability compared with that of the cells treated with MWCNTs only (without laser). In the *in vivo* examination conducted before the PTT study, deep-tissue temperature mapping and heat shock protein (HSP) activation were monitored using sagittal MR imaging and immunofluorescence assay. The results confirmed that the mice bearing RENCA tumor xenografts that were intratumorally injected with MWCNTs followed by laser irradiation exhibited an increased deep-tumor tissue temperature, and more HSP was induced in the tumor base compared with that in the tumors treated using the laser alone or MWCNTs only. In PTT, the survival rate of the mice injected with MWCNTs intratumorally that underwent laser irradiation was prolonged for 3 months, whereas the mice that received MWCNTs only or laser irradiation alone had a maximal survival of approximately a month. In addition, SWCNTs decorated with noble metals were used to conduct efficient photothermal therapy and surface-enhanced Raman spectroscopy (SERS) imaging.[124] The SWNT was coated with DNA using noncovalent integration to form DNA-SWNT with a -23 mV surface charge. This negative charge was inverted to +24 mV by coating poly(allylamine hydrochloride) (PAH), which formed PAH-DNA-SWNT. The PAH-DNA-SWNT was then decorated with negatively charged Au seeds by employing the *in situ* reaction of HAuCl$_4$ precursor solution with tetrakis-(hydroxymethyl) phosphonium chloride, which served as the reducing agent. The Au seeds decorated on the PAH-DNA-SWNT were further grown to obtain a complete Au coating, designated as PAH-DNA-SWNT@Au. The strong NIR absorption property of PAH-DNA-SWNT@Au found applications in SERS and PTT. For the *in vitro* experiments, PAH-DNA-SWNT@Au was functionalized with FA by tethering FA-PEG-grafted poly(maleic anhydride-alt-1-octadecene), which formed FA-PEG-PAH-DNA-SWNT@Au. FA-PEG-PAH-DNA-SWNT@Au, incubated with folic receptor positive KB cells, exhibited an enhanced Raman signal and the major advantage of this composite was that it required a short imaging time (a few minutes, compared to SWNT, which required hours in Raman studies). In PTT, KB cells were incubated with FA-PEG-PAH-DNA-SWNT@Au and irradiated for 5 min with an 808 nm laser using a power density of 1 W/cm^2, which caused the destruction of cells, observed in both the tryphan blue and propidium iodide staining results. The cells treated with PEG-PAH-DNA-SWNT@Au, FA-PEG-PAH-DNA-SWNT, or PEG-PAH-DNA-SWNT, followed by laser irradiation, were not destroyed. Finally, the photostability of FA-PEG-PAH-DNA-SWNT@Au was compared with that of Au NR by exposing them for 1 h to an 808 nm laser with a power density of 1 W/cm^2; Au NR exhibited a complete loss of absorbance, whereas FA-PEG-PAH-DNA-SWNT@Au retained nearly 87% of the absorbance intensity, as shown in Fig. 23.
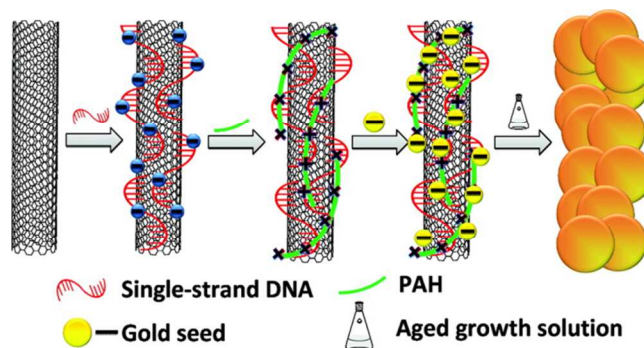

Fig. 23. Schematic illustration of the synthetic procedure used for the SWNT@Au nanocomposite. (Reprinted with permission from ref. 124. Copyright *J. Am. Chem. Soc.,* 2012.)

The proper surface functionalization of CNTs renders them biocompatible and enables them to serve as efficient cancer drug delivery vehicles. Because loading aromatic drugs using CNTs by employing noncovalent π-π stacking is simple, the high surface area of the CNTs can occupy approximately 70%–80% of its surface with stacked DOX molecules.[125] Based on this, Liu *et al.*[126] demonstrated DOX loading, delivery, and chemotherapy using the composite. The SWNT was PEGylated with phospholipid-branched PEG by applying the noncovalent interaction. This PEGylated SWNT was loaded with DOX using π-π stacking to form SWNT-DOX. This SWNT-DOX achieved maximal drug loading of up to 4 g of DOX per gram of SWNT. The circulation half life of SWNT-DOX extended to 2.22 h, whereas that of the free DOX was only 0.21 h. This extension in the circulation half life enhanced the uptake of SWNT-DOX compared with the uptake when DOX was used, quantified according to fluorescence. In the *in vivo* study, mice bearing Raji lymphoma xenograft tumors were individually intravenously injected with SWNT-DOX and the free drug. The size of the tumor in the untreated control increased rapidly (7.53 fold), whereas the mice injected with SWNT-DOX exhibited tumor growth inhibition (2.15-fold). Thus, the mice treated with SWNT-DOX displayed an approximately 72% reduction in tumor size compared with that of the untreated control. However, the mice treated with free DOX and DOXIL (DOX in liposome) demonstrated a 2.9- and 0.88-fold increase in tumor size, respectively. This indicated that SWNT-DOX was more effective than the free DOX, but not effective compared to the use of DOXIL during therapy. Therefore, the toxicity of SWNT-DOX, free DOX, and DOXIL was analyzed. The free DOX and DOXIL induced a 19% and 17% weight loss and 20% and 40% mortality, respectively, during a 2-week observation. In addition, SWNT-DOX was not toxic even at a concentration double that of the free DOX. Consequently, mice that were treated with SWNT-DOX (at a concentration double that of the free DOX)

exhibited complete control over tumor volume and no toxicity symptoms. An additional toxicity analysis was pursued, which revealed that free DOX induced gastrointestinal mucositis destruction, but SWNT-DOX did not. This was because of the ability of free DOX to diffuse into the intestine from the blood vessels. Unlike free DOX, SWNT-DOX cannot diffuse into the intestine because the large size limits its access to the intestinal tissues, as shown in Fig. 24. Therefore, SWNT-DOX formulation was observed to produce a more favorable therapeutic effect than free DOX did, and was accompanied by biocompatibility. This strategy can be readily adopted for chemotherapy involving lipophilic aromatic drugs such as daunorubicin, gefitinib, and camptothecin analogues,[65] as well as PTX.[127] Because of the photothermal effect, synergistic enhancement in therapeutic applications was also observed in a study where CNTs were used as a drug delivery vehicle.[128] In this study, SWNT was loaded with docetaxel using π-π accumulation, and was subsequently subjected to surface modification conducted using PVP and 1,2-distearoyl-sn-glycero-3-phosphoethanolamine-N-[methoxy(polyethylene glycol)-2000]-maleimide. Maleimide was further conjugated with the targeting NGR peptide (Asn-Gly-Arg) to form NGR-SWNT/DTX. The NGR-SWNT/DTX was administered intravenously to the mice bearing S180 tumor xenografts followed by irradiation with an 808 nm laser using a power density of 1.4 W/cm²; the mice were monitored for 13 days. The tumor volume was inhibited at the early stage (7th day) of combined chemotherapy and PTT, whereas, the other groups that received chemotherapy only (NGR-SWNT/DTX) or PTT only (NGR-SWNT with laser) exhibited a continual increase in tumor volume.
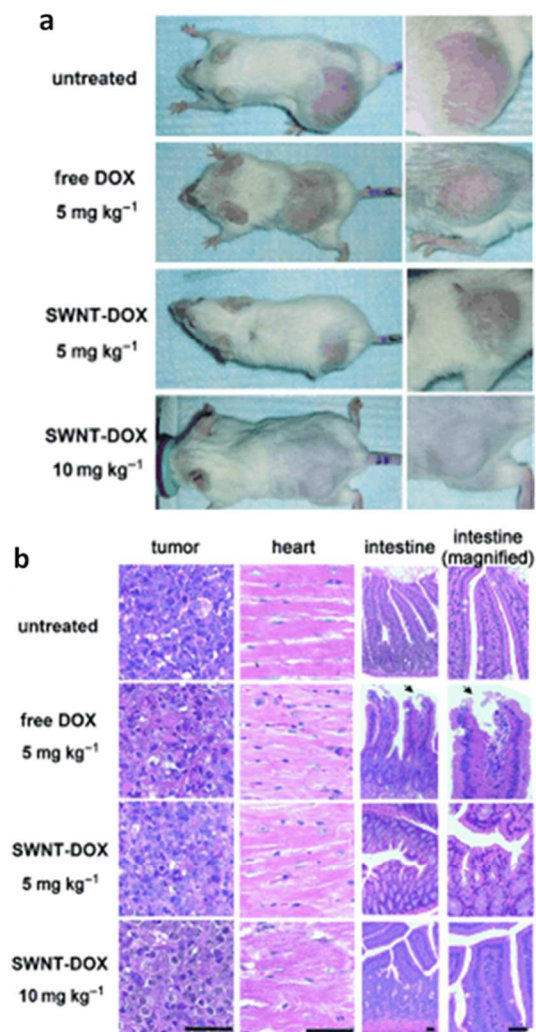

Fig. 24. SWNT–DOX exhibited less *in vivo* toxicity than free DOX did. (a) Representative photos of mice from different groups that were taken at the end of treatment. The mice became visibly thinner after receiving free DOX treatment. (b) Gastrointestinal toxicity was observed in mice treated with free DOX, but not in mice treated with SWNT-DOX. Histological sections of the intestinal epithelium were damaged in the free DOX-treated group. The arrows show the area of columnar epithelial cell loss at the tips of the villi. Scale bars: 100 µm. (Reprinted with permission from ref. 126. Copyright *Angew. Chem. Int. Ed.*, 2009.).

Despite the CNTs having twice the mass extinction coefficient value compared to GOs as an effective photothermal agent,[58] the applications in cancer therapy are seriously challenged because of their potential toxicity. CNT was reported to show genotoxicity, as they can pierce the cells and enter the nucleus easily. In the *in vivo* condition, the oral or intraperitoneal

administration of the CNTs reveals complications, such as inflammatory response and granuloma formation. These complications are due to the poor ability of CNTs to clear form the blood and tissue. Particles above 5 nm are not evidenced to clear the blood through urine in spite of the 43 nm glomerular capillary opening.[129] The blood clearance is subjected to the particle size, functionalisation and other factors which decide the degree of debundling. However, there are reports that even the CNTs with size more than 500 nm can be cleared through urine by orienting their small axis to the glomerular opening.[130-133] Considering the prolonged debate about the CNT toxicity, it is suggested that hydrophilic CNTs with stable dispersion in physiological medium need to be designed before clinical study for further studies.[134]

G.4. Gd related nanomaterials and Pd nanosheets

A combination of a T_1-weighted contrast agent and NIR-absorbing materials was developed for use in image-guided photothermal therapy. Huang *et al*. analyzed Gd_2O_3 coated with graphitic carbon prepared by combining gadolinium (III) tri(isopropoxide) with a gelatin template and calcination at 440 °C in air and followed by 600 °C in N_2 atmosphere.[135] This Gd_2O_3/C consisted of hollow cores and a shell-like nanostructure, and produced brightened images of the kidney cortex and liver. To improve the solubility of this material for biomedical applications, the Gd_2O_3/C nanoshells were coated with PSMA, improved the water solubility of the nanoshell and switched the imaging contrast effect of the contrast agent from positive to negative, as shown in Fig. 25. The graphitic carbon comprising the Gd_2O_3 had a large extinction coefficient of approximately 1563 M^{-1} cm^{-1} at 808 nm, and exhibited excellent absorbance in the NIR region during photothermal therapy.

The stable and photothermal efficiency of Pd nanosheets has motivated researchers to use these nanosheets as an effective PTT agent. The combination of Pd nanosheets either with mesoporous silica[136] or drug-loaded mesoporous silica for synergistic chemotherapy, and the possibility of inducing drug release either by pH or heat have been studied in recent years.[137,138] Regarding this topic, we present an example of the combination of PTT and chemotherapy. Hollow mesoporous silica (HMS) was synthesized using surfactant-assisted selective etching. This HMS was coated with a thin Pd sheet using noncovalent electrostatic attraction (Pd-HMS). The Pd-HMS reproduced the NIR absorbance capabilities of the Pd sheet. Pd-HMS also caused an approximately 20° C increase in temperature in 12 min when irradiation was administered using an 808 nm laser with a power density of 1 W/cm². Moreover, HMS was loaded with DOX using adsorption and then covered with the Pd sheet (Pd-HMS-DOX). The results indicated that 9% DOX loading occurred in Pd-HMS-DOX. The Pd-HMS-DOX exhibited both pH and temperature sensitive release behavior. As the pH decreased, the amount of DOX released from Pd-HMS-DOX increased. The Pd-HMS-DOX exposed and not exposed to laser irradiation for 5 min with an 808 nm laser using a power density of 1 W/cm² induced a 39% and 14.5% DOX release, respectively. In the *in vitro* examination, HEP G2 human hepatoblastoma cells were treated with Pd-HMS-DOX (20 µg/mL DOX), followed by exposure to the laser, which caused 90% of the cells to die, whereas administering the free DOX, Pd-HMS (with laser), and Pd-HMS-DOX (without laser) at the same concentration resulted in a 30%, 47%, and 28% cell death, respectively.
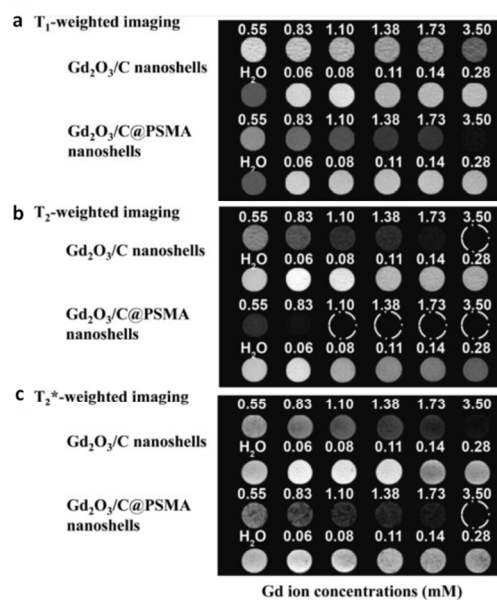

Fig. 25. MR *in vitro* assays of Gd_2O_3/C and Gd_2O_3/C@PSMA nanoshells. (a) T_1-weighted images (repetition-time/echo-time (TR/TE) = 472 ms/9.4 ms), (b) T_2-weighted images (TR/TE = 4500 ms/65 ms), and (c) T_2*-weighted images (TR/TE = 500 ms/5.2 ms; flip angle (α) = 30°) of the nanoshells in water containing 0.5% agarose gel. The images were taken using designed sequences with a matrix size of 256 x 192, a field of view of 60 x 60 mm, and a slice thickness of 6 mm operated at 125.3 MHz (3T MR system). (Reprinted with permission from ref. 135. Copyright *Adv. Funct. Mater.*, 2009.)

With relation to this review there are more reports that are not covered in the above text, the readers can refer to the Table 1 for additional references.

Table 1

Subject category	Reference
Au NRs	139-151
Au nanoshells	152-167
UCNPs	168, 169
CuS/Se	170-172

Conclusion and perspective

The use of nanoparticles in cancer therapy has improved site-specific drug delivery dramatically. The vast number of recent studies that were discussed in this review emphasize the various NIR-stimulated cancer therapies that can be used with the support of NIR light-sensitive nanoparticles. Generally, the NIR light-sensitive nanoparticles either transduce into heat or upconvert into high-energy visible radiation. The nanoparticles that transduce the irradiated photons into local heat facilitate local PTT or photothermal heat-responsive local drug release during chemotherapy. In addition, UCNPs, which convert low incident NIR energy into high-energy emissions, are promising in PDT. Because most photodynamic contrast agents require high energy excitation in visible wavelength, the upconverted high energy from UCNPs can induce excitement and ROS production in deep tissues. The upconversion that was demonstrated to uncage drug and improve targeting is another topic of interest. Thus, NIR light triggering secures PTT, chemotherapy, and PDT both spatially and temporally, which is a requirement in the future clinical execution of these cancer therapies. Without the assistance of nanoparticles, the possibility that undesired cell damage causes serious side effects, such as acute cardiac toxicity, when conventional therapy is used increases. Based on the studies reviewed, nanoparticle-assisted cancer therapy has been proven to effectively induce site-specific cell death in both *in vitro* and *in vivo* treatments and prevent side effects from occurring.

However, the designs described in this review exhibited variations in efficacy depending on the nanoparticle platforms used and the surface modifications that were applied. Therefore, by using the information provided in this review, obtaining the desired optical properties, an efficient targeting ligand with the highest specific uptake, and photothermal and upconversion conversion efficiency can be accomplished when using an ideal system. In addition, the improvement of the nanoparticle platforms, which is also warranted in this field, can be achieved with the following consideration: (1) The optical band and the photothermal efficiency of Au nanoparticles can be tuned and improved by exploring plasmon hybridization by the introduction of the dielectric gap in the form of core-shell structures; 2) regarding graphene, combination therapy (involving PTT, chemotherapy, and PDT), combination drugs (various drugs), and the variety of available thermoresponsive attachments must be further investigated; and (3) the excitation that occurs at 980 nm when UCNPs are used should also be investigated. Unlike 808-nm radiation, 980-nm radiation is absorbed by water and, consequently, the direct thermal effect must be avoided. Therefore, the excitation energy must be adjusted and addressed using various dopants. Considering these suggestions, an ideal nanoplatform can be constructed while maintaining cost efficiency for the next generation of noninvasive treatment methods.

Acknowledgements

Notes and references

1. T. S. Hauck, T. L. Jennings, T. Yatsenko, J. C. Kumaradas and W. C. W. Chan, *Adv. Mater.,* 2008, **20**, 3832-3838.
2. J. Moan and Q. Peng, *An outline of the history of PDT.* In Thierry Patrice. *Photodynamic Therapy* RSC publisher, 2003
3. R. Bonnett, *Chem. Soc. Rev.*, 1995, **24**, 19-33.
4. A. F. Bagley, S. Hill, G. S. Rogers and S. N. Bhatia, *ACS Nano,* 2013, **7,** 8089-8097.
5. Y.-L. Luo, Y.-S. Shiao and Y.-F. Huang, *ACS Nano,* 2011, **5**, 7796-7804.
6. B. M. I. van der Zande , M. R. Böhmer, L. G. J. Fokkink and C. Schönenberger, *Langmuir*, 2000, **16,** 451-458.
7. N. R. Jana, L. Gearheart, and C. J. Murphy, *Adv. Mater.,* 2001, **13**, 1389-1393.
8. B. Nikoobakht and M. A. El-Sayed, *Chem. Mater.,* 2003, **15**, 1957-1962.
9. N. R. Jana, *Small*, 2005, **1**, 875–882.
10. X. Huang, I. H. El-Sayed, W. Qian and M. A. El-Sayed, *J. Am. Chem. Soc.,* 2006, **128**, 2115-2120.
11. W. Choi, J.-Y. Kim, C. Kang, C. C. Byeon, Y. H. Kim and G. Tae, *ACS Nano,* 2011, **5,** 1995-2003.
12. D. K. Yi, I.-C. Sun, J. H. Ryu, H. Koo, C. W. Park, I.-C. Youn, K. Choi, I. C. Kwon, K. Kim and C.-H. Ahn, *Bioconjugate Chem.,* 2010, **21**, 2173-2177.
13. C. Bremer, C. H. Tung and R. Weissleder, *Nat. Med.,* 2001, **7,** 743-748.
14. W. Zhou, J. Shao, Q. Jin, Q. Wei, J. Tang and J. Ji, *Chem. Commun.*, 2010, **46**, 1479-1481.
15. L. Tong, Y. Zhao, T. B. Huff, M. N. Hansen, A. Wei and J.-X. Cheng, *Adv. Mater.,* 2007, **19**, 3136-3141.
16. C. Wang, J. Chen, T. Talavage and J. Irudayaraj, *Angew. Chem. Int. Ed.*, 2009, 48, 2759-2763.
17. H-W. Yang, H.-L. Liu, M.-L. Li, I-W. Hsi, C.-T. Fan, C.-Y. Huang, Y.-J. Lu, M.-Y. Hua, H.-Y. Chou, J.-W. Liaw, C.-C. M. Ma and K.-C. Wei, *Biomaterials,* 2013, **34,** 5651-5660.
18. F. Mohamed, P. Marchettini, O. A. Stuart, M. Urano and P. H. Sugarbaker, *Ann. Surgical Oncol.*, 2003, **10**, 463-468.
19. S. Ohno, Z. H. Siddik, Y. Kido, L. A. Zwelling and J. M. C. Bull, *Cancer Chemother Pharmacot.,* 1994, **34,** 302-306.
20. B. Barlogie, P. M. Corry and B. Drewinko, *Cancer Res*., 1980, **40**, 1165-1168.
21. J. Overgaard, M. M. Radacic and C. Gran, *Cancer Res*., 1991, **51**, 707-711.
22. D. S. Alberts, Y. M. Peng, G. Chert, T. E. Moon, T. C. Cetas and J.D. Hoeschele, *J. Natl. Cancer Inst.*, 1980, **65**, 455-461.
23. G. M. Hahn, J. Braun and I. Har-Kedar, *Proc. Natl. Acad. Sci. USA.,* 1975, **72**, 937-940.
24. J.-H. Park, G. Maltzahn, L. L. Ong, A. Centrone, T. A. Hatton, E. Ruoslahti, S. N. Bhatia, and M. J. Sailor, *Adv. Mater.*, 2010, **22**, 880-885.
25. Y. Zhong, C. Wang, L. Cheng, F. Meng, Z. Zhong and Z. Liu, *Biomacromolecules,* 2013, **14**, 2411-2419.
26. Z. Xiao, C. Ji, J. Shi, E. M. Pridgen, J. Frieder, J. Wu and O. C. Farokhzad, *Angew. Chem. Int. Ed.*, 2012, **51**, 11853-11857.

27. Y. T. Chang, P. Y. Liao, H. S. She, Y. J. Tseng, F. Y. Cheng, and C. S. Yeh, *Adv. Mater.,* **2012** *, 24*, 3309-3314.

28. W.-S. Kuo, C.-N. Chang, Y.-T. Chang, M.-H. Yang, Y.-H. Chien, S.-J. Chen, and C.-Sh. Yeh, *Angew. Chem. Int. Ed.,* 2010, **49**, 2711-2715.

29. D. P. O'Neal, L. R. Hirsch, N. J. Halas, J. D. Payne and J. L. West, *Cancer Lett.* 2004, **209**, 171-176.

30. C. Loo, A. Lowery, N. Halas, J. West and R. Drezek, *Nano Lett.,* 2005, **5**, 709-711.

31. S.-Y. Liu, Z.-S. Liang, F. Gao, S.-F. Luo and G.-Q. Lu, *J. Mater Sci: Mater Med.,* 2010 **21**, 665-674.

32. A. M. Gobin, M. H. Lee, N. J. Halas, W. D. James, R. A. Drezek and J. L. West *Nano Lett,* 2007, **7**, 1929-1934.

33. M.-R. Choi, K. J. S. Maxey, J. K. Stanley, C. S. Levin, R. Bardhan, D. Akin, S. Badve, J. Sturgis, J. P. Robinson, R. Bashir, N. J. Halas and S. E. Clare, *Nano Lett.,* 2007, **7**, 3759-3765.

34. H. Ke, J. Wang, Z. Dai, Y. Jin, E. Qu, Z. Xing, C. Guo, X. Yue, and J. Liu, *Angew. Chem. Int. Ed.*, 2011, **50**, 3017-3021.

35. S. E. Skrabalak, J. Chen, L. Au, X. Lu, X. Li, and Y. Xia, *Adv. Mater.* 2007, **19**, 3177-3184.

36. J. Chen, D. Wang, J. Xi, L. Au, A. Siekkinen, A. Warsen, Z.-Y. Li, H. Zhang, Y. Xia and X. Li, *Nano Lett.*, 2007, **7**, 1318-1322.

37. J. Chen, C. Glaus, R. Laforest, Q. Zhang, M. Yang, M. Gidding, M. J. Welch and Y. Xia, *Small,* 2010, **6**, 811-817.

38. Y. N. Qiang, L. Ling, L. J. Mei, J. T. Tong, Z. L. Xin and X. X. Liang, *Chin. Phys. B,* 2013, **22**, 097502.

39. J. Kim, S. Park, J. E. Lee, S. M. Jin, J. H. Lee, I. S. Lee, I. Yang, J.-S. Kim, S. K. Kim, M.-H. Cho and T. Hyeon, *Angew. Chem. Int. Ed.,* 2006, **45**, 7754 -7758.

40. W. Stöber, A. Fink and E. Bohn, *J. Colloid Interface Sci.,* 1968, **26**, 62-69.

41. X. Ji, R. Shao, A. M. Elliott, R. J. Stafford, E. E.-Coss, J. A. Bankson, G. Liang, Z.-P. Luo, K. Park, J. T. Markert and C. Li, *J. Phys. Chem. C Nanomater Interfaces,* 2007, **111**, 6245-6251.

42. R. Bardhan, W. Chen, C. P.-Torres, M. Bartels, R. M. Huschka, L. L. Zhao, E. Morosan, R. G. Pautler, A. Joshi and N. J. Halas, *Adv. Funct. Mater.*, 2009, **19**, 3901-3909.

43. F.-Y. Cheng, C.-T. Chen and C.-S. Yeh, *Nanotechnology* 2009, **20,** 425104.

44. J. You, G. Zhang and C. Li, *ACS nano,* 2010, **4,** 1033-1041.

45. J. You, R. Shao, X. Wei, S. Gupta and C. Li, *Small,* 2010, **6**, 1022-1031.

46. G. Wu, A. Mikhailovsky, H. A. Khant, C. Fu, W. Chiu and J. A. Zasadzinski, *J. Am. Chem. Soc., 2008*, **130**, 8175-8177.

47. M. S. Yavuz, Y. Cheng, J. Chen, C. M. Cobley, Q. Zhang, M. Rycenga, J. Xie, C. Kim, K. H. Song, A. G. Schwartz, L. V.Wang and Y. Xia, *Nature Materials,* 2009, **8,** 935-939.

48. H. Liu, T. Liu, X. Wu, L. Li, L. Tan, D. Chen and F. Tang, *Adv. Mater.*, 2012, **24**, 755-761.

49. M.-F. Tsai, S.-H. G. Chang, F.-Y. Cheng, P. S. Vijayakumar, Y.-S. Cheng, C.-H. Su and C.-S. Yeh, *ACS Nano,* 2013, **7**, 5330-5342.

50. Y. Su, X. Wei, F. Peng, Y. Zhong, Y. Lu, S. Su, T. Xu, S.-T. Lee and Y. He, *Nano Lett.,* 2012, **12**, 1845-1850.

51. J.-O. You, P. Guo and D. T. Auguste, *Angew. Chem. Int. Ed.,* 2013, **52**, 4141-4146.

52. H. Park, J. Yang, J. Lee, S. Haam, I. H. Choi and K. H. Yoo, *ACS nano,* 2009, **3**, 2919-2926.

53. J. Lin, S. Wang, P. Huang, Z. Wang, S. Chen, G Niu, W. Li, J. He, D. Cui, G. Lu, X. Chen and Z. Nie, *ACS nano,* 2013, 7, **5**, 5320-5329.

54. W. S. Hummers and R. E. Offeman, *J. Am. Chem. Soc.,* 1958, **80**, 1339.

55. Y. Si and E. T. Samulski, *Chem. Mater.,* 2008, **20**, 6792-6797

56. S. Gangadharaiah, A. M. Farid, and E. G. Mishchenko, *Physical Review Letters,* 2008, **100**, 166802-166804.

57. K. Yang, S. Zhang, G. Zhang, X. Sun, S.T. Lee and Z. Liu, *Nano Lett.,* 2010, **10**, 3318-3323.

58. J. T. Robinson, S. M. Tabakman, Y. Liang, H. Wang, H. S. Casalongue, D. Vinh and H. Dai, *J. Am. Chem. Soc.*, 2011, **133**, 6825-6831.

59. D.-K. Lim, A.Barhoumi, R. G. Wylie, G. Reznor, R. S. Langer and D. S. Kohane, *Nano Lett.,* 2013, **13**, 4075-4079.

60. S.-H. Hu, Y.-W. Chen, W.-T. Hung, I-W. Chen, and S.-Y. Chen, *Adv. Mater.,* 2012, **24**, 1748-1754.

61. R. R.-Aburto , T.. N. Narayanan , Y. Nagaoka , T. Hasumura , T. M. Mitcham , T. Fukuda , P. J. Cox , R. R. Bouchard , T. Maekawa , D. S. Kumar , S. V. Torti , S. A. Mani and P. M. Ajayan, *Adv. Mater.*, 2013, DOI: 10.1002/adma201301804

62. X. Shi, H. Gong, Y. Li, C. Wang, L. Cheng and Z. Liu, *Biomaterials,* 2013, **34,** 4786-4793.

63. X. Yang, X. Zhang, Z. Liu, Y. Ma, Y. Huang, and Y. Chen *J. Phys. Chem. C,* 2008, **112**, 17554-17558.

64. X. Sun, Z. Liu, K. Welsher, J. T. Robinson, A. G., S. Zaric, and H. Dai, *Nano Res.,* 2008, **1,** 203-212.

65. Z. Liu, J. T. Robinson, X. M. Sun and H. Dai, *J. Am. Chem. Soc.*, 2008, **130**, 10876-10877.

66. S. P. Sherlock, S. M. Tabakman, L. Xie and H. Dai, *ACS Nano,* 2011, **5,** 1505-1512.

67. W. Zhang, Z. Guo, D. Huang, Z. Liu, X. Guo and H. Zhong, *Biomaterials,* 2011, **32,** 8555- 8561.

68. Y. Wang, K. Wang, J. Zhao, X. Liu, J. Bu, X. Yan, and R. Huang, *J. Am. Chem. Soc.,* 2013, **135**, 4799-4804.

69. Y. Wang, W. Shi, W. Song, L. Wang, X. Liu, J. Chen and R. Huang, *J. Mater. Chem.*, 2012, **22**, 14608-14616.

70. H. Kim, D. Lee, J. Kim, T. Kim and W. J. Kim, *ACS Nano,* 2013, **7,** 6735-6746.

71. T. Peck, S. Hill and M. Williams *Pharmacology for Anaesthesia and Intensive Care, Third Edition* Cambridge University Press 2008

72. C. Wang, J. Mallela, U. S. Garapati, S. Ravi, V. Chinnasamy, Y. Girard, M. Howell and S. Mohapatra, *Nanomedicine,* 2013, **9**, 903-911.

73. L. Zhou, W. Wang, J. Tang, J.-H. Zhou, H.-J. Jiang, and J. Shen, *Chem. Eur. J.,* 2011, **17**, 12084 - 12091.

74. P. Huang, C. Xu, J. Lin, C. Wang, X. Wang, C. Zhang, X. Zhou, S. Guo and D. Cui, *Theranostics,* 2011, **1,** 240 - 250.

75. A. Sahu, W. I. Choi, J. H. Lee and G. Tae, *Biomaterials*, 2013, **34,** 6239-6248.

76. B. Tian, C. Wang, S. Zhang, L. Feng, and Z. Liu, *ACS Nano,* 2011, **5,** 7000-7009.

77. W. Miao, G. Shim, S. Lee, S. Lee, Y. S. Choe and Y.-K. Oh, *Biomaterials,* 2013, **34,** 3402-3410.

78. J. Chen and J. X. Zhao *Sensors,* 2012, *12*, 2414-2435.

79. Q. Ju, D. Tu, Y. Liu, H. Zhu, X. Chen**,** *Comb. Chem. High Throughput Screen,* **2012,** *15*, 580-94.

80. C. Wang, H. Tao, L. Cheng and Z. Liu, *Biomaterials*, 2011, **32**, 6145-6154.

81. G. Tian, W. Ren, L. Yan, S. Jian, Z. Gu, L. Zhou , S. Jin, W. Yin, S. Li and Y. Zhao, *Small,* 2013, **9,** 1929-1938.

82. J. Shan, S.J. Budijono, G. Hu, N. Yao, Y. Kang, Y. Ju, and R.K. Prudhomme, *Adv. Funct. Mater.,* 2011, **21,** 2488-2495.

83. S. Cui, H. Chen, H. Zhu, J. Tian, X. Chi, Z. Qian, S. Achilefu and Y. Gu, *J. Mater. Chem.,* 2012, **22,** 4861-4873.

84. S. Cui, D. Yin, Y. Chen, Y. Di, H. Chen, Y. Ma, S. Achilefu and Y. Gu, *ACS Nano,* 2013, **7,** 676-688.

85. P. Zhang, W. Steelant, M. Kumar and M. Scholfield, *J. Am. Chem. Soc.,* 2007, **129,** 4526-4527.

86. X-F. Qiao, J-C. Zhou, J-W. Xiao, Y-F. Wang, L-D. Sun and C-H. Yan, *Nanoscale,* 2012, **4,** 4611-4623.

87. N. M. Idris, M.K. Gnanasammandhan, J. Zhang, P.C.Ho, R. Mahendran and Y. Zhang, *Nature medicine,* 2012, **18,** 1580-1586.

88. A. Zhou, Y. Wei, B. Wu, Q. Chen and D. Xing, *Mol. Pharmaceutics,* 2012, **9,** 1580-1589.

89. K. Liu, X. Liu, Q. Zeng, Y. Zhang, L. Tu, T. Liu, X. Kong, Y. Wang, F. Cao, S. A. G. Lambrechts, M. C. G. Aalders and H. Zhang, *ACS Nano,* 2012, **6,** 4054-4062.

90. C. Wang, L. Cheng, Y. Liu, X. Wang, X. Ma, Z. Deng, Y. Li and Z. Liu, *Adv. Funct. Mater.,* 2013, **23,** 3077-3086.

91. G. Tian, Z. Gu, L. Zhou, W. Yin, X. Liu, L. Yan, S. Jin, W. Ren, G. Xing, S. Li and Y. Zhao, *Adv. Mater.,* 2012, **24,** 1226-1231.

92. Z. Hou, C. Li, P. Ma, G. Li, Z. Cheng, C. Peng, D. Yang, P.Yang and J. Lin, *Adv. Funct. Mater.,* 2011, **21***,* 2356-2365.

93. Z. Xu, P. Ma, C. Li, Z. Hou, X. Zhai, S. Huang and J. Lin, *Biomaterials,* 2011, **32,** 4161-4173.

94. H. Xu, L. Cheng, C. Wang, X. Ma, Y. Li and Z. Liu, *Biomaterials,* 2011, **32,** 9364-9373.

95. F. Zhang, G. B. Braun, A. Pallaoro, Y. Zhang, Y. Shi, D. Cui, M. Moskovits, D. Zhao and G. D. Stucky, *Nano Lett.,* 2012, **12,** 61-67.

96. Z. Hou, C. Li, P. Ma, Z. Cheng, X. Li, X. Zhang, Y. Dai, D. Yang, H. Lian and J. Lin, *Adv. Funct. Mater.,* 2012, **22,** 2713-2722.

97. S. Gai, P.Yang, C. Li, W. Wang, Y. Dai, N. Niu and J. Lin, *Adv. Funct. Mater.,* 2010, **20,** 1166-1172.

98. C. Li, D. Yang, P. Ma, Y. Chen, Y. Wu, Z.Hou, Y.Dai, J. Zhao, C.Sui and J. Lin*, Small,* 2013, **9,** 4150-4159.

99. B. Yan, J-C. Boyer, N.R. Branda and Y. Zhao, *J. Am. Chem. Soc.,* 2011, **133,** 19714-19717.

100. C-J. Carling, F. Nourmohammadian, J-C. Boyer and N.R. Branda, *Angew. Chem. Int. Ed.,* 2010, **49,** 3782-3785.

101. M.K.G. Jayakumar, N.M. Idris and Y. Zhang, *P Natl. Acad. Sci. USA.,* 2012, **109,** 8483-8488.

102. Y. Yang, Q. Shao, R. Deng, C. Wang, X. Teng, K. Cheng, Z. Cheng, L. Huang, Z. Liu, X. Liu and B. Xing, *Angew. Chem. Int. Ed.,* 2012, **51,** 3125-3129.

103. N. C. Fan, F. Y. Cheng, J. A. Ho and C. S. Yeh, *Angew. Chem. Int. Ed*., 2012, **51,** 8806-8810.

104. Y.-H. Chien, Y.-L. Chou, S.-W. Wang, S.-T. Hung, M.-C. Liau, Y.-J. Chao, C.-H. Su and C.-S. Yeh, *ACS Nano,* 2013, **7,** 8516-8528.

105. L. Cheng, K. Yang, Y. Li, J. Chen, C. Wang, M. Shao, S-T. Lee and Z. Liu, *Angew. Chem. Int. Ed.,* 2011, **50,** 7385-7390.

106. L. Cheng, K. Yang, Y. Li, X. Zeng, M. Shao, S-T. Lee and Z. Liu, *Biomaterials,* 2012, **33,** 2215-2222.

107. Y. Wang, H. Wang, D. Liu, S. Song, X. Wang and H. Zhang, *Biomaterials,* 2013, **34,** 7715-7724.

108. C.J. Chen and D. H. Chen, *Chem. Eng. J.,* 2012, **180,** 337-342.

109. P. K. Jain, K. S. Lee, I. H. El-Sayed and M. A. El-Sayed, *J. Phys. Chem. B,* 2006, **110,** 7238-7248 .

110. M. Zhou, R.Zhang, M. Huang, W. Lu, S. Song, M. P. Melancon, M. Tian, D. Liang and C.Li, *J. Am. Chem. Soc.,* 2010, **132,** 15351-15358.

111. Q. Tian, M. Tang, Y. Sun, R. Zou, Z. Chen, M. Zhu, S. Yang, J. Wang, J. Wang and J.Hu, *Adv. Mater.*, 2011, **23***,* 3542-3547.

112. S. Goel, F. Chen and W. Cai, *Small,* 2013, **10,** 631-645.

113. C.M. Hessel, V.P. Pattani, M. Rasch, M.G. Panthani, B. Koo, J.W. Tunnell and B.A. Korgel, *Nano Lett.,* 2011, **11,** 2560-2566.

114. M-Y. Liao, P-S. Lai, H-P. Yu, H-P. Lin and C-C. Huang, *Chem. Commun.,* 2012, **48,** 5319-5321.

115. M. Chu, Y. Shao, J. Peng, X.Dai, H. Li, Q. Wu and D. Shi, *Biomaterials,* 2013, **34,** 4078-4088.

116. Z. Li, C. Wang, L. Cheng, H. Gong, S. Yin, Q. Gong, Y. Li and Z. Liu, *Biomaterials,* 2013, **34,** 9160-9170.

117. C. Wang, H. Xu, C. Liang, Y. Liu, Z. Li, G. Yang, L. Cheng, Y. Li and Z. Liu, *ACS Nano,* 2013, **7,** 6782-6795.

118. A. Burke, X. Ding, R.Singh, R. A. Kraft, N. L.Polyachenko, M. N. Rylander, C. Szot, C. Buchanan, J. Whitney, J. Fisher, H. C. Hatcher, R. D'Agostino, Jr., N. D. Kock, P. M. Ajayan, D. L. Carroll, S. Akman, F.M. Torti and S. V. Torti, *Proc. Natl. Acad. Sci. USA,* 2009, **106,** 12897-12902.

119. S. Ghosh, S. Dutta, E. Gomes, D. Carroll, R. D'Agostino, Jr., J. Olson, M. Guthold and W. H. Gmeiner, *ACS Nano,* 2009, **3,** 2667-2673.

120. H.K. Moon, S. H. Lee and H. C. Choi, *ACS Nano,* 2009, **3,** 3707-3713.

121. Z. Liu, C. Davis, W. Cai, L. He, X. Chen and H. Dai, *Proc. Natl. Acad. Sci. USA,* 2008, **105,** 1410-1415.

122. N.W.S. Kam, M. O'Connell, J.A. Wisdom and H. Dai, *Proc. Natl. Acad. Sci. USA,* 2005, **102,** 11600-11605.

123. J.T. Robinson, K. Welsher, S. M. Tabakman, S. P. Sherlock, H. Wang, R. Luong and H. Dai, *Nano Res.,* 2010, **3,** 779-793.

124. X. Wang, C. Wang, L. Cheng, S-T. Lee and Z. Liu, *J. Am. Chem. Soc.,* 2012, **134,** 7414-7422.

125. Z. Liu, X. M. Sun, N. N. Ratchford and H. J. Dai, *ACS Nano,* 2007, **1,** 50-56.

126. Z. Liu, A. C. Fan, K. Rakhra, S. Sherlock, A. Goodwin, X. Chen, Q. Yang, D. W. Felsher and H. Dai, *Angew. Chem. Int. Ed.,* 2009, **48,** 7668-7672.

127. Z. Liu, K. Chen, C. Davis, S. Sherlock, Q. Cao, X. Chen and H. Dai, *Cancer Res.,* 2008, **68,** 6652-6660.

128. L. Wang, M. Zhang, N. Zhang, J. Shi, H. Zhang, M. Li, C. Lu and Z. Zhang, *Int. J. Nanomedicine,* 2011, **6,** 2641-2652.

129. W.M. Deen, M.J. Lazzara, B.D. Myers *Am. J. Physiol. Renal Physiol*., 2001, **281,** F579–F596

130. R. Singh, D. Pantarotto, L. Lacerda, G. Pastorin, C. Klumpp, M. Prato, A. Bianco, K. Kostarelos *Proc. Natl. Acad. Sci. U. S. A.,* 2006, **103** 3357–3362

131. L. Lacerda, A. Soundararajan, R. Singh, G. Pastorin, K.T. Al-Jamal, J. Turton, P. Frederik, M.A. Herrero, S.L.A. Bao, D. Emfietzoglou, S. Mather, W.T. Phillips, M. Prato, A. Bianco, B. Goins, K. Kostarelos *Adv. Mater*., 2008 **20** 225–230

132. L. Lacerda, M.A. Herrero, K. Venner, A. Bianco, M. Prato, K. Kostarelos *Small*, 2008 **4**1130–1132

133. A. Ruggiero, C.H. Villa, E. Bander, D.A. Rey, M. Bergkvist, C.A. Batt, K. M.-Todorova, W.M. Deen, D.A. Scheinberg, M.R. McDevitt *Proc. Natl. Acad. Sci. U. S. A.,* 2010 **107** 12369–12374

134. R. Singh, S. V. Torti *Advanced Drug Delivery Reviews* 2013, **65,** 2045–2060

135. C-C. Huang, C-H. Su, W-M. Li, T-Y. Liu, J-H. Chen and C-S. Yeh, *Adv. Funct. Mater.,* 2009, **19,** 249-258.

136. S. Tang, X. Huang and N. Zheng, *Chem. Commun.,* 2011, **47,** 3948-3950.

137. W. Fang, S. Tang, P. Liu, X. Fang, J. Gong, and N. Zheng, *Small,* 2012, **8,** 3816-3822.

138. W. Fang, J. Yang, J. Gong and N. Zheng, *Adv. Funct. Mater.*, 2012, **22**, 842-848.

139. A. Wei, A. P. Leonov and Q. Wei, *Mol. Imaging*, 2008, **7,** 50-57.

140. C.-L. Chen, L.-R. Kuo, C.-L. Chang, Y.-K. Hwu, C.-K. Huang, S.-Y. Lee, K. Chen, S.-J. Lin, Jing-D. Huang and Y.-Y. Chen, *Biomaterials,* 2010, **31,** 4104–4112.

141. H. Takahashi, T. Niidome, A. Nariai, Y. Niidome and S. Yamada, *Chem. Lett.,* 2006, **35,** 500-501.

142. Z. Li, P. Huang, X. Zhang, J. Lin, S. Yang, B. Liu, F. Gao, P. Xi, Q. Ren and D. Cui, *Mol. Pharm.,* 2009, **7,** 94–104.

143. G. P. Goodrich, L.L. Bao, K. G.-Sharp, K. L. Sang, J. Wang and J. D. Payne, *J. Biomed. Opt.,* 2010, **15,** 18001-18008.

144. D. Pissuwan, S. M. Valenzuela, M. C. Killingsworth, X. Xu and M. B. Cortie *J. Nanopart. Res.,* 2007, **9,** 1109–112.

145. K. C. Black, N. D. Kirkpatrick, T. S. Troutman, L. Xu, J. Vagner, R. J. Gillies, J. K. Barton, U. Utzinger and M. Romanowski, *Mol Imaging.,* 2008, **7,** 50-57.

146. R. Guo, L. Zhang, H. Qian, R. Li, X. Jiang and B. Liu, *Langmuir,* 2010, **26,** 5428–5434.

147. Z. Zhang, L. Wang, J. Wang, X. Jiang, X. Li, Z. Hu, Y. Ji, X. Wu and C. Chen, *Adv. Mater.*, 2012, **24,** 1418–1423.

148. X. Yang , X. Liu , Z. Liu , F. Pu, J. Ren and X. Qu, *Adv. Mater.*, 2012, **24**, 2890–2895.

149. M. Ma, H. Chen, Y. Chen, X. Wang, F. Chen, X. Cui and J. Shi, *Biomaterials,* **33,** 2012, 989-998.

150. H.S. Qian, H. C. Guo, P. C.-L. Ho, R. Mahendran and Y. Zhang, *Small,* 2009, **5,** 2285–2290.

151. Y. I. Park, H. M. Kim, J. H. Kim, K. C. Moon, B. Yoo, K. T. Lee, N. Lee, Y. Choi, W. Park, D. Ling, K. Na, W. K. Moon, S. H. Choi, H. S. Park, S.-Y.g Yoon,Y. D. Suh, S. H. Lee and T. Hyeon, *Adv. Mater.,* 2012, **24,** 5755–5761.

152. Y. Hu, L. Meng, L. Niu and Q. Lu, *ACS Appl. Mater. Interfaces,* 2013, **5,** 4586−4591.

153. S. I. Stoeva, F. Huo, J.-S. Lee and C. A. Mirkin, *J. Am. Chem. Soc*., 2005, **127**, 15362-15363.

154. H. Zhang, Y. Li, I. A. Ivanov, Y. Qu, Y. Huang and X. Duan, *Angew. Chem. Int. Ed*., 2010, **49**, 2865-2868.

155. J. You, R. Zhang, C. Xiong, M. Zhong, M. Melancon, S. Gupta, A. M. Nick, A. K. Sood and C. Li Effective, *Cancer Res*., 2012 ,**72,** 4777-47786.

156. H. Liu, D. Chen, L. Li, T. Liu, L. Tan, X. Wu and F. Tang, *Angew. Chem. Int. Ed.,* 2011, **50**, 891-895.

157. J. You, R. Zhang, G. Zhang, M. Zhong, Y. Liu, C. S. V. Pelt, D. Liang, W. Wei, A. K. Sood and C. Li, *J. Control. Release,* 2012, **158,** 319-328.

158. S.-K. Baek, A. R. Makkouk, T. Krasieva, C.-H. Sun, S. J. Madsen and H. Hirschberg, *J Neurooncol*., 2011, **104,** 439–448.

159. T. D. Yang, W. Choi, T. H. Yoon, K. J. Lee, J.-S. Lee, S. H. Han, M.-G. Lee, H. S. Yim, K. M. Choi, M. W. Park, K.-Y. Jung and S.-K. Baek, *J. Biomed. Opt.,* 2012, **17**, 128003 1-8.

160. S. A. Waldman, P. Fortina, S Surrey, T Hyslop, L. J. Kricka and D. J. Graves, *Future Oncol.,* 2006, **2,** 705-16.

161. J. M. Stern, J. Stanfield, W. Kabbani, J.-T. Hsieh and J. A. Cadeddu, *The Journal Of Urology,* 2008, **179,** 748 – 753.

162. J. C. Y. Kah, K. Y. Wong, K. G. Neoh, J. H. Song, J. W. P. Fu, S. Mhaisalkar, M. Olivo and C. J. R. Sheppard, *J. Drug Targe.,* 2009, **17,** 181–193

163. H. Liu, D. Chen, F. Tang, G. Du, L. Li, X. Meng, W. Liang, Y. Zhang, X. Teng and Y. Li, *Nanotechnology,* 2008, **19,** 455101 (1-7).

164. L. Wang, J. Bai, Y. Li and Y. Huang, *Angew. Chem. Int. Ed.,* 2008, **47,** 2439-2442.

165. L. R. Hirsch, R. J. Stafford, J. A. Bankson, S. R. Sershen, B. Rivera, R. E. Price, J. D. Hazle, N. J. Halas and J. L. West, *PNAS.,* 2003, **100,** 13549–13554.

166. J. A. Schwartz, A. M. Shetty, R. E. Price, R. J. Stafford, J. C. Wang, R. K. Uthamanthil, K. Pham, R. J. McNichols, C. L. Coleman and J. D. Payne, *Cancer Res.,* 2009, **69,** 1659-1667.

167. W. Chen, C. A.-Orozco, N. C Biswal, C. P.-Torres, M. Bartels, R. Bardhan, G. Stinnet, X.-D. Liu, B. Ji, A. Deorukhkar, L. V Brown, S. Guha, R. G Pautler, S. Krishnan, N. J Halas and A. Joshi, *Nanomedicine,* 2013 doi:10.2217/nnm.13.84

168. F. Chen, S. Zhang, W. Bu, Y. Chen, Q. Xiao, J. Liu, H. Xing, L. Zhou, W. Peng and J. Shi *Chem. Eur. J.,* 2012, **18,** 7082 – 7090.

169. H. Guo, H. Qian, N. M. Idris and Y. Zhang *Nanomedicine: Nanotechnology, Biology, and Medicine,* 2010, **6,** 486–495.

170. Y. B. Li, W. Lu, Q. A. Huang, M. A. Huang, C. Li and W. Chen, *Nanomedicine,* 2010, **5,** 1161-1171.

171. Q. Tian, F. Jiang, R. Zou, Q. Liu, Z. Chen, M. Zhu, S. Yang, J. Wang, J. Wang and J. Hu, *ACS Nano,* 2011, **5,** 9761-9771.

172. S. Ramadan, L. Guo, Y. Li, B. Yan and W. Lu, *Small,* 2012, **8,** 3143-3150.

TOC

Near-Infrared light sensitive nanomaterials provide ideal nanoplatforms in site specific noninvasive cancer therapy.
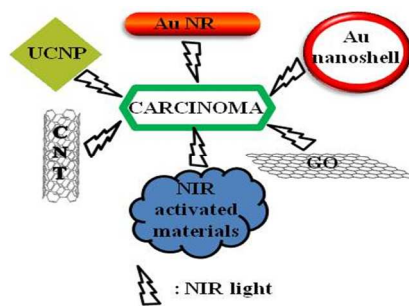
Chen-Sheng Yeh received a M.S. degree from National Tsing Hua University, Taiwan and a Ph.D. degree in Chemistry from University of Georgia, USA, in 1993. He then worked as postdoctoral fellow at Department of Chemistry in Purdue University, USA. He started as an Associate Professor at the Department of Chemistry, National Cheng Kung University, Taiwan, in 1995. He was promoted to Professor and Distinguished Professor in 2001 and 2009, respectively. His research focuses on the development of functional nanomaterials in biological applications and the area of nanostructured characteristics.

Vijayakumar P. Shanmugam obtained his Ph.D. in Environmental Science from Tamil Nadu Agricultural University, India. Following this from 2007 he pursued his postdoctoral studies on the bioapplication of nanoparticles, in the group of Dr. B.L.V. Prasad, National Chemical Lab, India and Prof. J.M. Zen, National Chung Hsing University, Taiwan. Currently he is doing postdoctoral research in Prof C.S.Yeh's lab in National Cheng Kung University, Taiwan, on the synthesis and application of the NIR sensitive nano-materials for the cancer therapy. His research interest covers the synthesis and bioapplications of nanoparticles.

S. Selvakumar, born in 1980, obtained his M.Sc degree in chemistry from Madurai Kamaraj University, India in 2002. He received his PhD degree from National Chemical Laboratory (India) in 2010. Thereafter he entered University of Lille1, France as postdoctoral researcher in 2010. Then in 2012 he joined Prof. C.S. Yeh group, National Cheng Kung University, Taiwan, as postdoctoral research fellow. His research interest focuses on multifunctional rare earth doped up-conversion nanophosphors for biomedical applications.